Title
Short- and Long-Term Tectonics across the Indo-Burma Range

Author
Maneerat, Patcharaporn

Publication Date
2022

Peer reviewed|Thesis/dissertation

Short- and Long-Term Tectonics across the Indo-Burma Range

by

Patcharaporn Maneerat

A dissertation submitted in partial satisfaction of the

requirements for the degree of

Doctor of Philosophy

in

Earth and Planetary Science

in the

Graduate Division

of the

University of California, Berkeley

Committee in charge:

Professor Roland Bürgmann, Chair
Professor Douglas Dreger
Associate Professor Laurel Larsen

Spring 2022

Short- and Long-Term Tectonics across the Indo-Burma Range

Abstract

Short- and Long-Term Tectonics across the Indo-Burma Range

by

Patcharaporn Maneerat

Doctor of Philosophy in Earth and Planetary Science

University of California, Berkeley

Professor Roland Bürgmann, Chair

The Indo-Burma Range (IBR) is a highly oblique subduction zone that accommodates both strike-slip and convergent motions. Previous short-term tectonic investigations of geodetic and microseismic have been unable to fully explain the active tectonics in this region, as they are most sensitive to the elastic component of earthquake cycle deformation. The current distribution of interseismic deformation and background seismicity does not capture the contributions of large earthquake ruptures, postseismic deformation and inelastic strain to the development of geologic structures and the topography of the range. This is evident in the ongoing controversy among different research groups on whether the subduction thrust is active, and whether the non-uniqueness of existing elastic block models is/can be constrained only by interseismic deformation measurements. Since the IBR is the only subaerial segment along this convergent boundary, it is an interesting region to investigate how landscapes evolve in this tectonic setting. Therefore, this dissertation aims to investigate both short-term (stress orientations and plate driving forces) and long-term tectonics (geomorphology and structure), which is the integrated result of active deformation over many earthquake cycles.

For my short-term tectonics study, the objective is to improve the understanding of the plate driving forces and subduction dynamics across the IBR boundary zone. I combined 189 focal mechanisms from available catalogs and publications from 1950 until 2019 and divided them to subdomains before performing stress inversions. As a result, I find that the maximum principal stress (σ_1) always is orientated approximately NS, subparallel to the subducting slab, even at deeper depths, while the intermediate principal stress (σ_2) is plunging toward the west at different angles for distinct subdomains. The minimum principal stress (σ_3) is plunging eastward nearly following the Indian slab dip angles, suggesting downdip tension. The σ_1 orientation is always consistent with depth, indicating that the NS compression is due to the slab pushing northward through the mantle. Also, the slab-dip parallels σ_3 at all depths below 30 km, demonstrating that the net slab pull is a primary driving force of this subduction zone. According to these observations, I propose that we cannot rule out that

the megathrust in this region is tectonically active and able to produce major events (> M8) in the future.

To study the long-term tectonics by investigating the morphometric expression, I first assessed the stability of the major drainage divides and investigated tectonic uplift employing 30×30 SRTM digital elevation model (DEM) to generate watersheds, streams and drainage divides. To examine the divide stability, I used Gilbert's metrics (including channel elevation, relief and gradient) and χ of the channel heads located on both sides of the divide segments. Then I calculated the basin-scale (hypsometry and relief) and stream-scale (normalized steepness index, k_{sn}) geomorphic indices to exhibit the pattern of the relative tectonic uplift rates. I find that most of the drainage divides are static, allowing us to explore uplift rates using the morphometric indices while also considering the variation in lithology and precipitation rates. Both basin- and stream-scale indicators are not well correlated with first-order variations of the lithology and precipitation rates, but they suggest greater relative uplift rates in the eastern, inner-belt region. I infer that out-of-sequence thrusts in the inner belt might play an important active role in generating greater relative uplift rates in this region even though the deformation front has long migrated westward.

According to the previous findings, it is possible that there is an out-of-sequence reactivation of older antiforms in the western outer belt of the IBR. Therefore, I employed the Earth surface dynamics models (Landlab) to investigate four possible, first-order thrust propagation scenarios. I first thoroughly investigated the characteristics of the young western antiforms and a total of 20 tributaries of four rivers (Feni, Karnaphuli, Sangu and Matamuhuri Rivers) in the outer belt region, utilizing the DEM employed previously. I created the fluvial profiles of 20 channels, which mostly are antecedent streams, and determined knickpoint locations along the streams. Next, I used the geomorphic observations of drainages and antiforms in the outer belt to generate four first-order surface dynamics models consisting of a set of three antiforms. The modeling scenarios include sequential thrust propagation, partial reactivation, continuous reactivation of older structures, and synchronous thrusting style. Then, I compared the antecedent stream profiles and knickpoint locations of the modeled cases to the observed channels in the outer belt of the IBR. The sequential propagation with continuous reactivation model, invoking continued growth of the eastern anticlines, correlates best with the outer-belt IBR, and synchronous thrust activity and growth also likely occur in the westernmost region. This means as the deformation front has migrated westward, the older eastern antiforms remain tectonically active. The IBR bivergent antiform structures and numerical modeling results of weak décollement also support my findings of out-of-sequence reactivated splay faults in the outer belt. This suggests an active megathrust in this region. Although it is still inconclusive if the megathrust will fully rupture causing > M8 events, it is more likely that frequent, intermediate earthquakes due to independent failures of reactivated subsidiary faults will occur in the future.

In summary, for my short-term study of the three-dimensional distribution of stress in the IBR, I cannot clearly support or reject ongoing subduction and megathrust slip across the IBR, while the long-term tectonics investigations help further elucidate the active tectonics across this region. The observation of greater relative uplift in the eastern inner belt and

reactivated out-of-sequence splay faults in the western outer belt suggest active distributed uplift across the region. Even though the stress orientations in this area do not suggest EW shortening, slab pull might have contributed to the EW convergent motion and active splay faults that are possibly rooted from the megathrust generating out-of-sequence thrust activity. This leads to continuing active tectonics in the inner and outer belts of the IBR. Although currently I cannot conclude whether the megathrust is fully locked and capable of producing the major events in the future, it is more likely that small and intermediate earthquakes will occur frequently in the interior of the system due to the failures of the active splay faults across the IBR. Since the structures and tectonics in the IBR are especially complex, more field surveys and other detailed studies, such as chronological dating and high-resolution tomography, are needed to further improve our understanding of the tectonics and earthquake hazards in this region.

To Petch, Ubol Maneerat and Eongyu Yi

Contents

List of Figures

List of Tables

Acknowledgments

First and foremost, I would like to extend my deepest gratitude to my advisor, Professor Roland Bürgmann, for his continuous support, encouragement and invaluable advice during these past five years. His immense knowledge, positive point of view and enthusiasm for science have encouraged me in all of my graduate research. By working with Roland, I have learned how to develop myself professionally and personally which I never expected that from graduate program. I am truly grateful that I had the opportunity to work with him.

I would like to express my appreciation to Professor Douglas Dreger, my secondary advisor. It was my first time learning how to generate moment tensor and perform stress inversion. It is my pleasure to work on the stress inversion project with him. Also, I would like to thank my qualifying exam committee Professor David Shuster and Associated Professor Laurel Larsen.

Thanks to everyone in the Active Tectonics Research group, especially my fellow graduate students and postdoctoral researchers, Yuexin Li, Danielle Lindsay, Kathryn Materna, Kang Wang, Heather Shaddox, Yuankun Xu and Yifang Cheng for all fruitful research discussions that we have and always being supportive. I also would like to thank my officemates, Sarina Patel, Sevan Adourian, Li-Wei Chen, Robert Martin-Short, Nate Lindsey and Alexander Robson for creating great working environment and helping with many issues in research and life. Thanks to EPS graduate students, especially my cohort, for doing many activities together and always being supportive. My five years of graduate school would not be this wonderful without them.

I would like to express my appreciation to the Berkeley Seismology Lab staff and faculty for creating the supportive working environment and providing insights and knowledge during several discussions, such as Earthquake of the Week. I am truly grateful to be a part of this community.

I also would like to acknowledge the effort and invaluable advice of our research group collaborators from Earth Observatory of Singapore, Professor Emma Hill, Eric Lindsey and Rishav Mallick. Thanks for letting me joining the GPS survey in Myanmar, sharing the data and having a constructive discussion. I also would like to recognize the help from Professor Patricia Persaud from Louisiana State University. I am deeply glad that I had an opportunity to know her and her graduate students. I would like to acknowledge Professor Michael Steckler and Assistant Professor Paul Betka for useful discussions on my projects.

Finally, special thanks to my parents who have been supportive and understanding. Also many thanks to Eongyu for always being by my side through thick and thin. I would not have accomplished this without all of their supports.

Chapter 1

Introduction

The Indo-Burma Range (IBR) is a complex accretionary prism generated as a result of the highly oblique convergence between the Indian plate and the Burma microplate. It is estimated that the Indian plate has been subducting beneath the Burma microplate since ∼50 Ma (Hall, 2002). Over time, large volumes of sediment have been transported into the subduction zone, and the IBR fold-and-thrust belt deforming this material has become subaerial (Steckler et al., 2008). This is the only region in the convergent boundary where such structures are exposed. The westernmost portion of the plate boundary zone is buried due to the rapid sedimentation of the Ganges-Brahmaputra Delta (GBD) situated in the west of the IBR (Betka et al., 2018). To the north of the IBR lies the Shillong Plateau while to the east of the region is the Myanmar Central Basin. It remains controversial whether the megathrust in the IBR is capable of producing large magnitude earthquakes in the future. To improve our understanding of tectonics in this region, this dissertation aims to study both short- and long-term tectonics across the range.

For the short-term tectonic observations, a number of studies have investigated seismicity and stress orientations in the IBR. Kundu and Gahalaut (2012) find no significant discrepancy in the stress field at depth, and their stress inversion results suggest that the subduction is no longer active. They conclude that the lack of evidence of historical and current megathrust events supports low potential of great earthquakes in the future. On the other hand, Hurukawa et al. (2012) relocate focal mechanisms and find that three sub-crustal strike-slip events at depth ∼ 20 - 50 km have their P-axes trending in EW direction, suggesting a significant component of EW convergence in the region. Recently, Earnest et al. (2021) suggest EW convergent motion within the Kabaw Fault region, where the intra-slab stress is dominantly driven by the NS plate motion in the IBR. As such, existing literature contains contradictions regarding stress field observations and their interpretations. In Chapter 2, I utilize the larger quantity of focal mechanisms that have become available in recent years, combining the events from several catalogs and publications, i.e. GCMT, ISC, Hurukawa et al., (2012) and Mon Thet Chit et al. (2020). Then, I divide them based on several observations, i.e. variation in seismic velocities and slab geometries, and perform stress inversions to compare the results to previous publications. These results will contribute to our understanding of subduction

dynamics and the plate driving forces at play in the IBR subduction boundary.

Several geodetic and elastic block model studies also have been conducted in this region (i.e., Vigny et al., 2003; Socquet et al., 2006; Gahalaut et al., 2013; Kundu and Gahalaut, 2013; Steckler et al., 2016; Mallick et al., 2019; Panda et al., 2020). However, there are discrepancies between these publications that cannot be resolved by exclusively applying geodetic studies. Other data and investigations are needed for better understanding of tectonics in the region. Therefore, in Chapters 3 and 4, I study long-term tectonics, including (1) examining morphometric indices of the IBR basins and streams to find the patterns of relative uplift rates, and (2) using geomorphic observations to create Earth surface dynamics models in order to study the sequence of the thrust propagation in active IBR outer fold-and-thrust belt. Although the long-term tectonics study cannot be directly compared to the short-term tectonic observation, it contributes to overall understanding of tectonics in this region.

The geomorphology and drainage evolution of the IBR reflect the tectonic impacts of the region's recent geologic history. The characteristics of streams, basins and the underlying geologic structures, such as NS-oriented thrust-cored anticlines, can indicate which tectonic processes played the biggest role in creating these features. Although the observed long-term deformation is driven by IBR uplifts that occurred over the last millions of years (Chapters 3 and 4), these features might be reconcilable with the short-term strain fields calculated from GPS measurements and stress orientations inverted from focal mechanism data (Chapter 2), which provide snapshots of the current active deformation. Consideration of the deformation over a wide range of time scales allows us to assess if the study region has been governed by a similar tectonic regime over the last ∼million years. It is important to keep in mind that the surface deformation expressed in the landforms is a result of many earthquake cycles, but other factors, such as erosion, sedimentation and crustal flow, also contribute to the geomorphic expression.

Besides interesting geology, structures and tectonics across the IBR, this region is densely populated; therefore, the understanding of active tectonics is crucial in order to educate locals to prepare for future earthquakes or other associated hazards, such as landslides and tsunami. The Arakan earthquake (> M8.5) in 1762 likely occurred due to the slip on the megathrust and caused substantial damage in the Chittagong area, western IBR (Wang et al., 2014; Shyu et al., 2018). Although there has not been any recent great earthquakes (> M8), Kundu and Gahalaut (2012) indicate the sediment-filled areas, i.e. Manipur in India (∼2.7 millions of population) and Sylhet in Bangladesh (∼500k of population), can still be greatly impacted by small and intermediate earthquakes. Also, several publications suggest a future megathrust event is possible in the IBR, which will significantly impact a large area (i.e., Socquet et al., 2006; Steckler et al., 2016; Mallick et al., 2019; Vorobieva et al., 2021). Conducting research in the IBR, therefore, is not just necessary to improve our scientific understanding of the region's tectonics, but also adds to the body of knowledge available for local governments and organizations to use as they plan and prepare for possible future geohazards.

This dissertation contributes to our understanding of short-term tectonics in the IBR through the analysis of morphological features to characterize the distribution of accumulating

strain and the growth of geologic structures through the Quaternary. Stress orientation study, morphometric analysis and surface dynamics modeling of these observations help reveal the major drivers of deformation, including large scale megathrust and/or strike-slip faulting. Together, the investigation of both short- and long-term tectonics provide us with a more complete picture of tectonics in the IBR, a unique subaerial and highly oblique subduction zone.

Chapter 2

Stress orientations and driving forces in the Indo-Burma plate boundary zone

Published as: Maneerat, P., Dreger, D.S. and Bürgmann, R., 2021. Stress Orientations and Driving Forces in the Indo-Burma Plate Boundary Zone. Bulletin of the Seismological Society of America.

2.1 Abstract

The Indo-Burma Range (IBR) is the forearc of an oblique subduction zone where the Indian slab obliquely converges with the Burma microplate. In this study, we consider earthquake focal mechanisms to help elucidate the tectonic behavior of the region. Towards this end, we examine the spatially variable stress orientations across the IBR and in the downgoing plate to better understand the associated plate driving forces and subduction dynamics. We combined earthquake focal mechanisms from 1950/01/01 until 2019/12/31 from a number of available catalogs and published studies and divided the total of 189 events into spatial subdomains before performing stress inversions to document the spatial variability of the stress tensor. Generally, the maximum principal stress (σ_1) is oriented approximately NS in all domains, sub-parallel to the subducting slab. The intermediate principal stress (σ_2) is plunging westward at variable angles. In contrast, the minimum principal stress (σ_3) is plunging to the east roughly following the dip of the subducting plate, indicative of downdip tension in the slab. We do not observe a significant variation of the σ_1 orientation with depth and suggest that NS compression is due to the slab pushing northward through the mantle. Due to the well-defined slab-dip parallel σ_3 direction for the megathrust and upper plate catalogs, the primary driving force of this subduction region is likely to be a net slab pull. Based on the seismic activity of the region, the consistency of focal-mechanism-based stress and regional tectonic driving forces, as well as the σ_3 evidence for slab pull forces, the

possibility that the IBR can produce large earthquakes cannot be ruled out.

2.2 Introduction

The Indo-Burma Range (IBR) was formed in the Paleogene due to the India-Eurasia collision (Gahalaut et al., 2013; Mitchell, 1993) and represents the forearc of an oblique subduction zone, where the Indian plate subducts northeastward beneath the Burma microplate (Figure 2.1). Because the relative plate convergence is highly oblique, there is substantial partitioning between subduction on the plate interface and a number of crustal faults in the forearc (e.g., Steckler et al., 2016). However, the recent dominance of observed strike-slip and intraslab earthquakes at shallow to intermediate depths brings into question the present-day activity of the subduction megathrust in the IBR (Kundu and Gahalaut, 2012; Rao, 2005; Rao et al., 1990). Historical records point to a great earthquake in 1762, but whether it was a megathrust event is still debated in the literature (Kundu and Gahalaut, 2012). However, there are several geologic studies that provide evidence of substantial coastal uplift associated with the 1762 Arakan earthquakes (i.e., Than Tin Aung et al., 2008; Wang et al., 2013; Mondal et al., 2018). Wang et al. (2013) analyzed ages of uplifted coral and oyster fossils in Ramree and Cheduba Islands, on the western coast of Myanmar. According to their findings, the upper-plate splay faults were involved in the 1762 earthquake. Their faulting model suggests that the 1762 earthquake was at least M 8.5, and the approximate recurrence interval of such events is between 500 - 700 years. Mondal et al. (2018) examined corals and microatolls in Saint Martin's Island, southernmost of Bangladesh, and found evidence for three uplift events including the most recent 1762 earthquake. They also support that the recurrence interval of such megathrust events is between 500 - 700 years. Recently, Shyu et al. (2018) studied additional coral microatolls and provided further support for uplift generated by the 1762 Arakan event. They also found evidence for an earlier uplift event, about 800 - 900 years before the 1762 earthquake.

A number of studies relied on GPS-measured interseismic velocities to characterize the partitioning of deformation across the IBR. Several publications (e.g., Socquet et al. 2006; Mallick et al., 2019; Panda et al. 2020), highlight oblique India-Sunda convergence across the plate-boundary zone at $\sim$ 36 - 39 mm/yr. In contrast, Steckler et al. (2016) focus on the distribution of 46 mm/yr of differential motion between the Indian subcontinent and the Shan Plateau. This higher rate is due to the inclusion of GPS stations that are affected by toroidal flow associated with the distributed India-Eurasia collision zone (Panda et al., 2020; Mallick et al., 2019; Shi et al., 2018). Socquet et al. (2006) argue that the India-Sunda plate motion is accommodated by the megathrust (14 mm/yr), Sagaing Fault (SF, 18 mm/yr), and Kabaw Fault (KF, 9 mm/yr). They also present elastic dislocation models involving just the megathrust and the SF, which suggest that the Arakan megathrust accommodates 20 - 23 mm/yr of oblique convergence and is locked and eventually capable of generating a large magnitude earthquake. Mallick et al. (2019) find that the convergence rate across the Burma microplate is 12 - 24 mm/yr and the entire dextral motion is approximately 25 - 32

mm/yr. Finally, Panda et al. (2020) indicate that the plate motion in this region is primarily accommodated by the megathrust ($\sim$ 7 mm/yr), SF (18 mm/yr) and the Churachandpur Mao Fault (CMF, 17 mm/yr). In summary, while there is still disagreement regarding details of the partitioning of deformation across the IBR, all recent studies find significant convergence associated with the subduction megathrust.

A number of previous studies focused on improving earthquake locations and assessing the stress field in the IBR. Satyabala (1998) investigates the orientations of P and T axes of earthquakes occurring from 1977 - 1995. He finds that the T axes mostly follow the dip direction of the Indian slab indicating down-dip tension within the slab at intermediate depth. On the other hand, Guzmán-Speziale and Ni (2000) emphasize the lack of observations of interplate earthquakes. They also note that P axes are aligned parallel to the slab strike and T axes follow the downdip direction, suggesting that at shallow depths the stresses indicate arc-parallel bending while at greater depths there is gravitational pull. In addition, recent studies indicate the depth of relocated seismicity in this region ranges from near the surface to approximately 180 km (Stork et al., 2008; Hurukawa et al., 2012). Rao and Kalpna (2005) propose a transition of the faulting style at $\sim$ 90 km depth, featuring strike-slip events at shallower depths above 90 km and dominantly reverse events below. They suggest that the upper Indian slab ($<$ 90-km depth) stress is related to the plate motion while the lower segment ($>$ 90-km depth) is completely controlled by slab pull. On the other hand, Stork et al. (2008) suggest that after earthquake relocations both types of earthquakes are observed at depths greater than 100 km. They further propose that the northward moving slab is exposed to horizontal shear tractions. There are indications of spatial variations in the stress field within the Indian slab and overriding forearc, and more focal mechanisms are needed to improve stress inversion results and increase our understanding of stress orientations across the IBR and within the subducted slab.

Several tomographic studies have not been able to fully resolve the geometry and continuity of the slab. Li et al. (2008) suggest that the slab is continuous to at least a depth of 300 km. Pesicek et al. (2010) and Yao et al. (2021) find that the slab extends to a depth of $\sim$ 660 km. They also indicate that localized tears, windows, or thinned slab sections are possibly present, but these apparent slab gaps may be caused by poor resolution. In contrast, Rangin (2017) finds that the slab is clearly observed in northern and central Myanmar, but only extends to $\sim$ 200 km depth. In the south, the slab is not clearly resolved or possibly missing. Recently, Bai et al. (2020) suggest that the Indian slab in the IBR region extends to a depth of 440 km with a slab tear near the bottom. Overall, these tomographic studies confirm the existence of the Indian slab underneath the Burma microplate to at least 200 km depth. The tomographic evidence remains inconclusive as to whether the subducting slab is intact and can generate substantial gravitational slab-pull forces that influence present-day subduction in the IBR.

In this study, we aim to resolve the stress field in the IBR and the subducted Indian lithosphere in greater detail in order to (1) better understand plate driving forces and subduction dynamics, (2) clarify the varying faulting style and stress orientations across and along the deforming IBR forearc, and (3) contribute to improve earthquake hazard assessment in the

region.

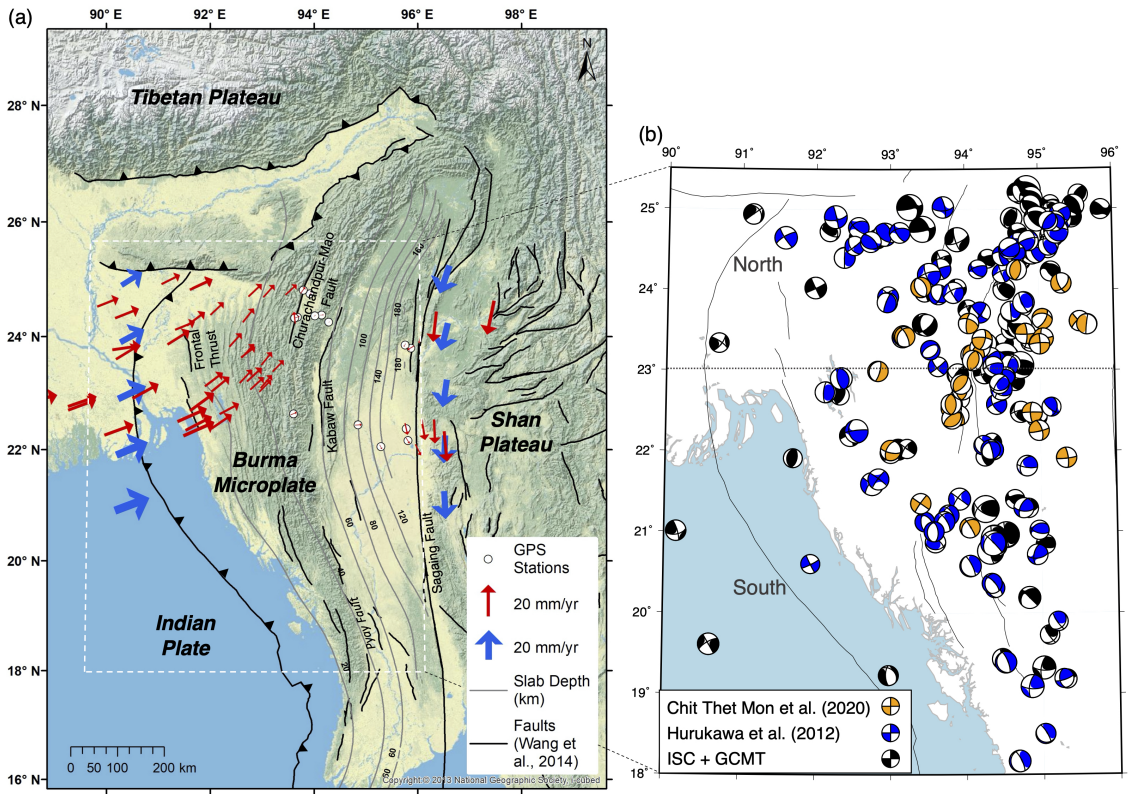

Figure 2.1: Regional tectonics and GPS velocity map. (a) topography and regional map. The red arrows represent GPS-measured surface velocities relative to the eastern Burma microplate, realized by minimizing the velocities of stations between the CMF and SF (Mallick et al., 2019). The white circles with black perimeters are the GPS station locations in the reference block. The velocity vectors (red arrows) are centered at the station locations. The blue arrows represent the plate motions relative to the eastern Burma microplate obtained from an elastic block model by Mallick et al. (2019). The thick gray lines are the slab depth contours extracted from SLAB2.0 (Hayes et al., 2018). The black lines are faults from Wang et al. (2014). The white dashed rectangle indicates the extent of the study region where stress inversions were performed. (b) The studied earthquakes used for the stress inversion in this study. Note that some of Hurukawa et al. (2012)'s events are the same as ISC and GCMT catalogs. We plot those events in Hurukawa et al. (2012) group instead, since they are the same events. The black lines are faults (Wang et al., 2014). The dark gray, thick dashed line represents the boundary line separating north and south used in the earthquake division for latitudinal range domain (A2).

2.3 Data and Methodology

Stress Inversion

We employed the STRESSINVERSE (v1.1) software from Vavryčuk (2014) to invert for the stress tensor from the focal mechanism catalog. We obtain information on the principal stress axes orientations ($\sigma_1 > \sigma_2 > \sigma_3$), coefficient of friction, and the shape ratio (R-value). An advantage of this method is the application of an additional fault instability constraint that finds the best oriented nodal planes that are consistent with a determined stress tensor and an assumed coefficient of friction. The coefficient of friction is evaluated by forward sensitivity testing. The code works by randomly sampling nodal planes and applying random noise to the focal parameters (we used up to 5-degrees of noise), and bootstrapping 1000 realizations to find the optimal stress parameters as well as characterizing the uncertainty in the estimates. For each inversion we allow for 6 iterations to converge. We allow a range in the shape ratio from 0 - 1.0 with 0.025 increments, and a friction value range of 0 - 1.0 with a 0.05 increment.

Focal Mechanism Data

Prior to performing stress-tensor inversions, we compared different moment tensor catalogs to assess their consistency and optimally combine the available data. We used the available catalogs from the Global Centroid Moment Tensor (GCMT) and the USGS National Earthquake Information Center (NEIC) moment tensor catalogs (see Data and Resources Section). We used 41 pairs of the common events between these two catalogs that occurred since 2000 in the IBR. We compared their focal mechanisms considering Kagan angles (Kagan 2007; Kagan 1991), coordinates, and hypocenter depths. The average Kagan angle between the events from both catalogs is 10.82° ± 7.36°. The average differences of latitude, longitude, and hypocenter depth are 0.10° ± 0.07°, 0.10° ± 0.10°, and 8.62 ± 8.73 km, respectively. Accordingly, we conclude that the focal mechanisms of these catalogs are similar within uncertainties and can be combined to increase the number of focal mechanisms used for the subsequent stress inversion.

For further analysis, we decided to use the catalog collected by the International Seismological Centre (ISC, see Data and Resources Section), since this catalog includes some focal mechanisms from GCMT and all NEIC mechanisms (either the PDE or W-phase solutions). Note that we also include some events directly from the GCMT catalog, since the ISC catalog does not contain all GCMT events. The combined catalog provides us with many more focal mechanisms (56 more events), which improves the stress inversions. The events from the ISC and GCMT catalogs have magnitudes equal to or greater than 4.5 in the period from 1950/01/01 to 2019/12/31, within 18 - 25.5° latitude and 91 - 96° longitude, thus excluding events occurring along the SF (Figure 2.1). The total number of GCMT and ISC events is 141 (85 events from ISC and 56 events from GCMT).

In addition, we included the relocated events from Hurukawa et al. (2012) and Chit Thet Mon et al. (2020). We first selected the relocated earthquakes in the Hurukawa et al. (2012) catalog that match the ISC and GCMT catalogs. The number of events occurring in the IBR in the Hurukawa et al. (2012) catalog is 82, and 58 events are also part of the earthquakes obtained from the ISC and GCMT catalogs. We found the differences between the coordinates and depths of these matched events from both catalogs (ISC&GCMT - Hurukawa et al., 2012) and calculated the averages of these differences. The average differences of latitudes, longitudes, and hypocenter depths of the matched events are -0.00487° ± 0.278°, 0.0423° ± 0.246°, 21.18 ± 20.59 km, respectively. As the event locations in Hurukawa et al. (2012) were relocated to obtain improved absolute event locations, we applied a uniform shift of the locations and hypocenter depths of the earthquakes obtained from ISC and GCMT by subtracting the calculated average differences from their latitudes, longitudes, and hypocenter depths. Thus, we selected all 82 events from the Hurukawa et al. (2012) catalog and added 83 events from ISC and GCMT that do not match the Hurukawa et al. (2012) events whose depths and coordinates were adjusted. Finally, we added 34 focal mechanisms from a temporary dense network by Chit Thet Mon et al. (2020) to increase the number of events in the upper plate and near the megathrust (Figure 2.1). The events from the Chit Thet Mon et al. (2020) catalog lie within latitude 21° - 24.5° and longitude 92.8° - 95.5° from 2016 - 2018 with a magnitude range of 2.8 M_L - 4.7 M_L. After adjusting the GCMT and ISC event locations and integrating the Hurukawa et al (2012) and Chit Thet Mon et al. (2020) catalogs, we have a total of 189 events for the stress inversion. Note that the actual total number of events is 199; however, 10 events do not lie within the horizontal extent of the slab geometry from the SLAB 2.0 model (Hayes et al., 2018). We excluded these ten events since we could not calculate their perpendicular distances to the slab interface.

Next, we used several approaches to divide the combined focal mechanism catalog into subdomains: (A1) all events, (A2) latitudinal ranges, (A3) hypocenter depth ranges, and (A4) the perpendicular distance of the events to the inferred slab interface (Hardebeck, 2015). For A2, we first classify the events into two groups based on their hypocenter depths, which are the events with depths (1) equal or less than 30 km and (2) below 30 km. This division is made according to tomography studies (i.e. Wang et al., 2019; Wu et al., 2021), suggesting the Moho depth is around 30 km. After that, we divide each group into two groups based on the variation in the topographic expression and first-order contrasting of seismic velocity from south to north (Wu et al., 2021). These two domains span ranges of latitude 18 - $<$ 23° (south), and 23 – 25.5° (north, Figure 2.1b). There are 4 subgroups of A2 as shown in Table 2.1. For A3 there are four groups for hypocenter depths with the following ranges 0 – 30, $>$ 30 – 50, $>$ 50 – 80, and $>$ 80 km (Table 2.1). The 0-30-km subgroup predominantly includes upper plate events while other subdomains contain mostly intraplate events. At 30 – 50 km, the slab is bending, and this group likely includes inter- and intraplate events. On the other hand, the other two deeper groups comprise intraplate earthquakes.

Lastly, for A4, we first selected the events with hypocenter depths less than 30, 40 or 60 km (the latter considered in Hardebeck (2015) as a limit depth defining the possible deepest hypocenters of the upper plate and possible megathrust events, Figure 2.2). For these events,

we then obtained their perpendicular distances to the top of the slab based on the SLAB 2.0 model. A subset of events is compiled that lie within ± 20 km perpendicularly to the slab interface, which in this study is called the megathrust window range, but likely includes events from both below and above the subduction interface. Events with slab-perpendicular distances > 20 km above and to the east of the slab interface were placed in an upper plate catalog (Hardebeck, 2015). The remainder, whose hypocenters lie > 20 km from and below the slab interface and all events deeper than 60 km, were put in an intraplate catalog. The numbers of events used for the stress inversion in each group are shown in Table 2.1. Moreover, by dividing the events according to the initial parameters' choices for A4 (megathrust window range of ± 20 km and 60-km limit depth, Figure 2.2), some events will be placed in the wrong group. For instance, some actual intraplate events likely fall into the megathrust catalog because the ± 20 km range is too wide (Figure 2.3). To test whether the event allocation based on A4 is applicable for the entire IBR, we changed the domains by (1) reducing the limit depth to 40 km, which is a typical downdip rupture limit depth of megathrust events (Oleskevich et al., 1999), and 30 km, which is the Moho depth in the IBR (Figure 2.2), and (2) narrowing the megathrust window range to ± 10 and ± 5 km from the slab interface. In addition, we selected the upper plate catalog from the division A4 with limit depth of 40 km and megathrust window ranges of ± 10 km and allocated the events based on their locations to the two major faults, CMF and KF. Subsequently, there are three subdomains, which are west-of-CMF, between-CMF-and-KF and east-of-KF. We chose this megathrust window range because the studied event hypocenter profiles show that the slab thickness is around 30 - 40 km (Figure 2.3). Thus, by using the megathrust window of ± 20 km, we might have included almost all the events within the Indian slab into the megathrust catalog. Moreover, according to Table 2.2, the combination of limit depth of 40 km and the megathrust window range of ± 10 km, seems to provide a suitable number of focal mechanisms (at least above 15 events) of each catalog for performing stress inversion.

2.4 Results

The following describes results for each of the schemes (A1 - A4) for dividing the data into domains.

A1: All Events

The result of the stress inversion for all events suggests a stress tensor consistent with the generally oblique reverse faulting mechanisms (Figure 2.4). Figure 2.1 shows a number of oblique-slip events, but there is also partitioning of dominantly reverse and dominantly strike-slip mechanisms. Overall, the inverted minimum principal stress axis (σ_3) is near-vertical acting perpendicular to the slab, while the intermediate principal stress (σ_2) is shallowly plunging westward, and the maximum principal stress (σ_1) is oriented in the NE-SW direction, roughly aligned with the relative plate motion between the Indian and Burma

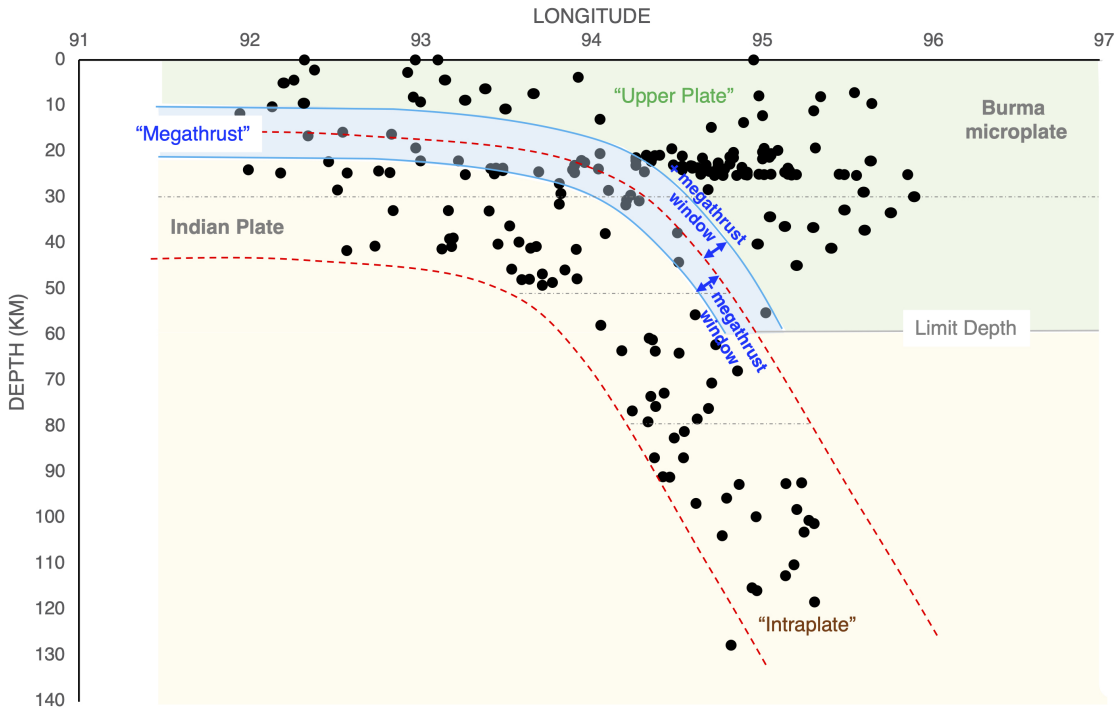

Figure 2.2: Event classification diagram following Hardebeck (2015). The black dots are the events used for the stress inversion shown schematically in a 2D section of the subduction zone. The limit depth is the possible deepest hypocenters of the upper plate and megathrust events and all events below the limit depth are assigned to the intraplate catalog. In this study, the limit depth is varied to 30, 40 and 60 km. The megathrust window range represents the perpendicular distance of the event locations to the plate interface. We consider events within 5 km, 10 km and 20 km above and below the interface, respectively. Alternative limit depths and megathrust window ranges are considered as described in Methodology and Data (Focal Mechanism Data). The gray dotted lines represent the division based on hypocenter depth ranges (A3), which includes 0 - 30, $>$ 30 - 50, $>$ 50 - 80 and $>$ 80-km subdomains.

Approaches	**Domains**	**Number of events**	**Friction**	**R**
A1	-	189	0.90	0.64
A2	18 $\leq$ Latitude $<$ 23 (Depth $\leq$ 30 km)	44	1.00	0.59
	18 $\leq$ Latitude $<$ 23 (Depth $>$ 30 km)	31	0.85	0.50
	23 $\leq$ Latitude $<$ 25 (Depth $\leq$ 30 km)	74	0.80	0.79
	23 $\leq$ Latitude $<$ 25 (Depth $>$ 30 km)	40	0.45	0.52
A3	0 $\leq$ Depth $\leq$ 30 km	118	0.90	0.71
	30 $<$ Depth $\leq$ 50 km	30	0.75	0.58
	50 $<$ Depth $\leq$ 80 km	18	1.00	0.43
	Depth $>$ 80 km	23	0.50	0.20
A4	Limit depth = 60 km and Megathrust window range of $\pm$ 20 km	38, 47, 104	0.65, 0.65, 0.80	0.13, 0.51, 0.65
	Limit depth = 40 km and Megathrust window range of $\pm$ 20 km	58, 27, 104	0.85, 0.90, 0.80	0.45, 0.63, 0.65
	Limit depth = 30 km and Megathrust window range of $\pm$ 20 km	71, 18, 100	0.90, 1.00, 0.80	0.55, 0.79, 0.64
	Limit depth = 40 km and Megathrust window range of $\pm$ 10 km	58, 16, 115	0.85, 1.00, 0.85	0.45, 0.61, 0.70
	Limit depth = 40 km and Megathrust window range of $\pm$ 5 km	60, 6, 123	0.90, 0.50, 0.85	0.50, 0.28, 0.71

Table 2.1: Number of events used for the stress inversion, frictions and R values of individual approaches. The three numbers of each subgroup in A4 are the values of intraplate, megathrust and upperplate catalogs, respectively.

Megathrust Window (km)	**Limit Depth (km)**			
	30	**40**	**60**	**No Limit Depth**
$\pm$ 5	72, 4, 113	60, 6, 123	46, 14, 129	39, 20, 130
$\pm$ 10	71, 11, 107	58 ,16, 115	41, 32, 116	24, 49, 116
$\pm$ 20	71, 18, 100	58, 27, 104	38, 47, 104	7, 78, 104

Table 2.2: The number of events for A4 Classification with different limit depth and megathrust window ranges. The numbers of events in the table are intraplate, megathrust and upper plate catalogs, respectively.

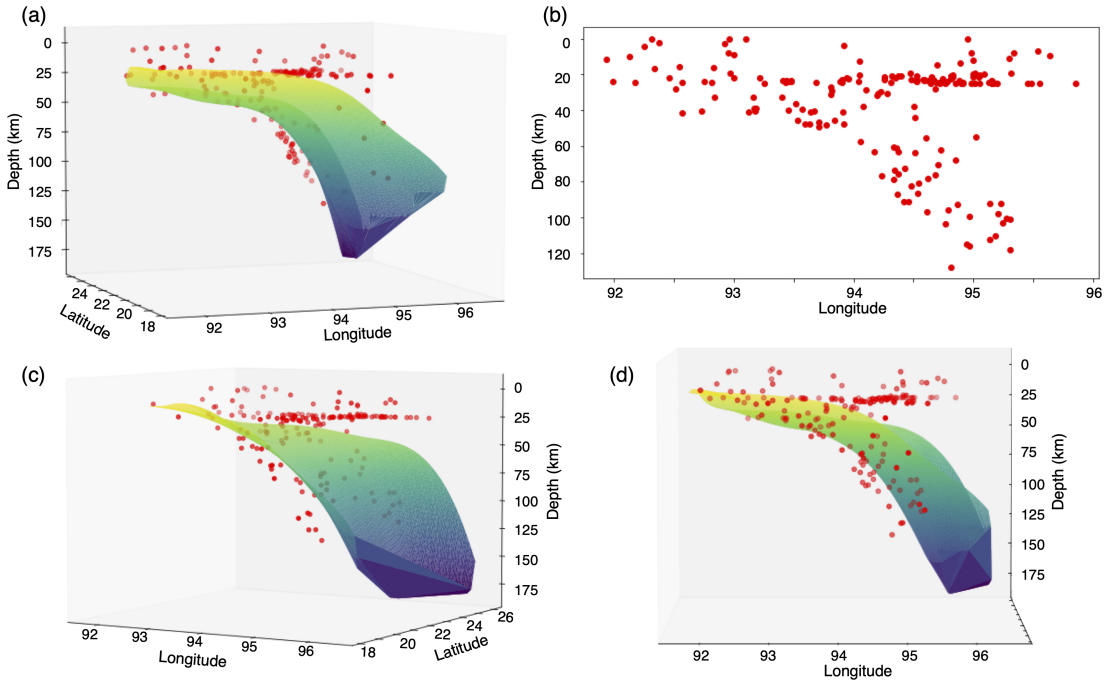

Figure 2.3: Hypocenters profiles and Indian slab geometry. (a, c, d) The events profiles (red dots) and slab plane at different angles of observation. (b) two-dimension earthquake profiles.

plates (trending $\sim$ 60°N) and parallel to the India-Sunda motion (orientating 30°N; Rangin, 2016) in this region. The inversion results for all three stress components are well-defined with formal uncertainties less than 4 degrees. Since this group includes the largest number of events, the formal uncertainties become very small. Note that if we assign larger random noise to the focal parameters, e.g., 10 and 20 degrees, we will get larger uncertainties. However, this does not mean that there is no variation in the state of stress across the IBR.

A2: Latitudinal Range Division

By dividing the events into four groups (Table 2.1), we observe a modest but systematic change in the stress inversion results from north to south of both depth ranges (Figure 2.5). The two greatest variations in the inversion results of A2 are the average directions of the σ_3 and σ_1 axes at depths below 30 km, which differ by 30.9 and 30.1 degrees, respectively. σ_1 plunges more steeply in the southern IBR. On the other hand, the σ_3 orientation changes from NW-SE in the north to E-W in the south. Nonetheless, the overall orientations of the principal stresses remain similar to those from all events (σ_1 = slab-strike-parallel stress, σ_2 = stress plunging to the northwest, σ_3 = steeply east plunging stress), and we still observe the oblique reverse stress tensor from the northern to southern IBR.

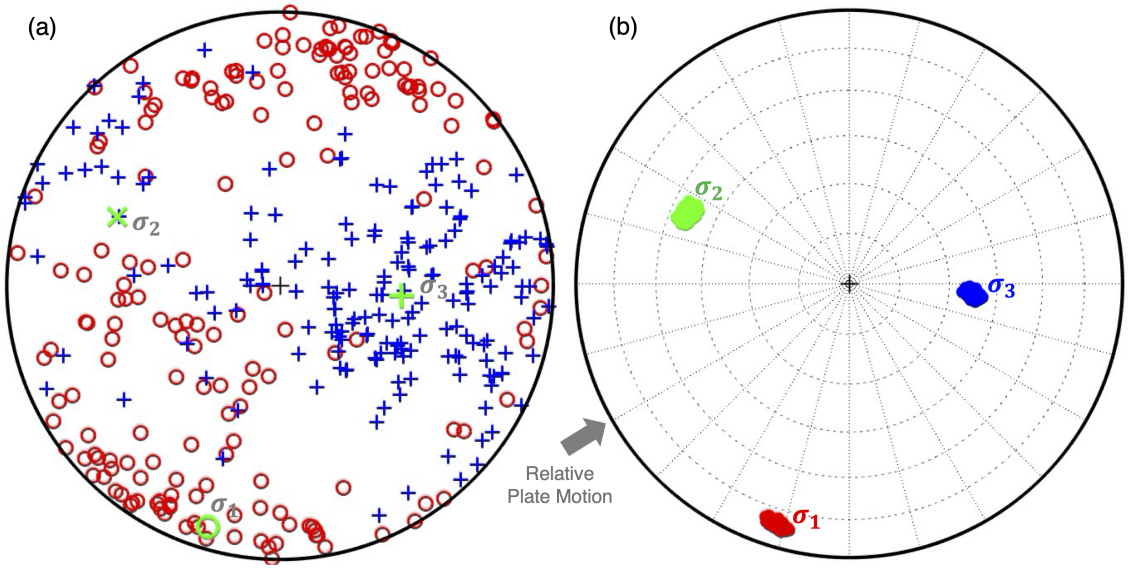

Figure 2.4: Stress inversion results for all 189 events from the ISC, GCMT, Hurukawa et al. (2012) and Chit Thet Mon et al. (2020) catalogs in the IBR region. (a) P-T axes of the studied events. Blue "+" signs represent the T-axes while the red circles, "o", indicate P-axes. (b) Principal stress directions from stress inversion. Generally, the result suggests an oblique-reverse faulting environment. This likely reflects contributions from a more heterogeneous stress field across the region. The gray arrow indicates the plate motions relative to the eastern Burma microplate obtained from an elastic block model by Mallick et al. (2019).

A3: Hypocenter Depth Range Division

We observe that partitioning the data into depth domains significantly affects the stress inversion results, showing the plunge of σ_3 systematically increasing with depth (Figure 2.6). The steepening of the σ_3 axis follows the increasing Indian slab dip angle (Figure 2.6e). However, for the shallow (0 - 30 km) domain, σ_3 is steeply plunging, possibly because these shallow earthquakes are mostly upper plate events and may reflect the thrust-faulting environment. On the other hand, in the 30 - 50 km depth range the inversion result suggests a stress tensor that is associated with strike-slip faulting. For the other two deeper ranges, the principal stress orientations remain similar to the previous results for A1 and A2. Moreover, the results for the σ_1 and σ_2 directions of events in the 50 - 80 km and $>$ 80 km depth domains are not well defined ($>$ 45 degrees of uncertainties). It is not certain what might cause these relatively high uncertainties since the σ_3 result for these groups is still well-defined.

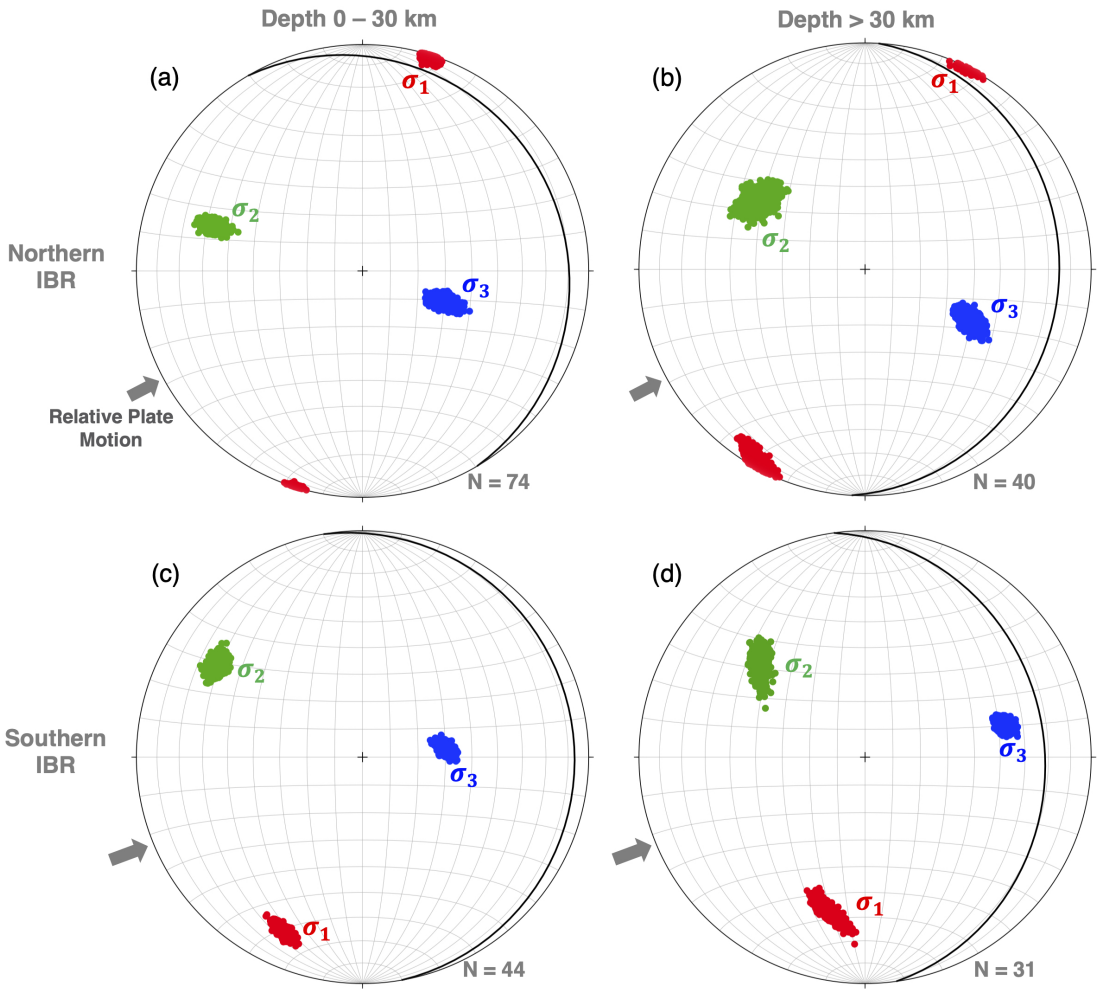

Figure 2.5: Stress inversion results of the studied events in two latitudinal domains and two depth ranges (A2). (a, b) the principal stress orientations between 23° N and 25° N, or northern IBR and the depth ranges of 0 - 30 and > 30 km, respectively. (c, d) the principal stress orientations between 18° N and 23° N, or southern IBR, and the depth ranges of 0 - 30 and > 30 km, respectively. There are 74, 40, 44 and 31 events used for the stress inversion of groups a, b, c, and d respectively. The gray arrow indicates the plate motions relative to the eastern Burma microplate obtained from an elastic block model by Mallick et al. (2019).

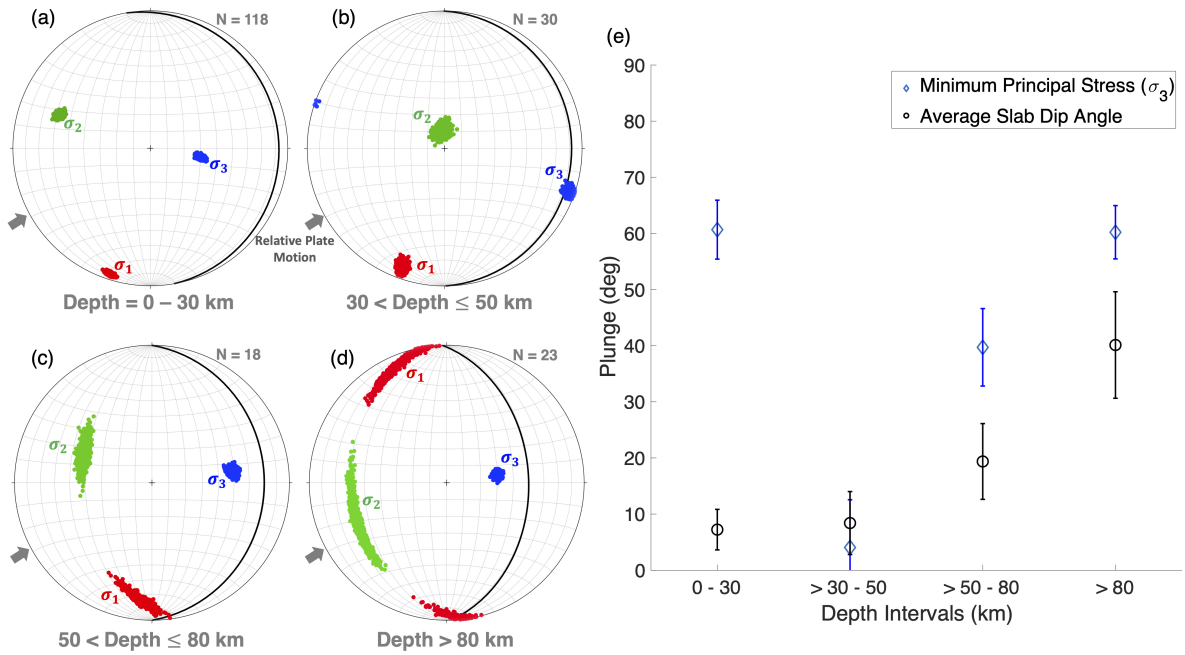

Figure 2.6: Stress inversion results of the studied events for a range of hypocenter depth domains (A3). (a, b, c, d) Inversion solutions for depth ranges of 0 - 30, > 30 - 50, > 50 - 80 and > 80 km, respectively. The numbers of events used for the stress inversion of a, b, c, and d are 118, 30, 18, and 23, respectively. The black lines on the Stereonets represent the associated slab geometries from Slab 2.0. The gray arrow indicates the plate motions relative to the eastern Burma microplate obtained from an elastic block model by Mallick et al. (2019). (e) The average σ_3 (blue diamonds) plunges and the average slab dip angles (black circles) of individual domains (a, b, c, d) are shown with their 1-sigma error bars.

A4: Division by Perpendicular Distance from the Slab Interface (PDSI)

In this division, we first apply Hardebeck (2015)'s method to classify the events into intraplate, megathrust and upper-plate catalogs. However, the limit depth of 60 km and the megathrust window range of ± 20 km used in Hardebeck (2015) may not be suitable for our study region. Thus, we vary these two parameters in order to test their impact on our results.

PDSI (limit depth = 60 km and megathrust window range of ± 20 km)

By dividing the events into three subsets according to their locations with respect to the plate interface, we find that for the intraplate and upper plate catalogs, the dominant stress tensor is oblique reverse, and σ_3 is steeply eastward plunging, similar to previous results

(Figure 2.7b, d). σ_1 and σ_2 for these two catalog inversion results are slab-strike parallel and horizontal stresses, respectively. The σ_1 of these two catalogs are slightly different but are generally oriented in the N-S direction consistent with the plate motion (i.e., Rangin, 2017). In contrast, in the megathrust window subset (Figure 2.7c), the dominant stress tensor is consistent with a strike-slip regime (near vertical σ_2). Although the σ_1 orientation is similar to the ones of the intraplate and upper plate catalogs, σ_2 is oriented near-vertical and σ_3 plunges more shallowly, becoming a near-horizontal stress.

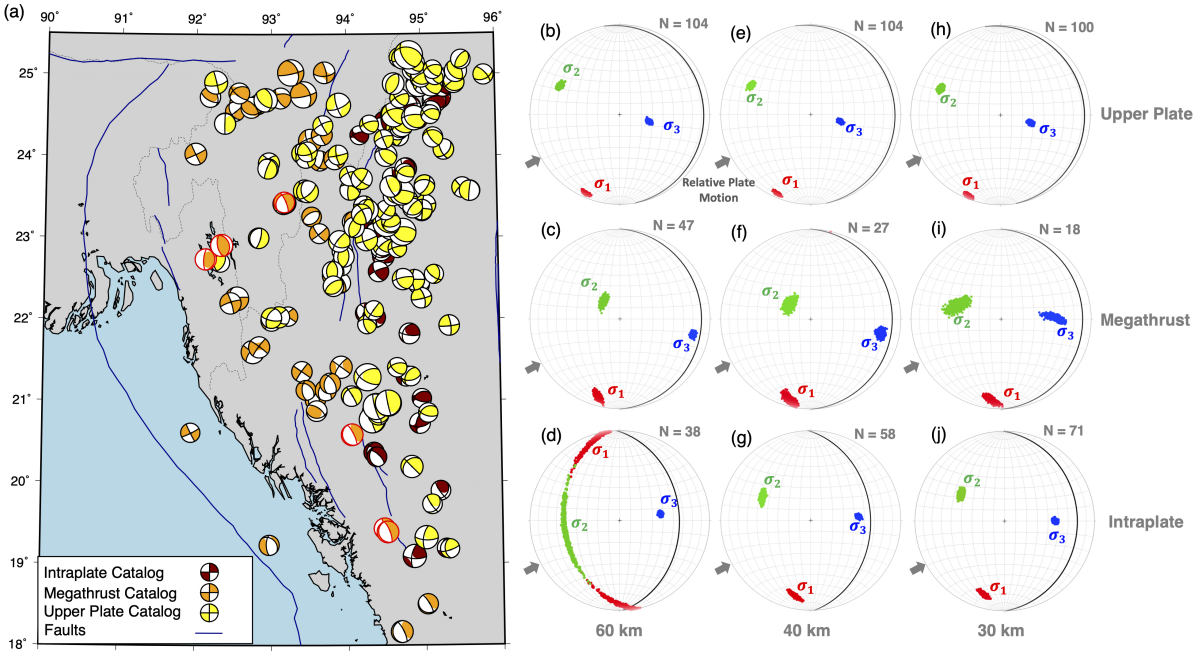

Figure 2.7: Stress inversion results of earthquakes divided into three groups based on their shortest (perpendicular) distances to the top of the subducting slab, varying the limit depth from 60 to 40 and to 30 km. (a) Map of events in the three subdomains. The megathrust subset includes events that are within ± 20 km from the slab interface, and the limit depth is assigned to 60 km. The focal mechanisms in the megathrust catalog marked by red outlines have shallow E-dipping nodal planes suggesting that they could potentially occur on the megathrust. (b, c, d) Inversion results for the intraplate, megathrust, and upper plate catalogs, respectively, mentioned in Results – A4 with limit depth of 60km. (e, f, g) the inversion results of the intraplate, megathrust, and upper plate catalogs for the limit depth of 40 km. (h, i, j) the inversion results of the intraplate, megathrust, and upper plate catalogs for the limit depth of 30 km. The black lines on the Stereonets represent the slab geometries. The gray arrow indicates the plate motions relative to the eastern Burma microplate obtained from an elastic block model by Mallick et al. (2019).

PDSI (limit depth = 40 and 30 km and megathrust window range of ± 20 km)

By changing the limit depth to 40 and 30 km, the σ_1 and σ_2 inversion results of the intraplate catalog become more well-defined than the results for the limit depth of 60 km (Figure 2.7d, g, j). The σ_3 orientation slightly changes and plunges a bit shallower. The inversion results of the upper plate catalog are similar (Figure 2.7b, e, h). On the other hand, for the megathrust catalog (Figure 2.7c, f, i), the σ_3 of the limit-depth-of-30-km domain plunges steeper than the other two groups, while the σ_2 plunge gets shallower, and σ_1 stays the same.

PDSI (limit depth = 40 km and megathrust window range of ± 10 km and ± 5 km)

Altering the megathrust window range to ± 10 and ± 5 km does not substantially change the inversion results of the upper plate and the intraplate catalogs (Figure 2.8). However, the σ_1 and σ_2 results of the megathrust catalog become less defined, especially when the megathrust window range is ± 5 km. This is possibly because the number of the focal mechanisms is very low (6 events). Generally, the number of focal mechanisms in a domain should be around 20 for a reliable stress inversion with an average error of principal stress direction results of less than 12 degrees (Vavryčuk, 2014). Overall, the stress inversion result of the megathrust domain suggests a dominance of strike-slip moment tensors, while the solutions of the intraplate and upper plate subsets indicate oblique-reverse faulting.

Upper Plate Catalog - PDSI (limit depth = 40 km and megathrust window range of ± 10 km)

By only considering the upper plate catalog, and dividing the events based on their locations to the two major faults, CMF and KF, the stress inversion results of all three divisions suggests that the $\sigma_1$orientates in NE-SW (Figure 2.9). The σ_2 and σ_3 of the west-of-CMF domain are steeply plunging toward NW and shallowly plunging toward SE, respectively. Similarly, the σ_3 of the east-of-KF division orientates in a similar direction to the one of the west-of-CMF domain but plunges more steeply. The σ_2 of the east-of-KF domain is shallowly plunging toward the NW. In addition, the σ_2 of the between-CMF-and-KF group strikes in NW-SE, while the σ_3 becomes vertical. Accordingly, the solutions of the west-of-CMF and east-of-KF indicate oblique reverse faulting, while the result of the between-CMF-and-KF suggests reverse faulting style.

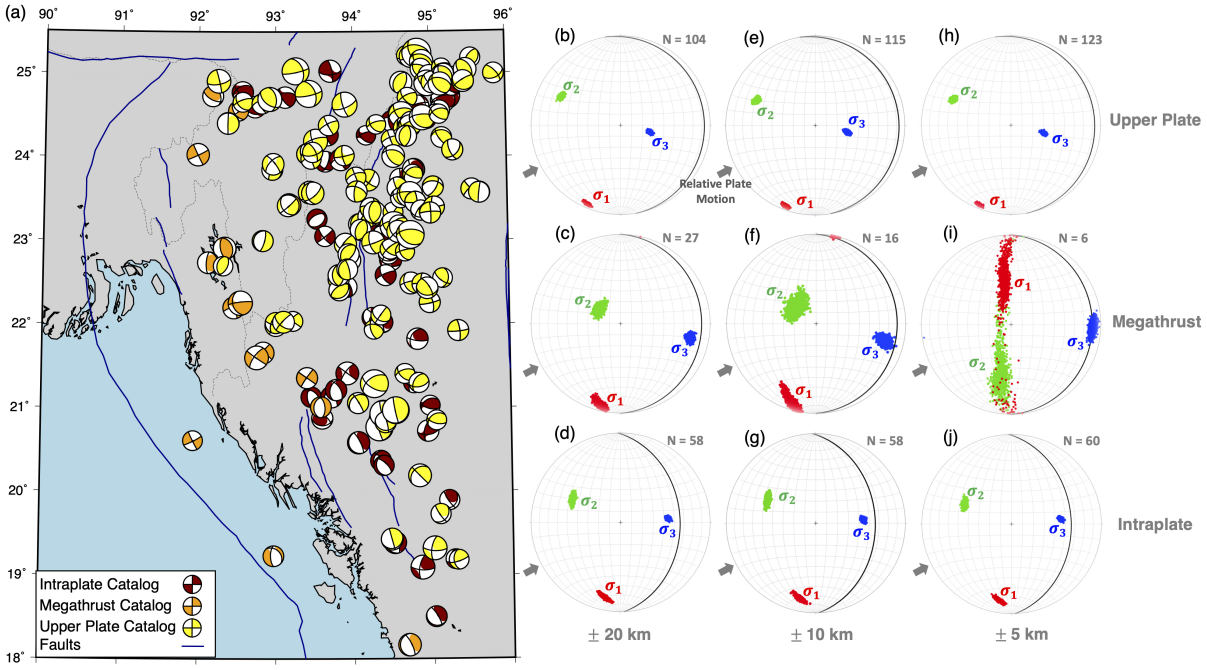

Figure 2.8: Stress inversion results of earthquakes divided into three groups based on their shortest (perpendicular) distances to the top of the subducting slab, altering the megathrust window range from ± 20 to ± 10 and to ± 5 km. (a) Map of events in the three subdomains. The megathrust catalog includes events that are within ± 10 km from the slab interface, and the limit depth is assigned to 40 km. (b, c, d) Inversion results for the intraplate, megathrust, and upper plate catalogs, respectively. Here, we consider the megathrust window ranges of ± 20 km and the limit depth of 40 km. (e, f, g) Inversion results for the intraplate, megathrust, and upper plate catalogs, respectively. For this group, we assign the megathrust window ranges to ± 10 km and the limit depth to 40 km. (h, i, j) Inversion results for the intraplate, megathrust, and upper plate catalogs, respectively. Here, we set the megathrust window ranges to ± 5 km and the limit depth to 40 km. The black lines on the Stereonets represent the slab geometries. The gray arrow indicates the plate motions relative to the eastern Burma microplate obtained from an elastic block model by Mallick et al. (2019).

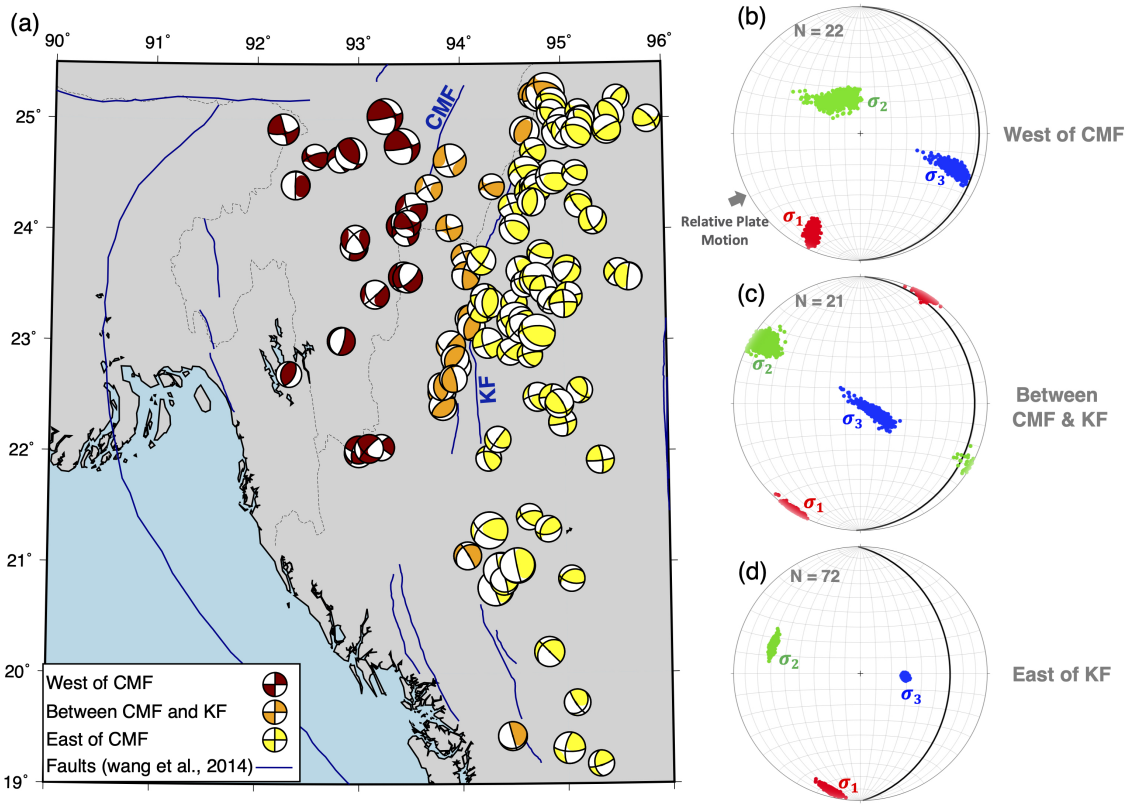

Figure 2.9: Stress inversion results of upper plate earthquakes (using limit depth of 40 km and megathrust window of ± 10 km) divided into three groups based on their locations from two major faults, CMF and KF. (a) Map of events occurring in the three subdomains, which are west of CMF, between CMF and KF, and east of KF. (b, c, d) Inversion results for the west-of-CMF, between-CMF-and-KF, and east-of-KF domains, respectively. The black lines on the Stereonets represent the slab geometries. The gray arrow indicates the plate motions relative to the eastern Burma microplate obtained from an elastic block model by Mallick et al. (2019).

2.5 Discussion

Stress Variation across the IBR

Considering different domains, dividing the events into latitudinal, depth, and slab-distance ranges, helps reveal variations in the stress state across the study area. Overall, by allocating the events to different subdomains, we find that the stress state across the IBR varies systematically along the subducting slab. The σ_1 is predominantly orientated NNE-SSW corresponding to the plate motion, the σ_2 is plunging shallowly toward the west, and the σ_3 plunges steeply, indicative of downdip tension plunging approximately at the slab dip angle. However, for domain A3, the σ_3 plunges shallowly at depth $> 30 - 50$ km while σ_2 becomes vertical (Figure 2.6b). Similarly, the σ_3 orientations of the megathrust window subsets in A4 are nearly horizontal while σ_2 is close to vertical, suggesting a strike-slip faulting style (Figures 2.7c,f,i and 2.8c,f,i). The inferred stress directions of the events near the plate interface are different from the inversion results of the intraplate and IBR forearc domains which indicate a stress environment favoring oblique reverse faulting.

In addition, by further dividing the events in the upper plate catalog of the A4 division (limit depth of 40 km and megathrust window range of $\pm$ 10 km) based on their occurrence locations to the CMF and KF and performing stress inversion of each group (Figure 2.9), we find that east of KF the stress tensor is consistent with the oblique reverse faulting mechanisms. This result supports the finding of Chit Thet Mon et al. (2020) that there is a dominance of the strike-slip deformation in the east of the KF and is consistent to the characteristics of the active faults in Central Myanmar, i.e. Pyay Fault, which is a reverse fault with a strike-slip component (Lin Thu Aung et al., 2020). Moreover, Chit Thet Mon et al. (2020) indicate that there is predominantly shortening in the west of the KF. However, we find that in between the KF and CMF, σ_1 orientates in NE-SW and does not indicate EW shortening (Figure 2.9c). Even though the obtained stress tensor suggests reverse faulting, the maximum principal stress direction is not similar to what Chit Thet Mon et al. (2020) suggest. Therefore, we further performed a stress inversion of the nine focal mechanisms from Chi Thet Mon et al. (2020) that occurred between the CMF and KF. We found that the σ_1 orientation is approximately NS, which is consistent with our previous result (Figure 2.10). However, the uncertainties of the σ_1 and σ_2 solutions are high ($\sim$ 70 degrees) due to the low number of events. Despite this inversion result, there are four out of nine events indicating EW maximum principal stress (Figure 2.10a). In addition, in the west of the CMF, our stress inversion result suggests an oblique reverse faulting mechanism. Accordingly, our findings in the east of the KF agree with the observation made by Lin Thu Aung et al. (2020) and Chit Thet Mon et al. (2020).

Overall, for all studied domains, the stress inversion results generally suggest oblique reverse faulting style, and the σ_1 orientation seems to be always consistent striking in NNE-SSW (Figure 2.11). However, we still observe variation in orientations of σ_2 and σ_3 of some domains indicating reverse (i.e., between-CMF-and-KF subdomain) and strike-slip faulting styles (e.g., $>$ 30-50-km depth range domain and megathrust catalog).

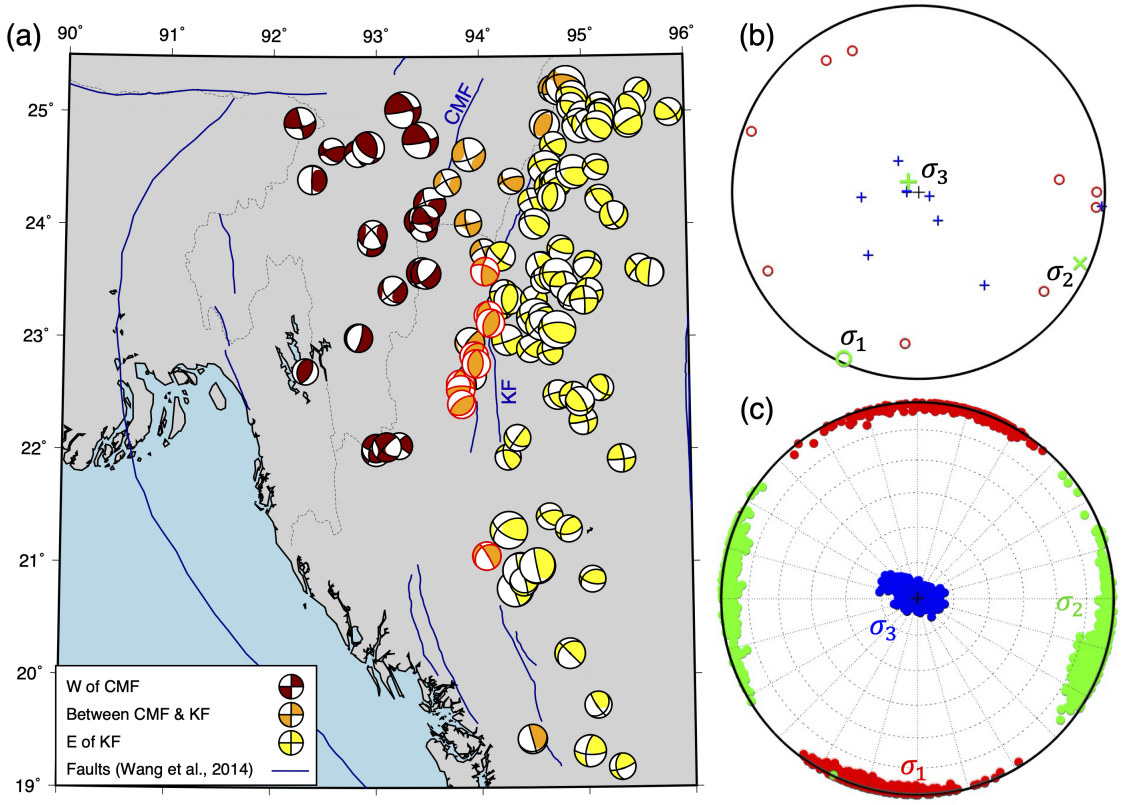

Figure 2.10: Stress inversion results of the events from Chit Thet Mon et al. (2020) occurring between the CMF and KF (indicated by red outlines in a). (a) Map of events occurring in the three subdomains, which are west of CMF, between CMF and KF, and east of KF. The focal mechanisms with red perimeters are the ones used for the stress inversion, and the results are shown in (b) and (c). (b) P-T axes and average principal stress orientations. (c) Inversion results of the principal stress orientations.

Upper Plate Stress

According to the A3 (depth = 0 – 30 km) and A4 (upper plate catalog) results, the inversion solutions suggest an oblique reverse mechanism, and the results appear well-defined (< 4 degrees of uncertainty). The σ_1 is oriented NE-SW and sub-parallel to the plate motion direction. The σ_2 is shallowly plunging toward the west while the σ_3 is near-vertical. In addition, by dividing the upper plate catalog based on their occurrence locations to the major faults, CMF and KF, we observe that the dominant stress tensors in the east of KF and in the west of CMF are similar in both domains associated with oblique reverse faulting (Figure 2.9). In contrast, the stress tensor of the between-KF-and-CMF division indicates a reverse faulting mechanism. The σ_1 of all three domains strikes similarly in the NE-SW direction. However, the σ_2 and σ_3 orientations of eastern KF and western CMF are different from the result of the between-KF-and-CMF domain. Overall, our findings are consistent with the observation of the dominant active strike-slip deformation in the east of KF (Chit Thet Mon et al., 2020) and the characteristics of Pyay Fault in Central Myanmar studied by Lin Thu Aung et al. (2020).

Additionally, the σ_1 orientation in the IBR upper plate region is similar to the stress of other forearc regions in oblique subduction zones, i.e. northern Cascadia and central Nankai (Wang, 2000). The slab-strike-parallel σ_1 seems to be a typical feature in the upper plate of a highly oblique subduction zones. The orientation of σ_1 appears to be consistent with the convergence direction and may be governed by the degree of the obliquity of the subduction zone. Generally, the upper plate σ_1 orientations in oblique subduction zones are different from the ones of non-oblique (very low obliquity) subduction zones, e.g. Mexico, Philippines, and Sumatra where σ_1 is a sub-horizontal stress plunging trenchward (Hardebeck, 2015).

Indian Slab Stress State

According to the inversion results from A3, the σ_3 orientations below 30 km consistently indicate downdip tension (Figures 2.6e and 2.11). The σ_3 direction results are always well-defined suggesting that the driving force of this subduction region is a net slab pull. The stress inversion of these data subsets suggests downdip tension for all depths below 30 km. This indicates that the net slab pull governs the slab stresses even at shallow depths.

In addition, the A4 results of the megathrust and intraplate catalogs indicate that σ_1 strikes approximately N-S and is a slab strike-parallel stress. In general, for oblique subduction zones, σ_1 of the upper plate will be affected by the convergence or plate motion, but the direction of σ_1 at greater depths may vary, as observed in the northern Cascadia and central Nankai (Wada et al., 2010; Wang et al., 2004; Wang 2000). However, the σ_1 direction in all depth domains in the IBR is always consistent and parallel to the Indian slab strike (i.e., inversion results of deeper depth ranges in A3 and A4). This indicates that the stress state in this region is dominated by the compression due to the northward pushing slab through the mantle.

Overall, the stress inversion results of the megathrust catalogs in the A4 suggest a strike-slip faulting style (σ_2 is near-vertical). While we might expect to find a thrust faulting style as a result of the stress inversion for the events near the megathrust, which would also be expected based on the geodetic modeling results (e.g., Mallick et al., etc.), this is not the case in the IBR. As we change the limit depth to 40 and 30 km as described in Results (A4) and Figure 2.7, the σ_2 plunges slightly shallower while σ_3 becomes more steeply plunging. This indicates that by assigning the limit depth as 60 km, we might have included more of the intraplate events in our megathrust catalogs.

The observed oblique reverse faulting style could reflect oblique subduction, however, most of the events in the megathrust catalog are likely not interface events. There are only six events that have shallow E-dipping nodal planes (Figure 2.7a) suggesting that they could potentially occur on the megathrust. According to the study of Shyu et al. (2018), it is likely that the recurrence interval of great megathrust events is 800 - 900 years. Thus, it is possible that the events occurring in the time period of our study are not representative of the kinematics of eventual plate interface events. This is similar to the Cascadia subduction zone which also features hardly any plate interface events but is known to host M∼9 megathrust ruptures (e.g., Wang and Tréhu, 2016). More events and improved event locations may be needed to better illuminate the state of stress near the plate interface.

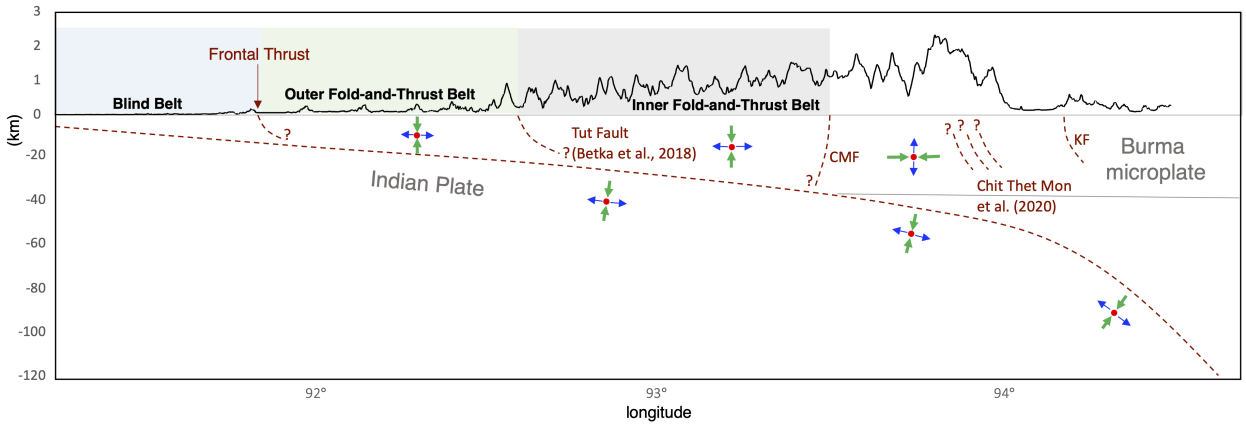

Figure 2.11: Diagram summarizing the stress inversion results across the IBR and in the Indian Slab. The green and blue arrows represent the directions of σ_2 and σ_3, respectively. The red circles indicate the direction of σ_1 that orientates in the NS direction.

2.6 Conclusions

The overall trends of the principal stress directions in the IBR suggest that σ_1 is a slab strike-parallel stress, σ_2 is plunging westward at variable angles, and σ_3 is steeply eastward

plunging. However, for the megathrust catalog, σ_3 becomes horizontal stress, while σ_2 is vertical. For the upper plate catalog, the principal stress orientations of the events in the east of KF and west of the CMF are modestly different, but they are greatly distinct from the solution of the events occurring in between the CMF and KF. The inversion results of the east-of-the-KF and west-of-the-CMF catalogs appear to be corresponding to the obliquely convergent plate motion. On the other hand, the stress tensor of the between-KF-and-CMF domain seems to be associated with the reverse faulting with σ_1 striking in N-S direction. This is different from the suggestion of E-W shortening proposed by Chit Thet Mon et al. (2020). By considering the state of stress within the subducting slab, the σ_1 direction is approximately in the N-S even at greater depths. This indicates the compression due to the northward pushing of the slab through the mantle. In addition, the inversion results suggest downdip tension at all depth ranges below the upper plate region. This indicates that the driving force of this subduction zone is a net slab pull. According to this observation, there is a possibility that the IBR megathrust may generate big earthquakes, even though there is currently little, if any, seismicity on the plate interface.

2.7 Data and Resources

Maps were created using ArcGIS (https://www.arcgis.com/index.html, last accessed December 2020) and Generic Mapping Tools (GMT) of Wessel et al. (2013). Earthquake mechanisms were obtained from the USGS National Earthquake Information Center (NEIC, https://earthquake.usgs.gov/earthquakes/search/, last accessed January 2020), Global Centroid Moment Tensor Project (GCMT, https://www.globalcmt.org/CMTsearch.html, last accessed January 2020), International Seismological Centre (ISC, http://www.isc.ac.uk/iscbulletin/search/catalogue/, last accessed January 2020), Hurukawa et al. (2012) and Chit Thet Mon et al., (2020) (https://agupubs.onlinelibrary.wiley.com/doi/full/10.1029/2019GL086236, last accessed May 2020). The stress inversions and the solutions were performed and plotted using MATLAB-based stress inversion code (STRESSINVERSE v1.1, https://www.ig.cas.cz/en/stress-inverse/, last accessed December 2020) of Vavryčuk, (2014). The data of slab geometry is from Hayes et al. (2018) (https://www.sciencebase.gov/catalog/item/5aa1b00ee4b0b1c392e86467/, last accessed August 2020).

Chapter 3

Geomorphic expressions of active tectonics across the Indo-Burma Range

Published as: Maneerat, P. and Bürgmann, R., 2022. Geomorphic expressions of active tectonics across the Indo-Burma Range. Journal of Asian Earth Sciences, 223, p.105008.

3.1 Abstract

The Indo-Burma Range (IBR) is an accretionary complex associated with the oblique subduction zone between India and the Burma microplate. It remains an outstanding question whether the ongoing plate-boundary deformation involves active subduction of the Indian plate. To study the tectonics in this region, we investigate drainage divide stability and the topographic expression of active tectonics across the IBR. We extract elevation data from the 30 $\times$ 30 m SRTM digital elevation model and identify streams, drainage divides and basins. We select the divide segments to construct and evaluate divide stability using the Gilbert metrics and χ values of the channel heads located on both sides of the divide portions. We calculate several geomorphic indices, including basin-scale (hypsometry and relief) and stream-scale (normalized steepness index [k_{sn}]) measures to reveal tectonic uplift patterns. We find that most of the divide segments are static, allowing us to study the morphometry of streams and drainage as indicators of spatial variation in tectonic uplift in the context of large-scale variations of precipitation and lithology. Our morphometric results support ongoing tectonic uplift distributed across the inner belt of the IBR, and they cannot be explained by variations in precipitation or lithology. The eastern region is characterized by higher relief, hypsometry and k_{sn} compared to the western outer belt. While the active deformation front lies far to the west, the inferred higher uplift rates in the eastern range suggest active out-of-sequence thrusts in the inner belt of the IBR that splay off from the active megathrust.

3.2 Introduction

The Indo-Burma Range (IBR, Figure 3.1) represents the forearc of an oblique subduction zone that formed due to the India-Eurasia collision starting in the Paleogene (Rangin et al., 2013; Mitchell, 1993). The highly oblique convergence has produced components of both EW shortening and NS strike-slip deformation (e.g., Steckler et al., 2016; Mallick et al., 2019; Panda et al., 2020). This is consistent with the observation of NS anticlines accommodating EW contraction and stream offsets, suggesting dextral offsets on several NS striking faults, such as the Churachandpur Mao Fault (CMF; Wang et al., 2014). Betka et al. (2018) and Rangin (2017) find that there is only pure convergent motion in the western anticlinal structures or outer belt, while partitioned strike-slip is observed in the eastern or inner belt. However, beyond the large-scale picture of partitioned oblique convergence, the details of the active tectonics across this region remain uncertain.

To help better understand the active tectonics of the region, several research groups used interseismic GPS measurements, and some employed elastic dislocation models to study the first-order fault kinematics and strain partitioning across the IBR. The southwest-directed surface velocities with respect to the Indian plate (Figure 3.2a) decrease and turn more westerly from the eastern to the western IBR, which is consistent with distributed plate boundary deformation across this region. This is partly due to deformation spread across multiple active faults but also may reflect the broad elastic strain fields of a deeply locked subduction thrust and other major faults. Published studies assumed different plate configurations and fault kinematics and thus have come to different conclusions with respect to fault slip rates and the distribution of convergence across the plate boundary. Socquet et al. (2006) suggest that the 35 mm/yr differential India-Sunda plate motion is mainly partitioned between the Arakan megathrust (∼14 mm/yr thrust motion), the Kabaw Fault (KF, 9 mm/yr thrust motion), and the Sagaing Fault (SF, 18 mm/yr right-lateral strike slip). In contrast, Steckler et al. (2016) use simple dislocation models to infer that 46 mm/yr of differential motion between the Indian subcontinent and the Shan Plateau is accommodated by the megathrust (∼13-17 mm/yr), the SF (∼21 mm/yr), the CMF (∼10 mm/yr right-lateral strike slip), and the KF (∼4-5 mm/yr). Relying on elastic block modeling, Mallick et al. (2019) propose that the convergent component across the IBR is in the range of 12 - 24 mm/yr and the entire dextral motion amounts to about 25 - 32 mm/yr. In their block models, nearly all the convergence is accommodated by the megathrust, which is thus potentially capable of generating great earthquakes in the future, while the SF, and possibly the CMF, accommodate most of the strike-slip component. In contrast, Rao and Kumar (1999) and Gahalaut et al. (2013) indicate that the strike-slip faults, the CMF and SF, can fully accommodate the plate motion, including the small convergent component and the former subduction thrust is now inactive. Most recently, Panda et al. (2020) reevaluated published GPS velocities and used dislocation modeling to suggest that the 37 mm/yr India-Sunda plate motion is accommodated by SF (∼18 mm/yr) and CMF (∼17 mm/yr) strike-slip faulting and subduction (∼7 mm/yr), which they suggest may involve either a fully locked or aseismically creeping detachment. Accordingly, all the geodetic studies found some amount of E-W contraction.

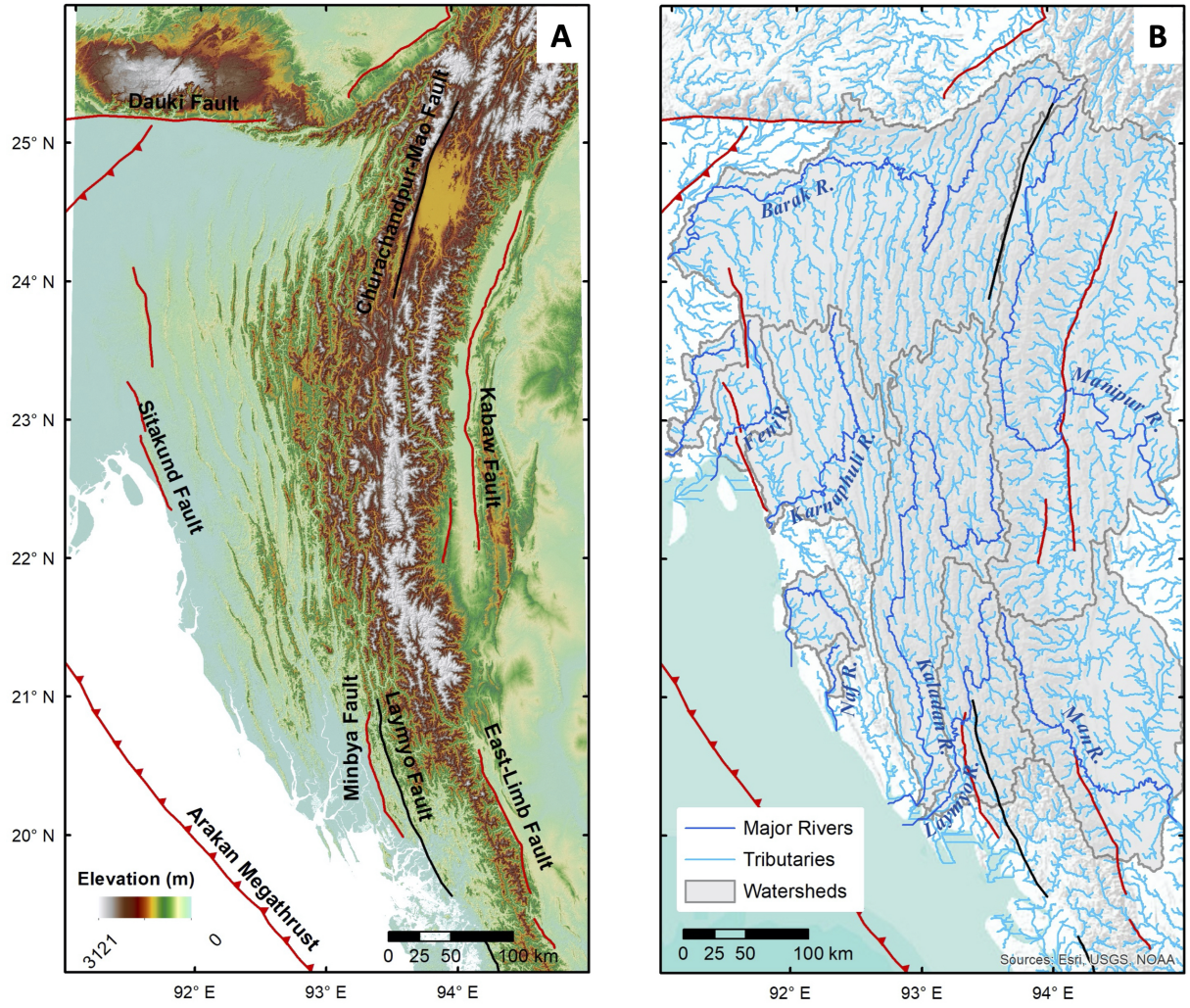

Figure 3.1: Setting of IBR study region. (a) Morphology of the IBR and mapped active faults (Wang et al., 2014; Betka et al., 2018). The black lines represent strike-slip faults, and red lines indicate thrust/reverse faults. (b) Major rivers in the IBR (dark blue lines) and their tributaries (light blue) used for stream-scale geomorphic indices. The polygons outline the watersheds of the major rivers.

However, the location where the convergent component is accommodated is still not certain. Given the disagreements between these previous studies relying on similar data constraints, it is difficult to fully explain the active tectonics in this region by only considering interseismic deformation data and elastic dislocation models.

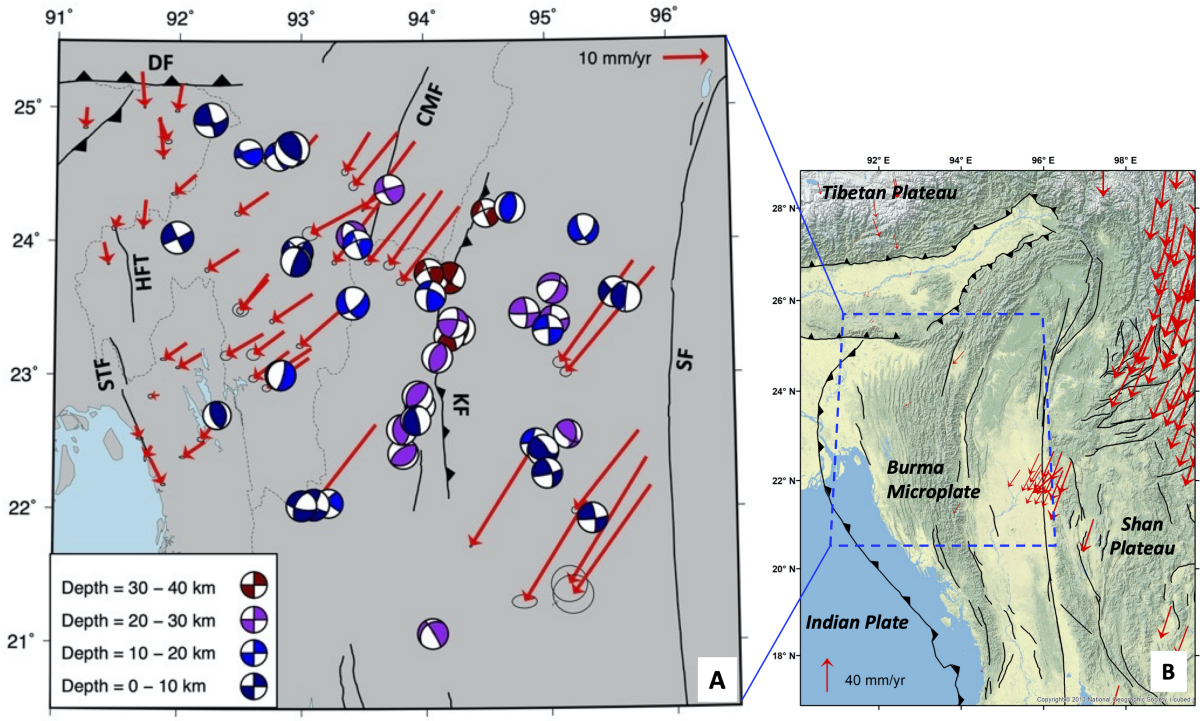

Figure 3.2: Plate boundaries and surface velocity maps. (a) GPS measured surface velocities relative to the India plate (Kreemer et al., 2014; Steckler et al., 2016; Mallick et al., 2019) and focal mechanisms of crustal earthquakes compiled from ISC, GCMT, Hurukawa et al. (2012), and Chit Thet Mon et al. (2020). The surface velocities (red arrows) show oblique convergent motion across the IBR. The black lines are active faults from Wang et al. (2014); DF = Dauki Fault, STF = Satikund Fault, HFT = Himalayan Frontal Thrust, CMF = Churachanpur-Mao Fault, KF = Kabaw Fault, SF = Sagaing Fault. (b) Zoomed-out panel showing regional plates. The red arrows represent surface velocities relative to India (Banerjee et al., 2008).

Several studies have investigated seismicity data to characterize the kinematics of the IBR subduction zone. Rangin et al., (2013) employed information on the active strain field, seismic focal mechanisms and seismic reflection profiles to investigate anticlinal deformation in the IBR and how it relates to the subduction zone. They propose that the anticlines reflect EW shortening that is largely driven by the gravitational forces associated with the collapse of the Tibetan Plateau. Similarly, Copley and McKenzie (2007) emphasize the role

of gravitationally driven lower-crustal flow across the IBR. In this view, the strike-slip faults accommodate the plate motion, and the subduction zone is no longer active. On the other hand, Chit Thet Mon et al., (2020) support the idea that the subduction is still active. They determined focal mechanisms of 40 smaller-magnitude earthquakes and propose that there are active thrust faults extending down to the Moho located between the CMF and KF. These thrust faults accommodate EW shortening and may provide evidence for out-of-sequence faulting governed by the subduction thrust.

Interseismic velocity fields and the distribution and mechanisms of earthquakes only provide a snapshot of active plate boundary deformation and are not able to uniquely resolve slip rates on individual faults that are locked down to substantial depths. Long-term processes such as the active redistribution of sediments (Steckler et al., 2008; Krien et al., 2019) and lower-crustal flow (Rangin et al., 2013; Copley and McKenzie, 2007; Maurin and Rangin, 2009) may also contribute to surface deformation in the IBR. Therefore, estimates of surface deformation that integrate over multiple earthquake cycles are needed to provide meaningful constraints on the overall pattern of active tectonics.

In this study, we examine the drainage divide stability across the IBR to assess to what degree our study region is in equilibrium, thus allowing the morphometric indices of streams and drainage basins to be interpreted as in the context of spatially variable tectonic uplift rates. We use indicators of active uplift and deformation from geomorphology to better understand the tectonics in the IBR at time scales spanning many earthquake cycles. In addition to tectonic uplift, other factors are known to influence the geomorphic expression of an area. In particular, variations in lithology and precipitation can also affect landscape evolution (e.g., Kirby and Whipple, 2012). Here, we use available geologic and annual precipitation maps (Figure 3.3) to assess the possible contribution of lithologic and climatic factors to the topographic expression of the area. We rely on available digital topography and morphometric analysis to complement geodetic and seismologic observations and gain improved understanding of the distribution of active uplift and convergence across the IBR. Quantitatively investigating the landform characteristics is useful for hazard assessment and will help us better understand active faulting mechanisms, surface deformation and the evolution of drainage systems in this tectonic setting.

3.3 Methods

We utilize geographical information system software (ArcGIS) and other computational tools (TopoToolbox, Schwanghart and Scherler, 2014; DivideTools, Forte and Whipple, 2018) for the analysis of relief and stream flow from digital elevation model data (DEM). We use a DEM with a 30 $\times$ 30m pixel size constructed from radar interferometric data collected by the NASA Shuttle Radar Topography Mission (SRTM) and distributed by the U.S. Geological Survey. To assess the role of DEM resolution and quality, we examined differences in elevation data and derived geomorphic indices from the 12 $\times$ 12m TanDEM-X and the 30 $\times$ 30m SRTM DEM. Because of the use of a different datum (orthometric heights with respect to

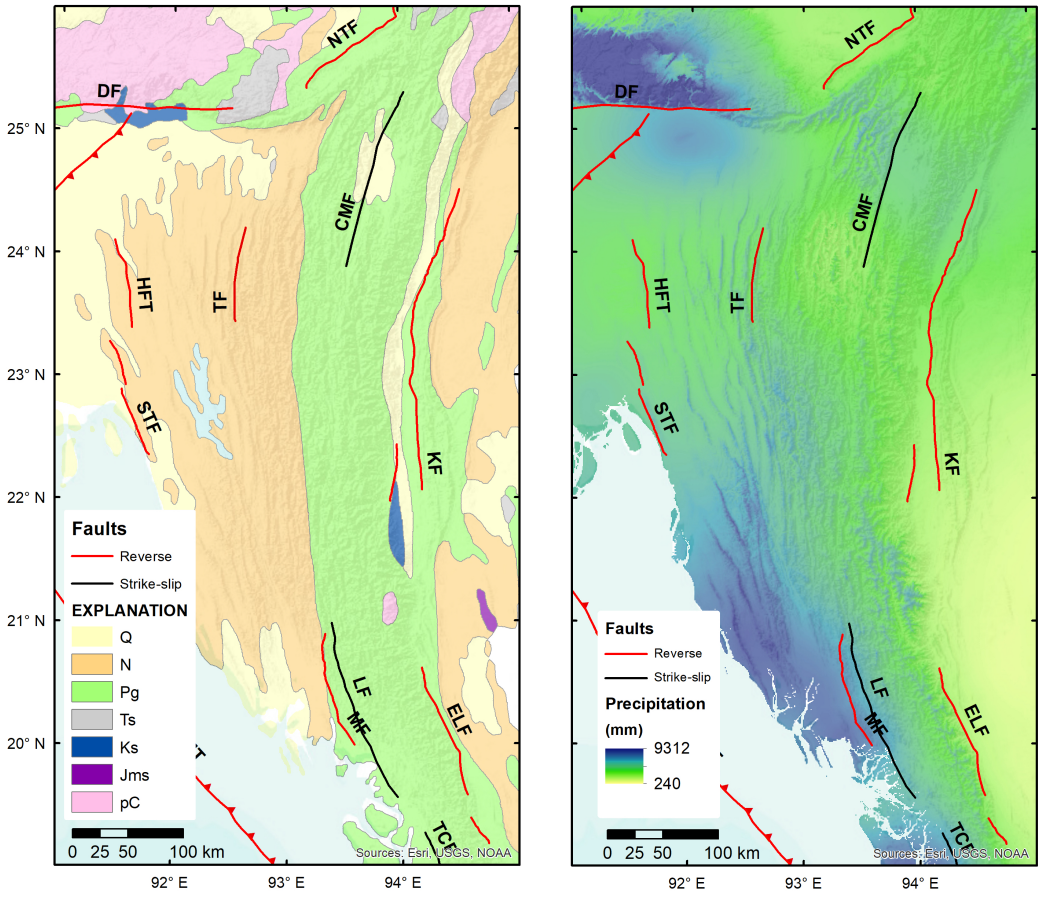

Figure 3.3: Geologic and annual precipitation rate maps. (a) The geologic map is from the Bureau of Indian Education, Department of the Interior. Most of the IBR is underlain by accreted Neogene and Paleogene molasse and flysch sediments. (b) Precipitation rates in mm/yr are from WorldClim bio-climatic variable data base. The faults on both maps are from Wang et al. (2014) and Betka et al. (2018); NTF = Naga Thrust Fault, LF = Laymyo Fault, MF = Minbya Fault, ELF = East-Limb Fault, TCF = Thahtay Chuang Fault, TF = Tut Fault.

the geoid in EGM96 vs. ellipsoidal heights in WGS-84), the SRTM DEM elevations are about 50 meters higher than those from TANDEM-X but are otherwise very similar (RMS = 6 m after removal of constant shift). For the normalized steepness index (k_{sn}, see below), both DEMs suggest high k_{sn} at consistent locations along the streams (Figure 3.4) and the range of k_{sn} values is similar. Therefore, we conclude that the 30 × 30m DEM is suitable for our geomorphic index calculations. As we do not have access to TanDEM-X data for the entire study region, we rely on the 30 × 30m SRTM DEM in our study. Next, we extract streams and watersheds and calculate geomorphic indices. We (1) explore drainage divide stability and (2) infer patterns of tectonic uplift applying both basin- and stream-scaled morphometric indices.

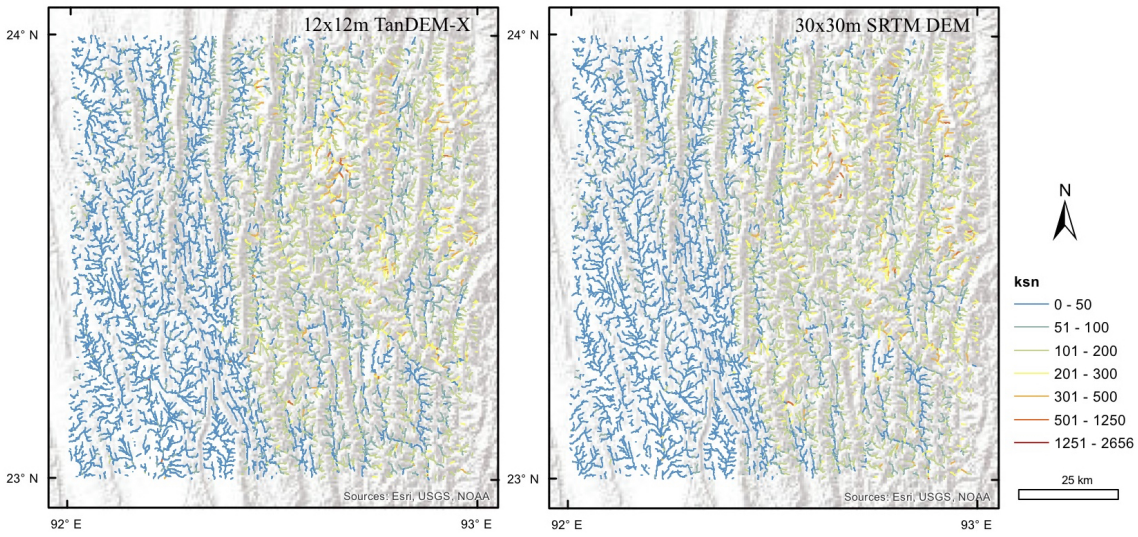

Figure 3.4: Comparison between k_{sn} values extracted and calculated from 12 × 12m TanDEM-X and 30 × 30m SRTM DEMs. Both DEMs provide similar values and spatial distribution of k_{sn}. This indicates that using the 30 × 30m SRTM DEM to calculate geomorphic indices will not cause significant biases.

Drainage Divide Stability Assessment

The mobility of drainage divides provides useful information about ongoing drainage system evolution. If the divides and stream networks are in equilibrium, the morphometric investigation of stream channels and basins can indicate spatial variations in tectonic uplift, erosion efficacy and/or lithology (Forte and Whipple, 2018). Thus, before assessing the spatial patterns of morphometric indices and inferred tectonic uplift, we first investigate the divide mobility of drainage divides within the IBR. For this purpose, we use χ and the Gilbert's metrics (Forte and Whipple, 2018).

χ is a widely used morphometric index describing the topology of a drainage system (Harkins et al., 2007; Perron and Royden, 2013; Mudd et al., 2014). Some studies also use this indicator as a proxy for equilibrium/disequilibrium states of drainages and it can provide evidence of potential drainage divide migration in a region where uplift rates, erosional efficiency, climate, and precipitation rates are uniform (Whipple et al., 2017; Willett et al., 2014). By comparing χ values of two streams on opposite sides of a drainage divide, if the χ value on one side of the divide is greater than on the other, this divide is likely unstable and propagates towards the side with the higher value. To compare χ across the study region, we set a scaling drainage area (A_0) to $10^6 m^2$, reference concavity index (θ_{ref}) to 0.45, which is a mean value of the typical concavity range used for k_{sn} calculation (Kirby and Whipple, 2012; K. Whipple et al., 2017), and base level elevation of 60 m above sea level (equation 1 in Table 3.1). Differences in base level elevation can affect the calculated χ values (Forte and Whipple, 2018). We choose 60 m because it is the minimum elevation of the major outlets on both sides (east and west) of the IBR. Following this procedure, we obtain the χ map shown in Figure 3.5a, which will be used for further analysis of individual divide segments.

In addition, Forte and Whipple (2018) propose methods based on Gilbert (1877)'s finding of unequal declivities, which invokes that differences in topography on two sides of a divide, i.e., mean channel elevations, channel relief, and gradients, can indicate contrasts in erosion rates, suggesting divide instability. The authors state that even though χ maps are widely used for examining divide stability because of their easy calculation and provide visual assessment over a large area, χ maps work best in regions with consistent climate, rock erodibility and uplift. Since these factors are not uniform across the whole IBR region, we include the channel elevation, relief and gradient maps to identify the locations of anomalies, where we observe differences of these values on the two sides of divides. These three morphometric indices (channel elevation, relief and gradient) are named the Gilbert metrics by Forte and Whipple (2018). To calculate the Gilbert metric maps, we employ the TopoToolbox and DivideTools. The channel elevation values of the streams are directly derived from the DEM, and then we normalize these values into the range of 0 – 1. For the channel relief calculation, we first compute the local reliefs for all grids in the DEM using a moving window filter radius of 500 m. In other words, the elevation range within this radius is used to find the local relief of an individual grid point. Then, we again normalize the relief values of all grid points to put the values into the range of 0 – 1. Finally, we select the mean values of each cell along the streams extracted from the DEM. In addition, for the gradient calculation we estimate gradient values of the individual cells and normalize the gradients of all cells in the entire DEM. Then, we only choose the mean gradient values of each cell along the streams. After obtaining all three metrics of the streams in the IBR (Figure 3.5), we extract these values and χ on both sides of selected divide segments, as explained below.

We focus on three major drainage divides, which are (A1) the EW drainage divide where the tributaries of the Barak, Kaladan and Karnaphuli originate, (A2) the NS divide including the tributaries of the Manipur, Barak and Kaladan Rivers, and (A3) the easternmost NS divide (Figure 3.6a). This selection is based on the χ map where we observe χ anomalies (high contrasts between the streams on the two sides of the divides, Figures 3.5a and 3.6b-

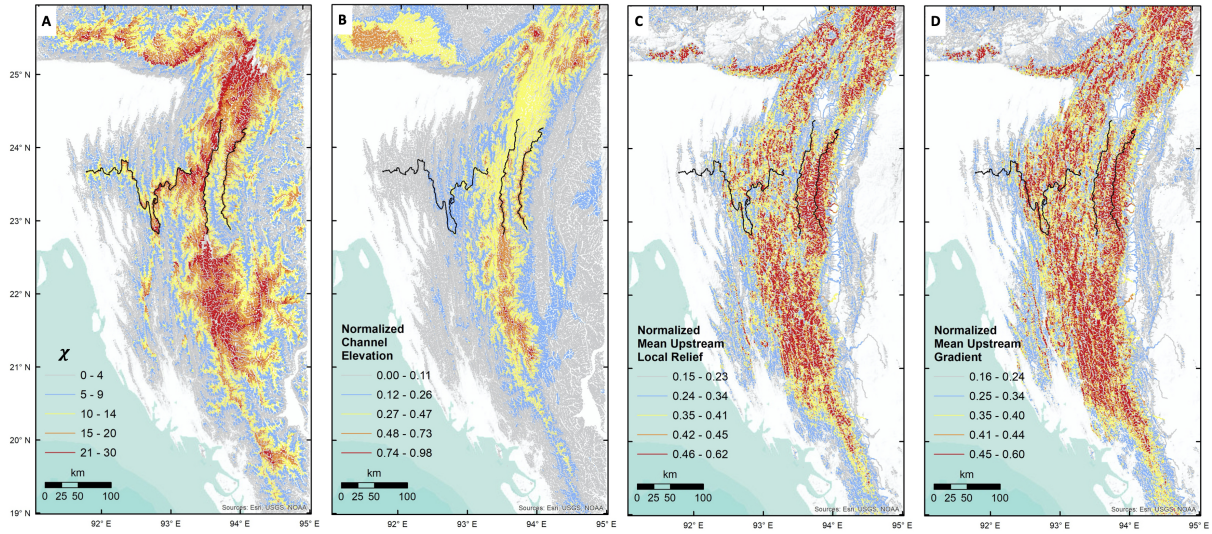

Figure 3.5: Results of divide stability study (χ and the Gilbert metrics). (a) χ map for streams using a base level elevation of 60 m in the IBR. Warmer colors represent a higher drainage area at a certain distance from the headwater. Where the regions on the two sides of divides have highly contrasted χ values this suggests instability and progressive migration of the divides towards the side of higher χ. (b – d) the Gilbert metric maps (normalized channel elevation, normalized mean upstream local relief and normalized mean upstream gradient, respectively). Where the values of the metrics at the stream endpoints (reference drainage area = $10^6 m^2$) on the two sides of divides have significantly different values, instability, and progressive migration of the divides towards the side of high χ, high channel elevation, low channel relief, and low stream gradient, may be indicated. The black lines are the major drainage divides used in the divide stability assessment.

c). To examine whether the χ anomalies that we observe in these three regions provide a reliable interpretation on the divide stability, we also apply the Gilbert metrics (Forte and Whipple, 2018) to our analysis. In order to assess if a drainage divide is stable, we select multiple segments along the divides to calculate the Gilbert metrics and χ. Then, we generate histograms of these four indices calculated at the channel heads on both sides of the divide segments. Next, we find the degree of difference or overlap of the estimated index values across these divides of interest (Figure 3.7). There are four options to indicate the amount of overlap of the indices, which are their standard deviation, standard error, bootstrapping (using 95% confidence interval from a normal bootstrap statistics), and the paired t-test. Forte and Whipple (2018) indicate that the use of the standard deviation may provide a bias toward a finding suggesting a stable divide (high possibility of overlapping), the standard error may produce a bias toward unstable divide (low possibility of overlapping), and the paired t-test works best when the values or populations are normally distributed, which is

not always the case in this study area. Therefore, we decide to use bootstrapping to estimate the degree of similarity of the metrics of the channel heads on the two sides of the divides and to interpret their stability. Accordingly, the estimated Gilbert metrics and χ of the channel heads located on the two sides of a studied divide segment suggest a progressive migration of that divide section towards the side of high χ, high elevation, low channel relief and low stream gradient.

Tectonic Uplift Investigation

After having considered and explored a number of indices, i.e., normalized steepness index, valley-floor-width-height ratio, basin elongation ratio, hypsometric integral, drainage density, etc., which have been proposed as diagnostic measures of tectonic uplift (e.g., Kirby and Whipple, 2012, 2001; Pérez Peña, 2009; Pérez-Peña et al., 2010; Wobus et al., 2006; Snyder et al., 2003; Keller and Pinter, 1996), we focus on three indices, including both basin- and stream-scale measures. These indicators have been found to be particularly responsive to surface deformation due to active tectonics and are relatively easy to calculate when investigating large study regions (e.g., Keller and Pinter, 2002; Kirby and Whipple, 2001; Wobus et al., 2006; Willett et al., 2014; Whipple et al., 2017; Forte and Whipple, 2018).

For the regional investigation, we examined basin-scale geomorphic indices (hypsometry and relief), and stream-scale morphometric indicator (steepness index [k_s] or normalized steepness index [k_{sn}], Table 3.1), because these indicators have been found to be particularly responsive to surface deformation due to active tectonics and easy to use when investigating large study regions (e.g., Keller and Pinter, 2002; Kirby and Whipple, 2001; Wobus et al., 2006; Willett et al., 2014; Whipple et al., 2017).

The basin-scale indicators used in this study are hypsometry and relief. Hypsometry documents the relative distribution of elevations within a study area (Pérez-Peña et al., 2010). It can be described and quantified using hypsometric curves (HC) and the hypsometric integral (HI). The HCs are used to illustrate the dominance of either low or high elevations within a basin, which has been argued to quantify the erosion stage of that basin. If there is a predominance of low elevations within a basin, this may suggest an "old" stage condition where erosion dominates over tectonic uplift, and vice versa. However, this measure also depends on the distribution of active structures in a study region. If a study region is similar to the widely spaced western anticlines in the IBR, there will likely be a dominance of low elevation areas within individual basins. The HI represents the area under the HC (area-slope curves), such that low HI values (below 0.3) represent concave HCs indicating dominance of low-elevation areas within a watershed (i.e., Singh et al., 2008). Higher HIs suggest more S-shaped or convex HCs. In our initial analysis of individual watersheds, we found that most watersheds with higher HIs have S-shaped HCs, while those with lower HIs have concave HCs (Figure 3.8), consistent with other published papers (i.e., Singh et al., 2008). Accordingly, to estimate HIs, we divide the study area into 5 $\times$ 5km pixels and calculate their HIs. We use the Hot Spot Analysis Tool in ArcGIS to calculate the Getis-Ord Gi* statistic and determine in which areas low or high HIs are spatially clustered. Another basin-scale indicator is relief,

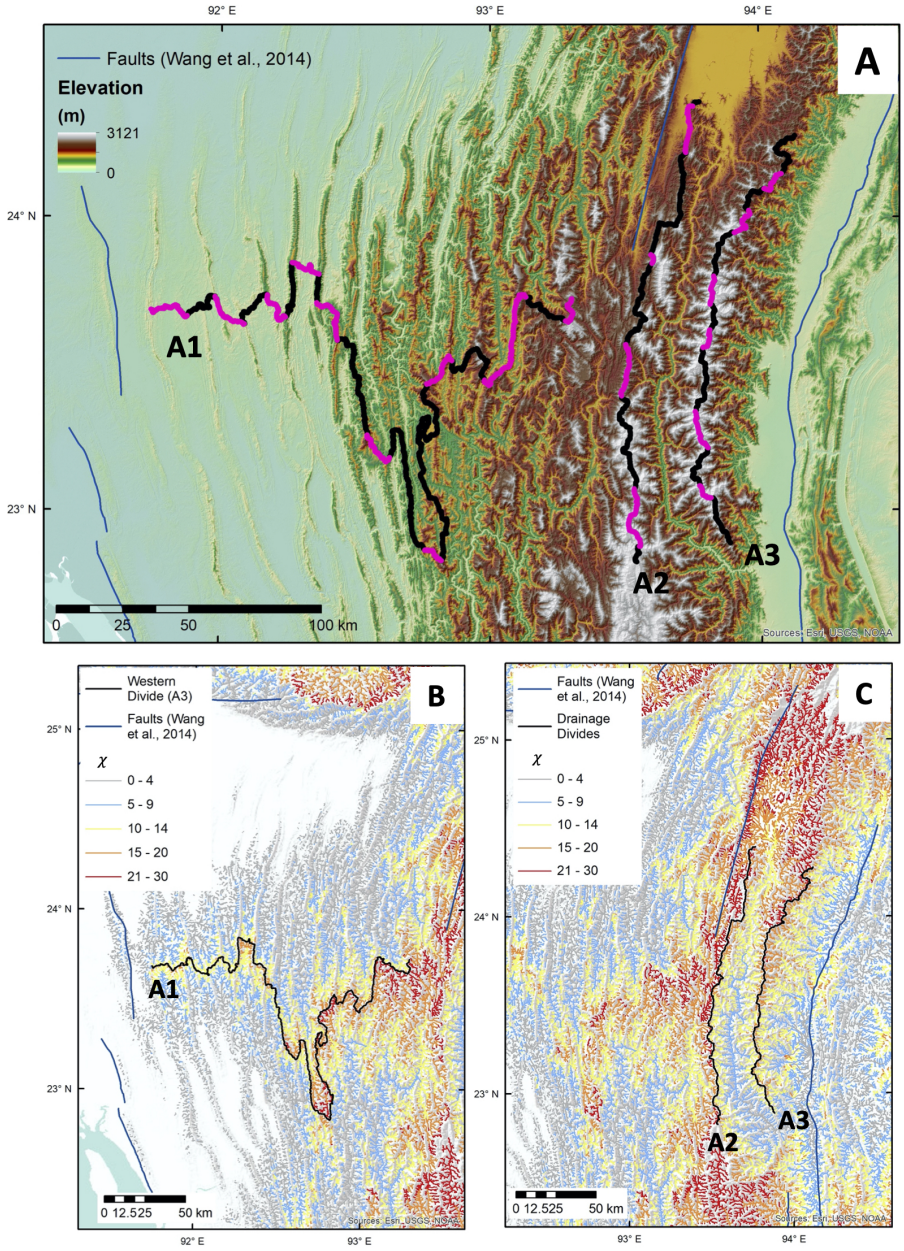

Figure 3.6: Three sub-regions and drainage divides in the northern IBR (a). The pink segments of the individual divides (black lines) are the selected portions used to calculate the Gilbert metrics and χ. (b, c) Close-ups of χ maps of the three major drainage divides A1, A2, A3 described in Methods - Drainage Divide Stability Assessment. The χ maps of the divides in A1, A2, and A3 show strong contrasts between the χ values of the channel heads on the two sides of the divides.

Morphometric Indicators	**Equation**	**What it can indicate**	**References**
Divide Stability			
1. Chi (χ)	$\chi = \int_{x_b}^{x} (\frac{A_0}{A(x)})^{\theta_{ref}} dx$ where x = upstream location, x_b = base level or outlet location, A_0 = scaling drainage area, $A(x)$ = drainage area at location x, θ_{ref} = reference concavity index	Stability of drainage divides of interest.	Harkins et al. (2007), Perron et al. (2013), Mudd et al. (2014), Willett et al., (2014), Y. Wang et al. (2017), Whipple et al. (2017), Forte and Whipple (2018)
2.- 4. Channel Elevation, Relief, Gradient (Gilbert's Metrics)	N/A (see Methods - Drainage Divide Stability Assessment)	Correlate with erosion rates. Contrasts in these indicator values on two sides of a divide can indicate variation in erosion rates across that drainage divide, and thus, suggest divide migration.	Forte and Whipple (2018), Roering et al. (2007), Roering et al. (1999)
Basin-Scale Indices			
5. Hypsometric Integral (HI) and Curve (HC)	N/A (see Methods - Tectonic Uplift Investigation)	Distribution of elevation within a basin. There are 3 main types of HC: (1) convex HC suggesting dominance of high elevation area within a basin. (2) S-shaped HC indicating equilibrium between high and low elevation areas within a basin. (3) concave HC suggesting dominance of low elevation area within a basin.	Strahler (1957), Pérez-Peña et al. (2009), Azañón et al. (2012), Bellin et al. (2014)
6. Relief	$Relief = Elevation_{max} - Elevation_{min}$	Ongoing tectonic deformation and distribution of rainfall.	Bookhagen and Strecker (2008), Gaidzik and Ramırez-Herrera (2017)
Stream-Scale Index			
7. Steepness Index and Normalized Steepness Index (k_s and k_sn)	$S = k_s A^{-\theta}$where S = local channel slope, A = upstream drainage area, θ = concavity index $k_{sn} = k_s(A_{cent})^{\theta_{ref}-\theta}$ where A_{cent} = drainage area at the midpoint of the analyzed stream, θ_{ref} = regional mean concavity index	Sensitive to erodibility, uplift and precipitation rates.	Hack (1957), Flint (1974), Howard and Kerby (1983), Snyder et al. (2000), Brocklehurst and Whipple (2002), Wobus et al. (2006), Cyr et al. (2010), Wang et al. (2017)

Table 3.1: Geomorphic indices used in the investigation of divide stability and tectonic uplift (see Methods). Note that the indices 1 – 4 are calculated by using the TopoToolbox and DivideTools.

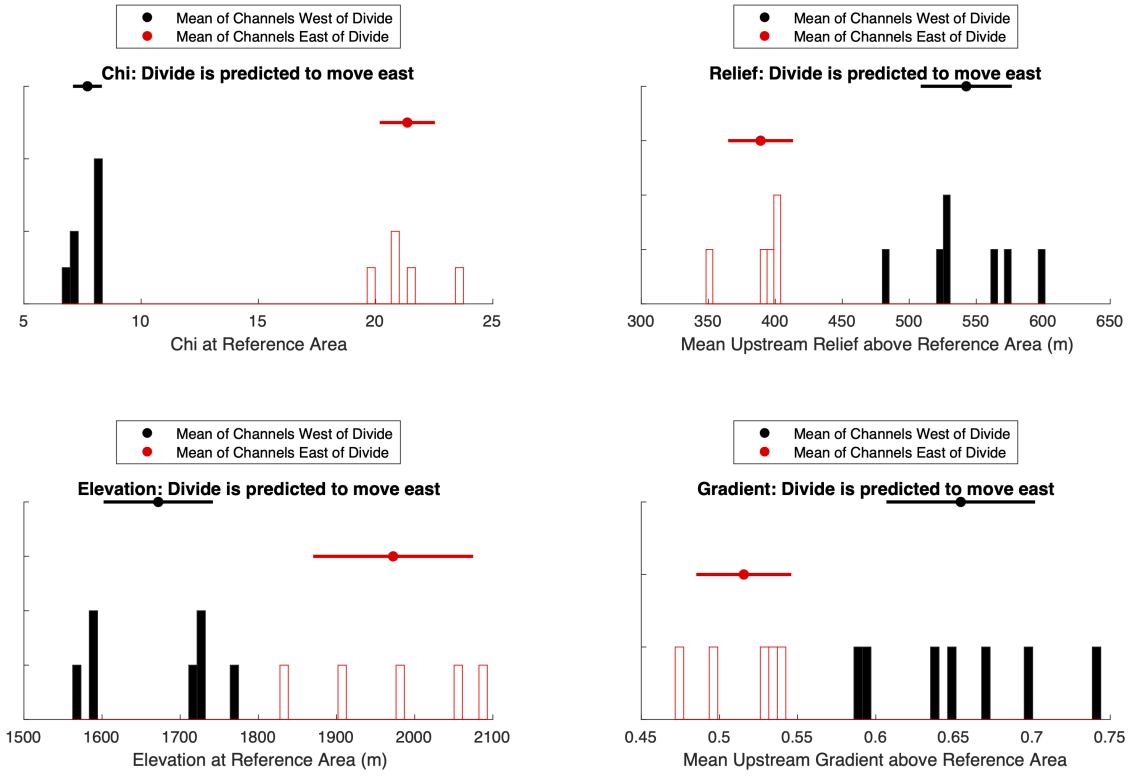

Figure 3.7: An example of the estimated metrics of channel heads on both sides of the A3 divide segment EDIV4 plotted in a histogram format. The amount of overlapping between the two sets of histograms are used to identify the divide stability.

the difference between the maximum and minimum elevations within a selected area. High relief can indicate rapid tectonic deformation (i.e., Gaidzik and Ramırez-Herrera, 2017) or high rainfall (i.e., Bookhagen and Strecker, 2008). For the calculation, we use the same 5 $\times$ 5km grid to calculate the local relief of individual pixels.

Moreover, several stream-scale indicators have been argued to reflect underlying uplift rates (D'Arcy et al., 2014; Pérez-Peña et al., 2010; Wobus et al., 2006). The stream-scale index we use to examine this region is k_{sn}, which is positively correlated with k_s. Following the stream power erosion law, the k_s is strongly correlated with the stream channel concavity (θ). From Table 3.1, as we transform the equation of k_s into log-log space, the concavity index represents the slope and k_s is the y-intercept of the log-log slope-area plot (e.g., Wobus et al., 2006). Therefore, when we plot channel slopes and drainage areas of several points along a stream in a logarithmic space and apply linear regression, we can determine a best fit concavity index and k_s value of that stream. To obtain k_{sn} and be able to compare the values of several streams in a study region, we use θ_{ref}, a reference concavity index, which is usually in a range of 0.4 – 0.5 (i.e., Kirby and Whipple, 2012; Whipple, 2017). The k_{sn}

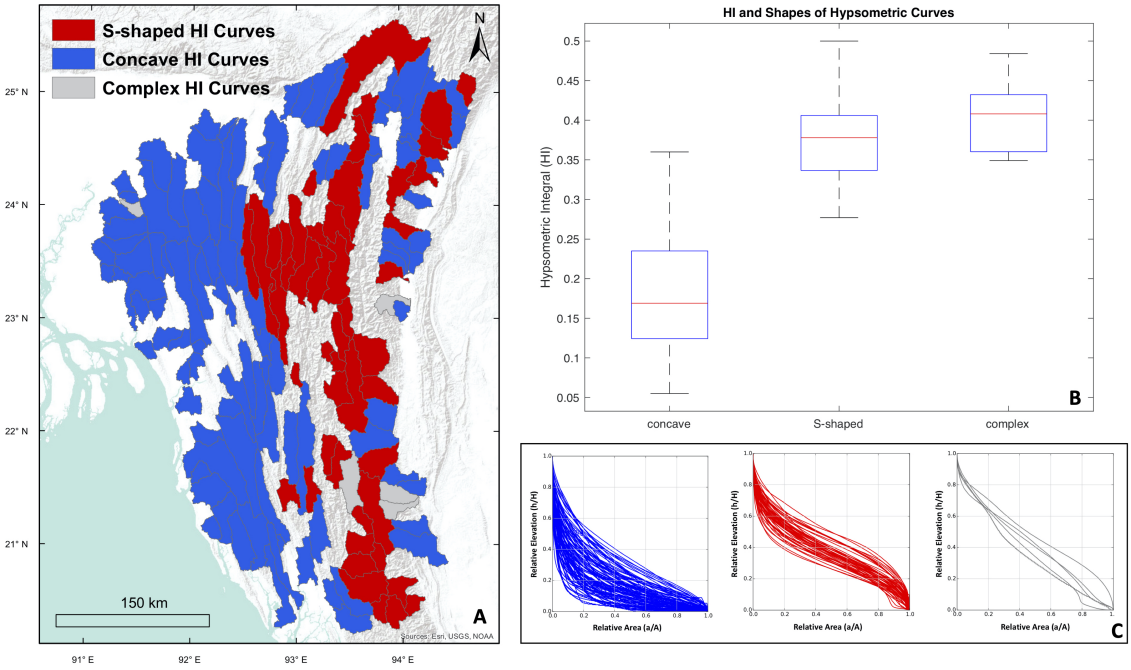

Figure 3.8: Relationship of HIs and HCs. (a) HCs of individual watersheds. (b) Box plots show the relationship between HIs and HCs. Most of the basins with higher HIs have S-shaped HCs while watersheds with lower HIs have concave HCs. According to this relationship, we rely on HIs for further study for greater coverage. (c) Three types of 4th-order-stream watershed HCs found in the IBR.

has been suggested to have a positive non-linear correlation with tectonic uplift rates but has also been shown to be sensitive to varying precipitation rates and lithologic properties (Kirby and Whipple, 2001, 2012; Wobus et al., 2006).

Importantly, there are a number of factors in addition to active uplift, in particular lithology differences and variations in precipitation, that can affect such morphometric analyses as they can produce similar patterns in the morphometric expression (e.g., Kirby and Whipple, 2012 and references cited there). Thus, we investigate possible regional-scale lithology effects on our geomorphic indices by using the geologic map from the Bureau of Indian Education, Department of the Interior, and precipitation variations by utilizing the database from WorldClim (Figure 3.3). To study the correlation between precipitation rate/lithology and k_{sn}, we (1) overlay our geomorphic results on lithology and precipitation maps and examine their correlations, and (2) extract k_{sn}, precipitation rate and lithology of individual points along the stream channels and create scatter and kernel density estimate (KDE) plots.

3.4 Results

As described in the Methods section, we consider geomorphic measures for divide stability assessment and tectonic uplift investigation. We first describe our results regarding divide stability. If the divide locations are static, this allows us to further examine the uplift patterns in this region using morphometric indices. Next, we present the basin- and stream-scale geomorphic indicators as proxies for spatially variable tectonic uplift rates across the IBR, while also considering the variations in precipitation and lithology.

Divide Stability Assessment

According to the χ maps from the previous section (Figure 3.6b-c), almost all segments along the drainage divides A1, A2 and A3 seem to be unstable, that is, they exhibit high contrasts of χ values of the channel heads across the divide. However, when we study individual segments of each divide by also considering the Gilbert metrics, we find that for the A1 divide, the results often contradict the χ solutions. The χ values indicate three segments (WDIV2, 8, 10) along the A1 divide are in equilibrium state (Figure 3.9), with two (WDIV4, 5) appearing to migrate northeastward and all others to the south. However, the Gilbert metrics suggest that only the WDIV2 segment is unstable and likely migrates southeastward. Accordingly, it is likely that the only segment that is unstable along the A1 divide is WDIV2, which is close to the A2 divide and located near the contact between the Neogene and Paleogene sedimentary rocks (Figure 3.10). Accordingly, most segments of the A1 divide are likely to be in equilibrium.

On the other hand, for A2, the Gilbert metrics and χ suggest unstable northern segments and more stable southern divisions (Figure 3.11a-b). The χ values suggest all four segments in this sub-region are unstable. However, the Gilbert metrics indicate that the MDIV1 – 2 are stable. On the other hand, for the third section, MDIV3, the Gilbert metrics and χ indicate that this is an unstable section, but they suggest different directions of inferred divide migration. All three Gilbert metrics indicate that the migration is in the east direction, while only χ suggests westward migration. For MDIV4, χ and elevation metrics indicate that this segment is unstable and migrates eastward while the mean upstream relief and gradient metrics suggest a stable divide. Overall, the A2 divide seems to be unstable in the northern part and stable in the south (Figure 3.11a-b).

Similarly, we find that for the A3 divide, the EDIV1 – 3 segments appear to be stable, while the EDIV4 section is unstable and EDIV5 – 6 division stability status are undefined. The χ values alone indicate that all six segments of the A3 divide are unstable (Figure 3.11c). However, there is only one segment, EDIV4, for which the three Gilbert metrics agree with the χ result, and the divide tends to migrate eastward (Figure 3.11d). For the other two segments EDIV5 and 6, χ and elevation metrics suggest that these portions of the divide are not stable. However, both metrics indicate different migration directions. Thus, the stability status and migration direction of these divide segments are undefined. Overall, for the A3,

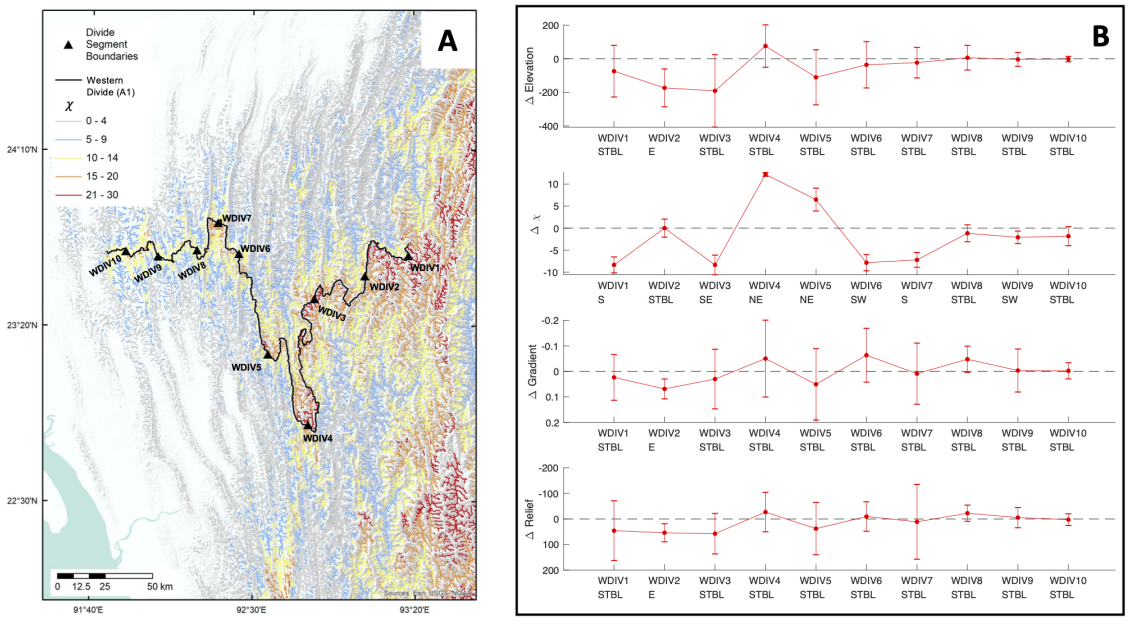

Figure 3.9: Results of the A1 divide stability study. (a) χ map and location of A1 sub-region. The black line indicates the EW drainage divide, while the black triangles represent the midpoints of the selected study segments (pink lines in Figure 3.5a) along the divide. (b) The Gilbert metrics' and χ results indicate the stability status and potential divide migration direction on the x-axes. The gray dashed lines represent divide stability lines. If an error bar determined by bootstrapping for a divide segment includes the stability line of a given metric (e.g., $\triangle$ elevation), that metric suggests that the segment of the divide is stable, and vice versa. Note that the y-axes of $\triangle$ gradient and $\triangle$ relief are reversed. The values significantly above the divide stability lines indicate possible divide migration toward the north/northeast. On the other hand, the values significantly below the divide stability lines suggest possible migration toward the south/southwest. The format of the plots in (b) is based on Forte and Whipple (2018).

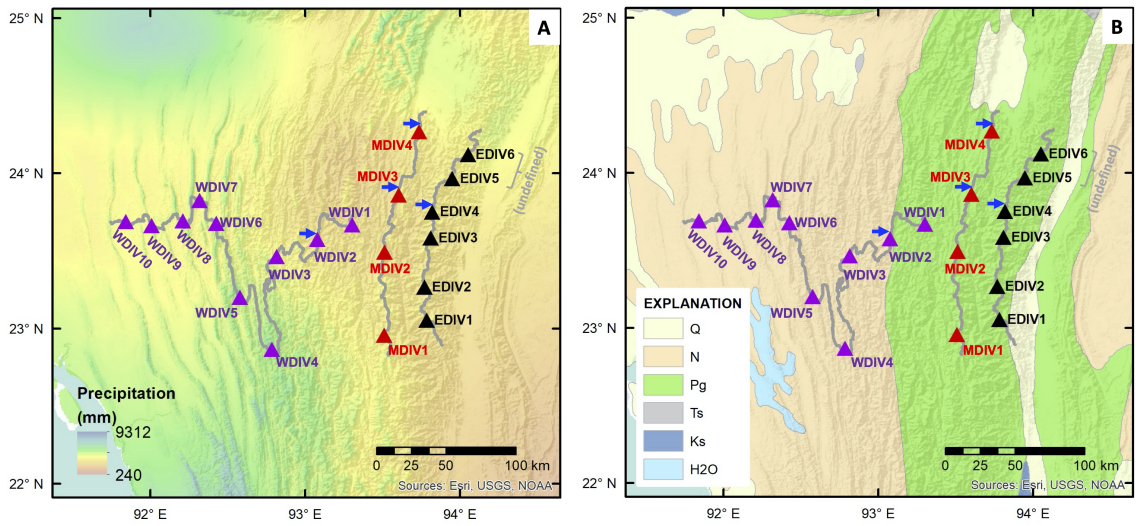

Figure 3.10: Annual precipitation rate, geologic map units and locations where the divide stability was studied. (a) Annual precipitation rate map. The warmer color represents lower rates of annual precipitation. (b) Geologic map; Q = Quaternary sediments, N = Neogene sedimentary rocks, Pg = Paleogene sedimentary rocks, Ts = Tertiary sedimentary rocks, and Ks = Cretaceous sedimentary rocks. The triangles represent the midpoints of the selected study segments (pink lines in Figure 3.5a) along the divides. The EDIV4, MDIV3 – 4 and WDIV2 are the inferred unstable portions of the divides. The divide migration directions are indicated by blue arrows in both (a, b). The stability status and migration directions of EDIV5 – 6 are undefined due to the contrasting results of the Gilbert metrics and χ. Overall, locations of unstable divides do not seem to correlate with the precipitation and geologic variation. However, the WDIV2 segment is located near the contact between the Neogene and Paleogene sedimentary rocks. Thus, it's possible that the lithologic difference might affect its divide stability.

the central division appears to be unstable while the southern portions are stable, and the northern are undefined.

Tectonic Uplift Investigation

Our large-scale morphometric analysis of the IBR suggests a more complex and potentially more active zone in the inner belt, which is bounded by the TF and KF in the north and LF and ELF in the south, than in the western outer belt. In the west, the topography is dominated by spaced, low-elevation anticlines accommodating modest amounts of EW contraction (Betka et al., 2018). This is also reflected in the distribution of elevation, relief, and HI (Figure 3.1 and 3.12). This contrasts with the relatively high elevations and local

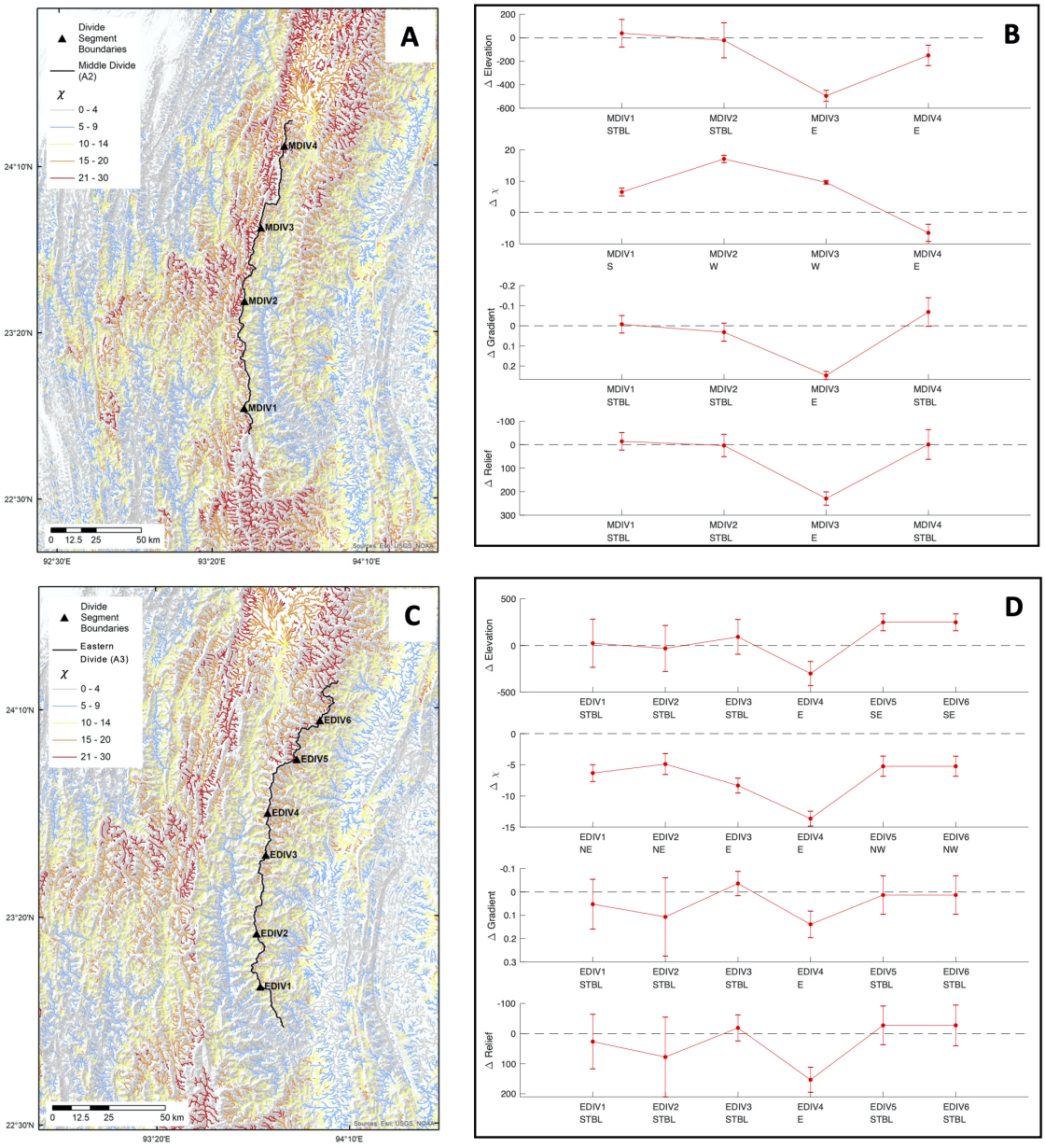

Figure 3.11: Results of the A2 and A3 divide stability studies. (a, c) The drainage divides in the study locations A2 and A3, respectively. The black triangles represent the midpoints of the selected study segments (pink lines in Figure 3.5a) along the divides. (b, d) The Gilbert metrics' and χ results indicate the stability status and potential divide migration direction on the x-axes. The gray dashed lines represent divide stability lines. Note that the y-axes of $\triangle$ gradient and $\triangle$ relief are reversed. Thus, the values significantly above the divide stability lines indicate possible divide migration toward the west, and vice versa.

relief in the eastern and central IBR. Similarly, the areas in the east (between the CMF and KF in the north and between the LF and ELF in the south) have higher HI values (Figure 3.12b).

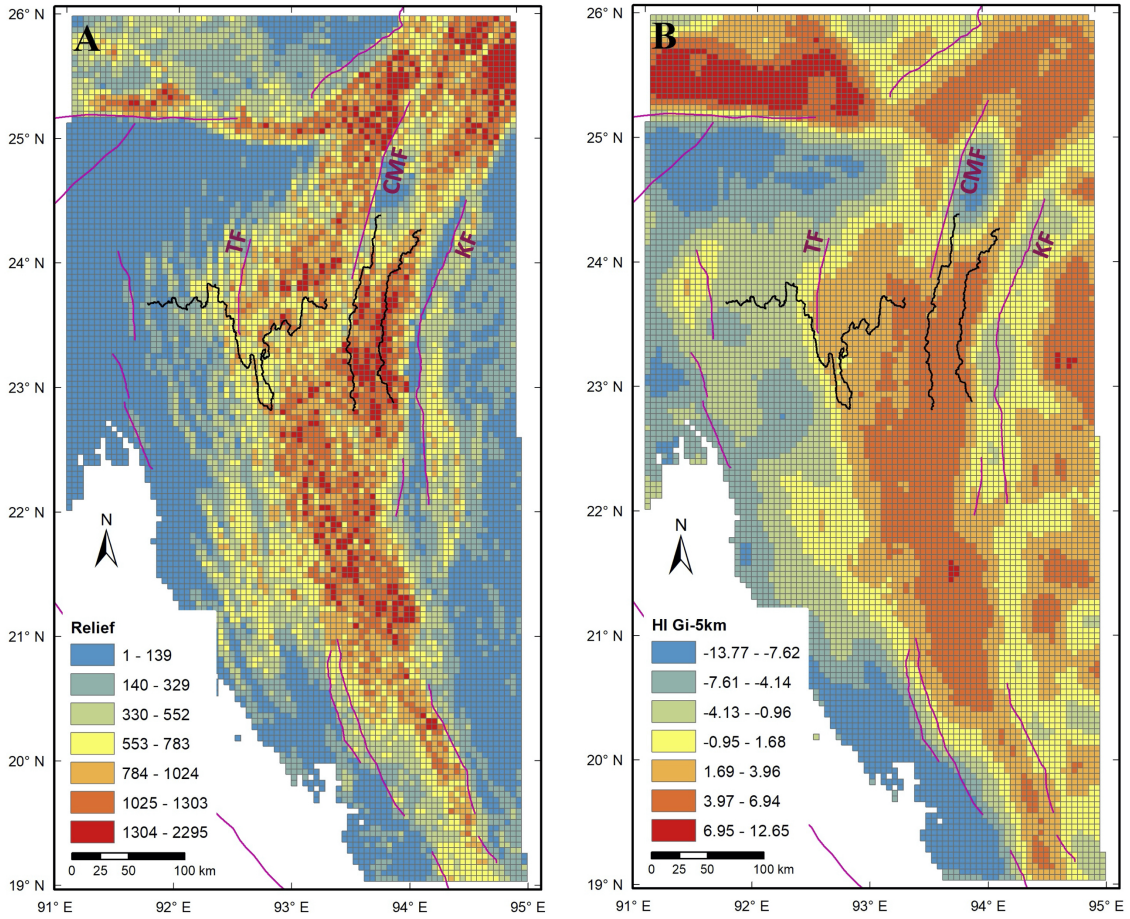

Figure 3.12: Basin-scale morphometric results. (a) Relief map of 5 × 5km pixel dimensions for the entire study region. The warmer colors represent higher relief. (b) Weighted HI map relying on the Getis-Ord Gi* statistic approach (HI Gi). The warmer colors represent higher HIs (greater variation in elevation within an individual pixel) and vice versa. The areas with higher relief generally have greater HI Gi values. The pink lines are faults (Wang et al., 2014; Betka et al., 2018), and the black lines are drainage divides described in section Methods - Tectonic Uplift Investigation.

The stream-scale indicator may illuminate actively deforming areas in more detail. There are two major clusters of high k_{sn} values which are (1) around the Manipur River (latitude 22.5° – 24° and longitude 93.5° - 94°, or easternmost of the IBR) and (2) in the eastern region of the Kaladan River and northern part of the Man River (∼ latitude 21° - 23° and

longitude 93° - 94°, Figure 3.13). Moreover, between the southern CMF and the Tut fault (TF), which has been proposed by Betka et al. (2018) as an out-of-sequence reverse fault along the boundary between the inner and outer belt, the k_{sn} values are relatively high. Also, the TF is close to the transition from relatively high k_{sn} (yellow and blue on Figure 3.13b) to low values (gray).

Overall, we consistently observe that there are areas of higher areal relief, HI Gi-5km and k_{sn} in the eastern IBR (Figure 3.12 and 3.13). In addition, by overlaying the k_{sn} values of the streams on the precipitation and lithology maps, the distribution of the geomorphic indices seems to be somewhat correlated with the distribution of precipitation rates but does not appear to be related to the lithologic domains (Figure 3.14). We will discuss the correlation with precipitation and lithology in more detail later in the discussion, where we extract all three values (precipitation rates, lithology and k_{sn}) for individual points along the streams and create plots, i.e. scatter and KDE plots, to quantitatively evaluate their relationships.

3.5 Discussion

Divide Stability

The regional-scale geomorphology illustrates that most uplifts/anticlines are oriented in the NS direction, but the χ map indicates that the primary drainage divides in the IBR are oriented both EW (A1) and NS (A2, A3, Figure 3.6). The EW divide is located across the western thrust-and-fold belts where the elevation is relatively low. Most of the segments of this divide are suggested by the Gilbert metrics and χ to be in equilibrium. The only portion that is likely unstable, potentially migrating northeastward (WDIV2 in Figure 3.9), is a segment that is oriented nearly NS and located near the contact of the Neogene and Paleogene sedimentary rocks (Figure 3.10). This might be due to the differences in rock strength or lithology affecting the divide migration around that segment. In contrast, the precipitation rate around this area is fairly uniform suggesting little effect of precipitation on the instability of this divide segment (WDIV2).

On the other hand, the NS-oriented divides in the east (A2 and A3), particularly the northern segments of A2 and the middle portion of A3, appear to be unstable, based on the differences in χ values and Gilbert metrics on either side of the divides. This indicates contrasting erosion rates across these parts of both divides and is reflected in the potential migration directions of these divides toward east. We do not observe a clear correlation between these unstable segments of the divides with substantial gradients in precipitation or contrasting lithologic units (Figure 3.14 and 3.15). It is possible that drainage reorganization due to stream capture by the Manipur River is taking place in the northeastern IBR.

In general, the climate and lithology are often important factors governing the surface processes and influencing the drainage systems. Thus, we evaluate the possible correlations between variations of divide stability and precipitation/lithology in our study region (Figure 3.10). We do not observe a clear effect of these factors on the divide stability results. Overall,

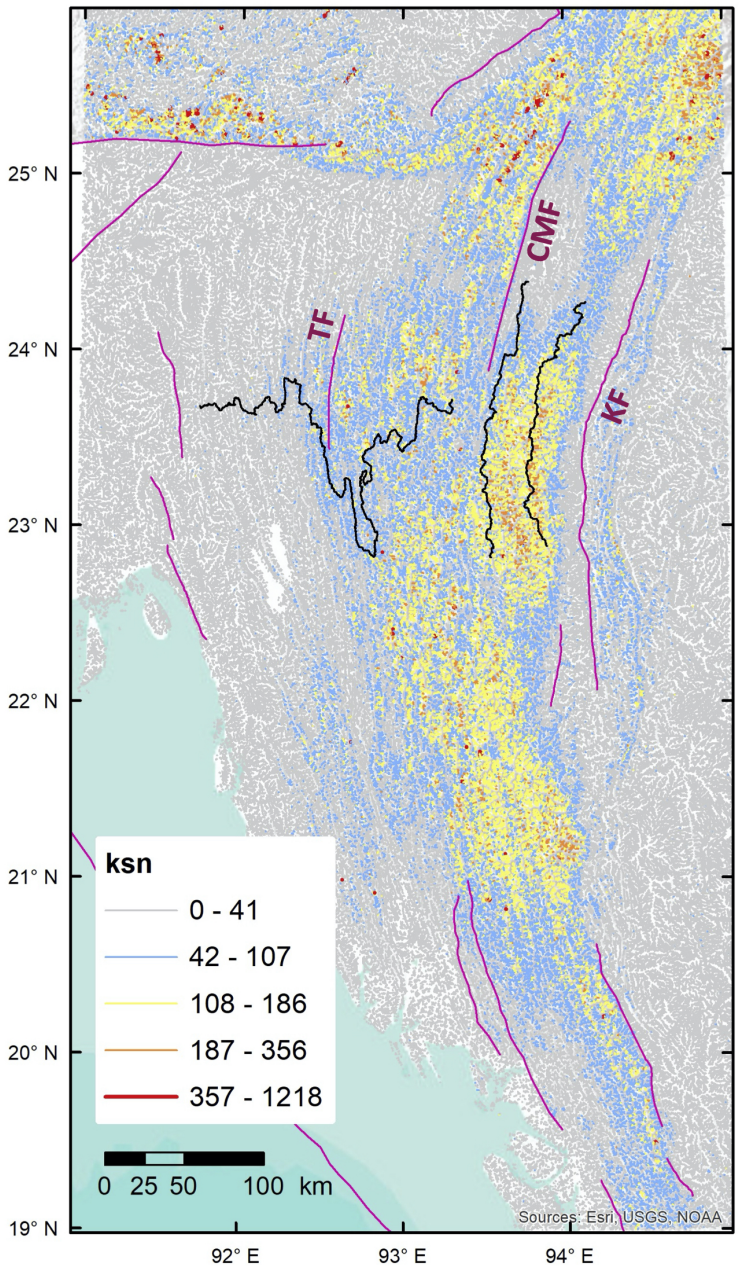

Figure 3.13: Spatial distribution of stream-scale normalized steepness index (k_{sn}). The warmer colors represent a higher normalized steepness index, suggesting more rapid uplift. The pink lines are faults (Wang et al., 2014; Betka et al., 2018), and the black lines are studied drainage divides described in Methods - Tectonic Uplift Investigation.

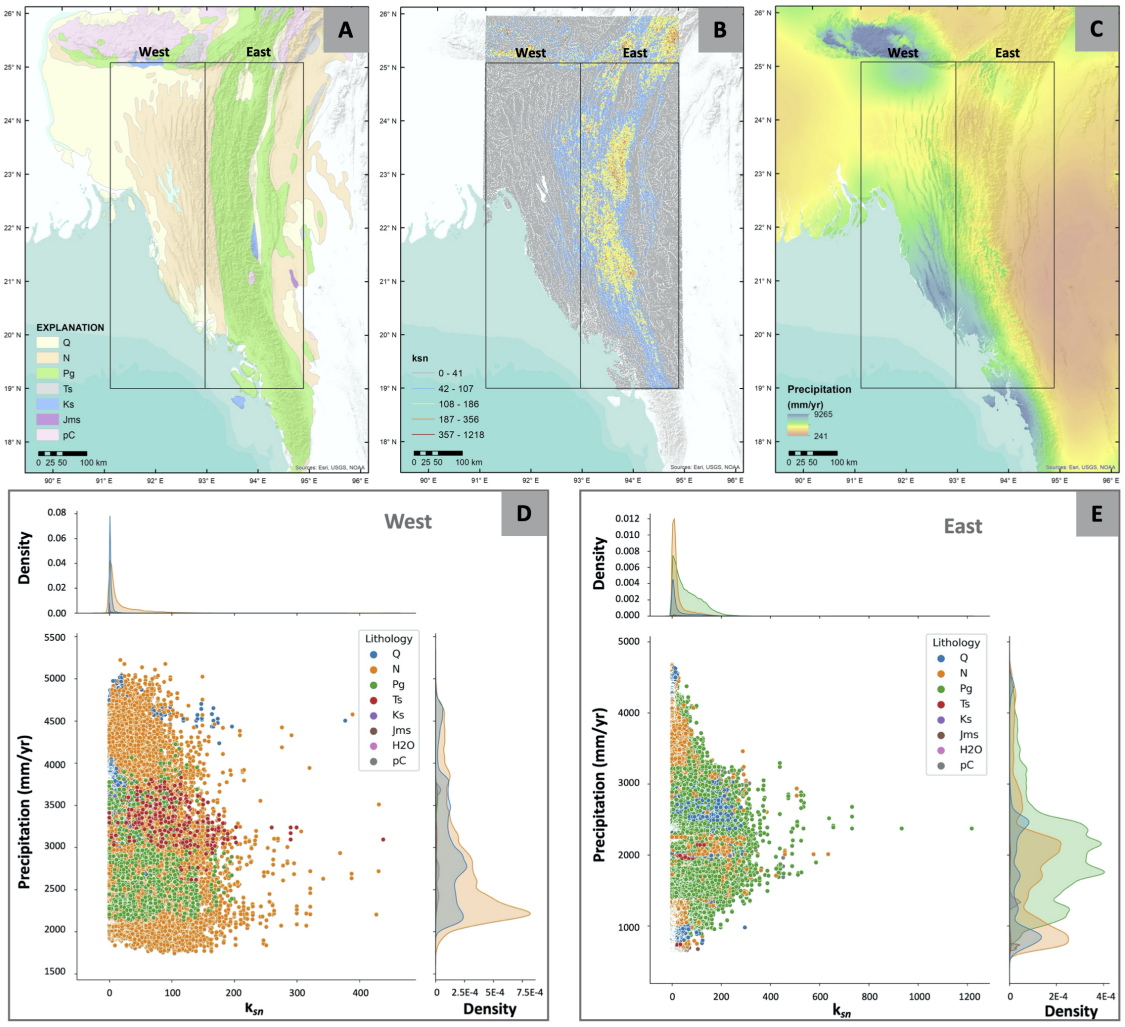

Figure 3.14: Scatter and KDE plots showing the correlation between precipitation/geology and k_{sn} values. (a, b, c) The map showing western and eastern blocks where we extracted the geologic map units, k_{sn} values, and precipitation rates from the streams, respectively. (d, e) The scatter plots of annual precipitation rates and k_{sn} values, and the KDE plots of the precipitation rates and k_{sn} values of individual lithology types indicated by different colors in the plots. The values in these plots are extracted from the streams in the western and eastern portions, respectively. The geologic unit abbreviations on the plots are explained as follows: Q = Quaternary Sediments, N = Neogene Sedimentary Rocks, Pg = Paleogene Sedimentary Rocks, Ts = Tertiary Sedimentary Rocks, Ks = Cretaceous Sedimentary Rocks, Jms = Jurassic Metamorphic and Sedimentary Rocks, Tr/J = Triassic and Jurassic Rocks, and pC = Undivided Precambrian Rocks.

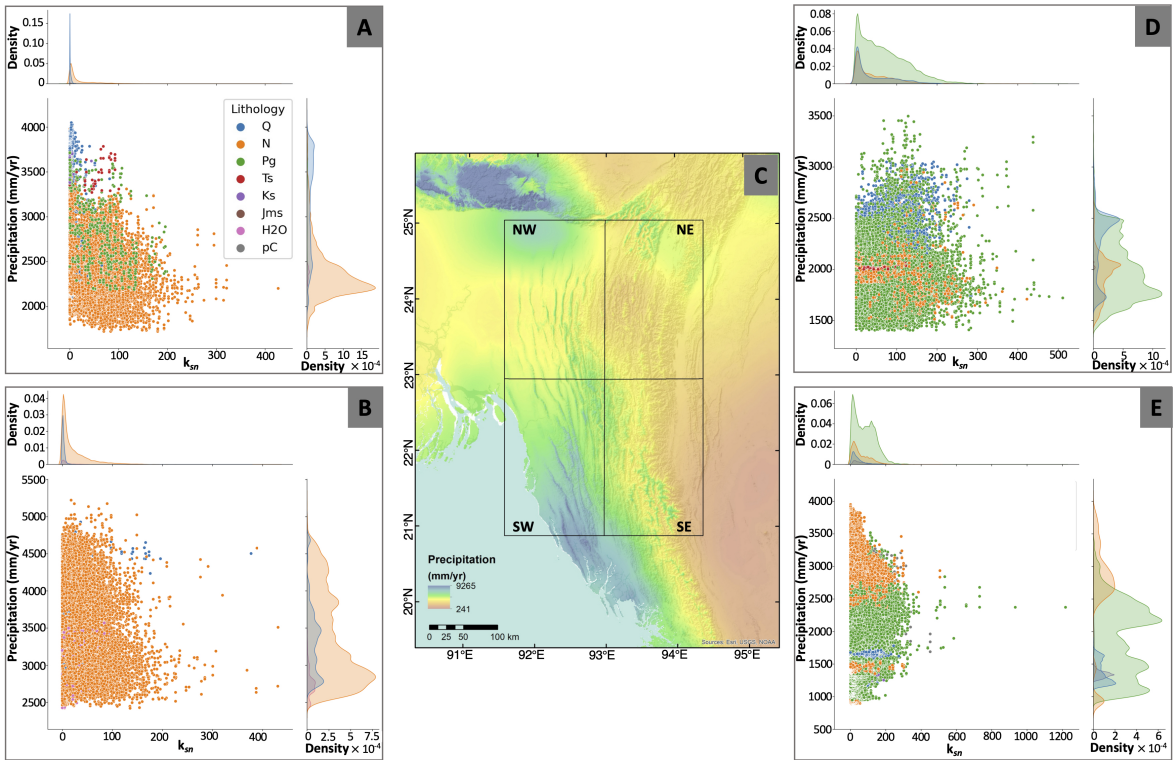

Figure 3.15: Scatter and KDE plots showing the correlation between precipitation/geologic map unit and k_{sn} values. (a, b, d, e) the scatter plots of annual precipitation rates and k_{sn} values, and the KDE plots of the precipitation rates and k_{sn} values of individual geologic units (indicated by different colors) of the streams located in NW, SW, NE, SE blocks shown in (c), respectively. The lithology abbreviations on the plots are explained as follows: Q = Quaternary Sediments, N = Neogene Sedimentary Rocks, Pg = Paleogene Sedimentary Rocks, Ts = Tertiary Sedimentary Rocks, Ks = Cretaceous Sedimentary Rocks, Jms = Jurassic Metamorphic and Sedimentary Rocks, H2O = Other Regions Water Triassic and Jurassic Rocks, and pC = Undivided Precambrian Rocks.

the studied divide segments are mostly static, except WDIV2 of A1 and northern portions of A2 and A3. This suggests that by analyzing the observed variation in geomorphic indices mentioned in the Methods section and the maps of lithology and precipitation (Figure 3.3), we will be able to investigate the spatial patterns of tectonic uplift around the studied divide areas across the IBR.

Use of k_{sn} as a proxy for tectonic rock uplift rates

A number of studies suggest that k_{sn} values are non-linearly correlated with tectonic rock uplift rates (e.g., Snyder et al., 2000 and Duvall et al., 2004). For example, Cyr et al. (2010) observe that the k_{sn} values of streams in the Apennines in Italy and independently determined rock uplift rates have a logarithmic correlation. The k_{sn} values increase as the uplift rate increases and level out at an uplift rate threshold of approximately 1 mm/yr (Cyr et al., 2010). In contrast, in some areas, e.g., the Siwalik Hills of central Nepal, k_{sn} values appear linearly correlated to the denudation rates, indicating simple stream adjustment due to differential rock uplift (Kirby and Whipple, 2012, 2001). More quantitative analysis (e.g., estimating denudation rates using cosmogenically-produced radionuclides such as Be^{10}), is indicated to assess the k_{sn} -based findings in the IBR and to more rigorously determine the rock uplift rates. Nonetheless, we hold that our regional study of k_{sn} and other geomorphic indices is useful, as it can indicate regional rock uplift rate patterns and can be used as a preliminary basis to identify locations where more detailed analysis and field investigations are warranted.

Regional Tectonics and Variations in Lithology and Precipitation

According to the distribution of regional geomorphic indices (Results - Tectonic Uplift Investigation), the eastern IBR seems to be tectonically more active even though the deformation front has been migrating westward as suggested by a westward-younging trend of anticlinal formation in the outer belt (Betka et al., 2018). The areas in the east (between the CMF and KF in the north and between the LF and ELF in the south, Figure 3.1a) have higher HI and relief values, indicating greater variation in elevation than in the west. Similarly, there is a concentration of high k_{sn} values in these areas (Figure 3.13), supporting higher rates of uplift and/or erosion in the inner belt. In addition, in the region between the TF and the southern CMF, these indices are relatively higher than in the surrounding areas, and the TF follows the transition from relatively high to low morphometric values (Figure 3.12).

The great variation in these stream indices within the region indicates significant variability of surface-process rates. This appears consistent with evidence for distributed crustal faulting between the CMF and KF inferred from seismicity and reverse focal mechanisms (Chit Thet Mon et al., 2020) and mapped discontinuous dextral strike-slip faults (Rangin, 2017). Moreover, the k_{sn} values are relatively high between the southern CMF and the TF

location. Overall, both basin- and stream-scale geomorphic indices support higher uplift rates in the eastern IBR (inner belt region) than in the western outer belt area.

The spatial distributions of the geomorphic indices have a few similarities with the patterns found in the precipitation map (Figure 3.14). By comparing the precipitation and k_{sn} maps of the area west of longitude $\sim 93^{\circ}$ (western IBR), we observe that there are higher precipitation rates in the region above latitude 23° (northern IBR) than the region below latitude 23° (southern IBR). This is somewhat similar to the k_{sn} pattern and streams in the southwestern IBR have somewhat higher k_{sn} values than those in the northwestern region (Figure 3.13 and 3.14). However, when we extract the precipitation rates, geologic map unit and the k_{sn} values of the points along the streams in the western block and create scatter and KDE plots of these extracted values, neither precipitation rates nor underlying geology appear to have clear correlations with the k_{sn} values (Figure 3.14d-e). The streams located in the western region are dominantly in Quaternary deposits and Neogene sedimentary rocks and exposed to a wide range of precipitation rates, ranging from $\sim$1500 – 5000 mm/yr; however, the scatter plot indicates no relationship between precipitation and the k_{sn}. In addition, the KDE plots of the k_{sn} values of the streams in this western block that are located in different geologic units are not significantly different, and they show peaks at around the same k_{sn} values (< 10). Accordingly, we conclude that there is little evidence of correlation between the precipitation or lithology and the k_{sn} values for the streams across the western IBR.

Comparing the spatial k_{sn} distribution with the precipitation and geologic maps in the eastern IBR (longitude $> 93^{\circ}$, Figure 3.14), we note an area in the south, around latitude 21° - 22°, where the precipitation rates are greater than in the remaining eastern IBR region, and the also have relatively high k_{sn} values. However, there are also areas where we do not observe this relationship between the precipitation rates and k_{sn} values. We also find that the eastern streams have higher k_{sn} values than those in the west, opposite to the general trend in precipitation rates. This suggests that precipitation rates do not dominate the topographic expression of the range and other factors, such as higher tectonic rock uplift rates, govern the drainage evolution and surface morphology in the eastern region. A more detailed analysis, using scatter and KDE plots, also indicate that neither precipitation rates nor first-order variations of geology have a strong relationship with the k_{sn} values (Figure 3.14). The only different point is that the streams located in the Paleogene sedimentary rocks seem to have a wider range of k_{sn} values than those located in the other geologic units. We also created the same plots for smaller subregions, but the results remain the same (Figure 3.15). Overall, we again do not observe that the precipitation rates and lithology have strong influences on the k_{sn} values in the eastern IBR.

Accordingly, the variations of the studied morphometric indicators do not appear to be a result of first-order variations in underlying geology and associated erodibility (Burbank et al., 2003; Kirby and Whipple, 2012). More-detailed geologic mapping and quantification of the erodibility of different rock types, higher resolution precipitation records, quantification of erosion rates using cosmogenic isotopes, and mapping of the distribution of active faults for the entire region will be important targets for future work in this area.

Tectonic Uplift in Eastern IBR

We find relatively high values of studied geomorphic indices concentrated in the eastern IBR. In addition, most segments of the western divide A1 and southern portions of the eastern divides A2 and A3 are suggested by χ and the Gilbert metrics to be static, allowing us to use geomorphic indices, i.e., relief, HI and k_{sn}, together with precipitation and lithology maps to study the spatial pattern of relative tectonic uplift rates across this region. The eastern NS divides, especially the southern sections, are located in a zone of relatively low precipitation rates with no obvious variation in geology (Figure 3.3), but the studied geomorphic indices are relatively high in this area (Figures 3.12 and 3.13). According to our findings, the eastern IBR is likely tectonically active. This is also consistent with Chit Thet Mon et al. (2020)'s observation of thrust-faulting events in the seismic zone in the lower crust in the eastern IBR and the finding of Betka et al. (2018) that the TF is the westernmost of several more deeply rooted young thrust faults within the inner belt. We found a transition from high to low geomorphic indices around the TF, and high k_{sn} values in the area between the east side of the TF and the southern CMF. This indicates that the distributed tectonic uplift within the inner belt region is due to active slip on multiple out-of-sequence reverse faults. Although the fold activity has migrated to the west (Betka et al., 2018), there are likely active out-of-sequence thrusts in the east that are still able to generate permanent uplift.

Alternatively, west-directed gravitational forces associated with the Tibetan lower-crustal flow have been suggested to have played a major role in the IBR uplift since the Neogene (Copley and McKenzie, 2007; Rangin et al., 2013). We believe that the effect of crustal flow in the IBR is likely to be minor due to the existence of the SF, which possibly has been deflected by the flow (Rangin et al., 2013), and it may not extend across the lower lying area between the eastern IBR and the SF. Both our observations of the high geomorphic indices in the eastern IBR and the existence of seismicity and thrust events in the lower crust to 40 km depth (Chit Thet Mon et al., 2020) argue against flow in a low-viscosity lower crust. Accordingly, with the existence of these active thrusts, the eastern inner belt region is likely to still be active and capable of producing large earthquakes and significant amounts of uplift (e.g., Wang et al., 2014).

3.6 Conclusions

Evaluation of Gilbert metrics (channel elevation, stream gradient and relief) and χ values alongside three major drainage divides in the IBR suggests that most portions of these divides are stable, allowing us to investigate the tectonic uplift pattern relying on morphometric analysis of streams and basins in the region. By considering the basin- and stream-scale geomorphic indices, as well as precipitation and lithology maps, we find that active tectonic uplift is likely a major factor governing the topographic expression of the areas around the eastern divides in the IBR. Even though the active deformation front of the IBR is migrating westward, we conclude that the eastern inner belt region experiences higher uplift rates. This

is likely due to multiple, deeply rooted out-of-sequence thrusts in the eastern IBR (Betka et al., 2018), which are also indicated by small earthquakes with thrust mechanisms in the lower crust (Chit Thet Mon et al., 2020).

Chapter 4

Thrust Sequence in the Western Fold-and-Thrust Belt of the Indo-Burma Range Determined from Fluvial Profile Analysis and Dynamic Landform Modeling

4.1 Abstract

The Indo-Burma Range (IBR) is a forearc fold-and-thrust belt that evolved under oblique convergence between India and the Burma microplate. IBR convergence is understood to be absorbed by north-striking dextral strike-slip faults and a west-propagating fold-and-thrust belt (FTB), however, the FTB spatio-temporal evolution and its seismic potential remain an area of active research. This study combines geomorphic and kinematic analyses to explore simple thrust-propagation scenarios for the IBR outer belt. We use a 30 × 30 m SRTM digital elevation model and investigate four river basins in the outer belt by extracting antecedent tributaries that cross young, NS-striking antiforms and analyzing their fluvial profiles. To help interpret the profiles, we explore first-order surface dynamics models based on four possible scenarios of the FTB evolution, including cases of sequential propagation, partial reactivation, continuous reactivation, and synchronous thrusting. We compare our modeled stream profiles and knickpoint locations to the IBR river profiles. The shapes of the profiles between knickpoints are most similar to model results of sequential propagation and continuous reactivation of older structures. This suggests that as younger antiforms start rising in the west, the eastern folds are still active. The stream profiles of the synchronous thrusting model also demonstrate similar shapes with the IBR tributaries crossing the westernmost antiforms. Results from a numerical FTB experiment with a weak detachment overlain by stronger sediment layers predicts cyclic periods of frontal ramp propagation and fault

reactivation. Overall, our findings suggest alternating periods of FTB propagation and fault reactivation in the outer belt, implying that earthquakes may alternately rupture to the deformation front and/or along splay thrusts in the wedge. The shapes of antecedent stream profiles crossing active FTB may record information about the sequence of ramp propagation and can be studied to inform the kinematic evolution of FTB.

4.2 Introduction

Analysis of stream patterns and quantitative investigation of the geomorphology of active fold-and-thrust belts is important for improved understanding of the structural evolution of accretionary wedges. In foreland regions, there are generally two major types of stream flows, which are longitudinal and transverse rivers (Burbank et al., 1996). The longitudinal rivers flow in synclinal valleys along the trend of the antiforms, while the transverse rivers follow the regional slope of the accretionary wedge and run orthogonally to the strike of the fold structures. Additionally, antecedent streams are common within fold-and-thrust belts, which are the channels of transverse rivers that formed prior to the formation of an uplift and are able to maintain their course across a rising structure over time (e.g., Burbank et al., 1996; Alvarez 1999). For an antecedent stream to maintain its course across an uplift (i.e. antiform), the erosion rate should be the same or greater than the rate of the tectonic uplift. Even when the antiforms have uplifted by several hundred meters, the rivers can still maintain their original flow directions (Burbank et al., 1996). Since antecedent streams are channels that can maintain their course during the anticlinal formation, their stream profiles can be used to investigate the tectonics of the antiforms that the streams cut across.

To illustrate the response of the landscape to the active tectonics, one of the widely used geomorphic investigation approaches is longitudinal river-profile analysis (i.e., Whipple and Tucker, 1999; Kirby and Whipple, 2001; Aiken and Brierley, 2013; Bhattarai et al., 2021). The examination of fluvial profiles can detect transient states where the erosion- and uplift rates are not uniform leading to the formation of disequilibrium state features, such as knickpoints (Stock et al., 2004; Wobus et al., 2006; Kirby and Whipple, 2012). The shape of the fluvial profiles can also indicate an equilibrium state, exhibiting a concave, graded profile that suggests a balance between erosion and uplift. In contrast, a convex profile denotes an unsteady state (Wobus et al., 2006; Bhattarai et al., 2021). Such transient signals along fluvial profiles are significant since they can reveal the recent tectonic evolution, i.e. variation in tectonic rock uplifts. Moreover, multiple equilibrium conditions can be separated by the knickpoint locations along the profile, where there are differential incision rates along a river (Wobus et al., 2006). For example, the channel segments below and above a knickpoint location are eroded at different rates. Over time, the upper segment profile will be subsumed by the lower profile as the knickpoint migrates upstream.

In this paper we model the landscape response to various scenarios of thrust propagation to test (1) how antecedent rivers respond to fault propagation, and (2) if antecedent river profiles record information about the kinematic evolution of fold-thrust belts. We examine

stream profiles and knickpoint locations of the antecedent channels in the Indo-Burma Range (IBR) fold-thrust belt and compare these natural examples with the results from the surface dynamics models of simplified representations of the system to better understand the tectonics of the thrust propagation style in active fold-thrust belts. We explore the hypothesis that active thrust tectonics in our study region (the IBR) partly controls the shape of antecedent stream profiles, i.e. changing from concave to convex profiles, and thus, fluvial profiles may be used to understand the kinematic evolution of fold-thrust belts. Our findings contribute to the current understanding of the active tectonics and thrust propagation in the IBR region and may be applicable to other active fold-thrust belts within sedimentary basins.

4.3 Tectonic Setting of the Indo-Burma Range Fold-Thrust Belt

The Indo-Burma Range (IBR) is a subaerial accretionary wedge that formed due to the oblique subduction of the Indian Plate below the Burma microplate and resulting accretion of a thick succession of late Cenozoic to modern sediments of the Ganges–Brahmaputra Delta (Curray et al., 1979; Johnson and NUR ALAM, 1991; Mitchel et al., 1993; Gani and Alam, 1999; Alam et al., 2003; Sikder and Alam, 2003; Steckler et al., 2008; Najman et al., 2008; Rangin et al., 2013; Govin et al., 2018; Sincavage et al., 2020; Betka et al., 2021; Figure 4.1). The range is about 1400-km long and extends for about 375 km from east to west (Steckler et al., 2016). The average slope across the westernmost IBR is approximately 0.1° and increases to the east to ∼0.5° (Steckler et al., 2008; Betka et al., 2018). The prism is divided into three sections, which are the eastern inner belt (east of the Tut Fault, TF), the western outer belt (between TF and Thrust Front) and the westernmost/frontal blind belt (Betka et al., 2018, Figure 4.1). This study focuses on the western outer belt region between latitude 21N and 24N (Figure 4.1b).

Previous studies have investigated the structural geology and tectonics of the outer-belt region of the IBR. The first quantitative analysis of the IBR fold-belt structure is presented in Sikder and Alam (2003) who interpret detachment and fault-propagation folds from 2D industry seismic lines in Bangladesh. They identify a regional décollement within a low-velocity horizon beneath the buried structures of the blind belt. In addition, Zalid and Uddin (2005) found a reduction in acoustic velocity of the subsurface strata from 3 – 4 km depth at the Sitakund anticline in southeastern Bangladesh (an area around the Sitakund Fault in Figure 4.1). Later, Maurin and Rangin (2009) interpret seismic reflection data and use limited field mapping from the outer belt to suggest that the structural evolution of the IBR is defined by a transition from rapidly propagating thin-skinned folding and thrusting to thick-skinned right-lateral strike-slip and reverse faulting. Maurin and Rangin (2009) suggest that the initial thin-skinned advance of the wedge is a response to high rates of sedimentation within the Ganges-Brahmaputra Delta, and the later thick-skinned deformation is required to maintain critical taper and accommodate strain partitioning in the forearc. In contrast, Betka

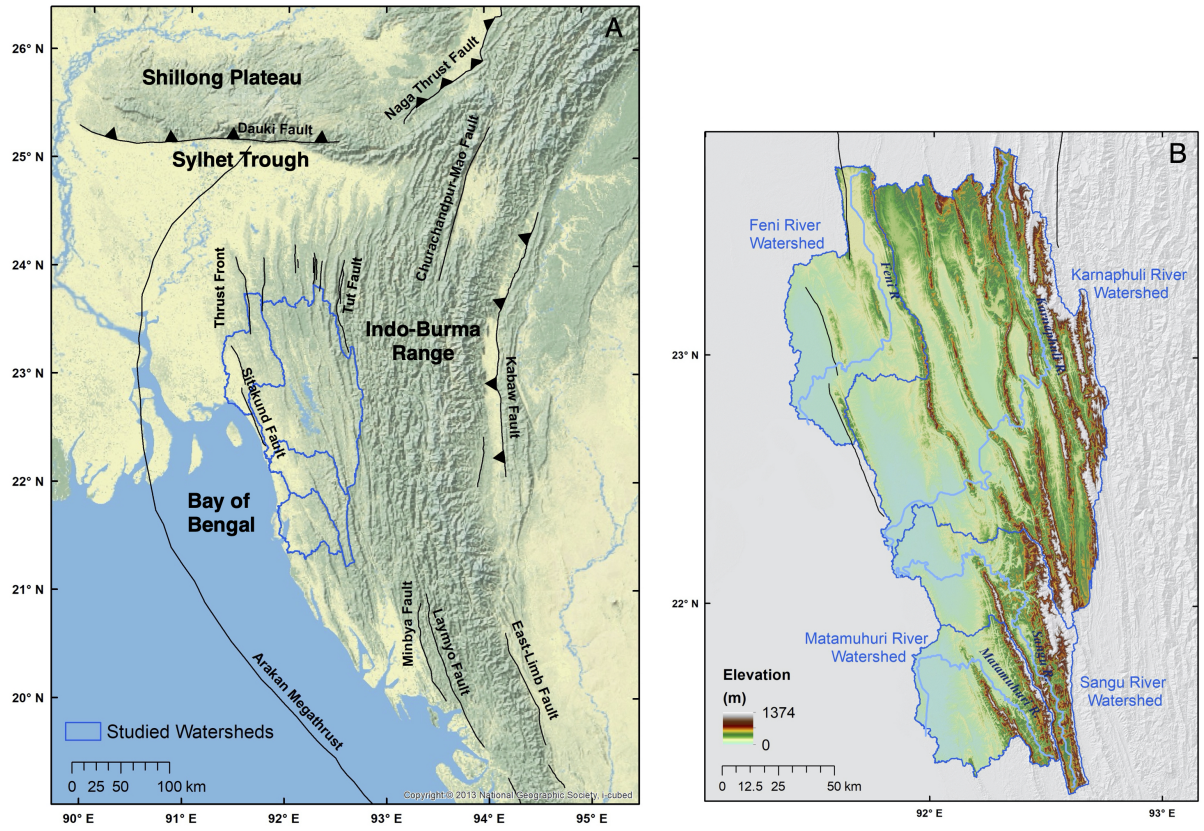

Figure 4.1: Topography and active faults in the study region. (a) The entire IBR region. The black lines are mapped faults (Wang et al., 2014; Betka et al., 2018), and the blue polygons indicate the watersheds of the studied rivers (b). (b)The targeted river basins in the western outer-belt region include the Feni, Karnaphuli, Sangu and Matamuhuri Rivers. The light blue lines indicate the main rivers. Color-contoured shaded elevation illuminates NS-oriented fold-and-thrust structures.

et al. (2018) present detailed field mapping and kinematic analysis of the outer belt and find evidence for only a thin-skinned fold-thrust structural style within the outer belt. Betka et al., (2018) model the kinematic evolution of the outer belt overriding a shallow décollement with a minimum depth of $\sim 3 - 4$ km. They propose that overpressured shale is required to lower the effective-friction angle of the basal décollement (i.e. Davies et al., 1983) and to accommodate the rapid propagation (15 km/Myr) of a very low-taper thrust wedge (c.f. Sikder and Alam, 2003; Betka et al., 2018; Steckler et al., 2008) since ∼8 Ma (Betka et al., 2018; Sincavage et al., 2020). Recently, Bürgi et al. (2021) examined seismic reflection profiles from Bangladesh, building on the earlier work of Sikder and Alam (2003), to constrain the depth of the detachment within the frontal/blind-belt of the IBR. They find that the décollement is ∼5 km deep in the blind belt near latitude 23.5N and 24N and the detachment is folded along an E-W trending axis parallel to the westward transport direction of the fold-thrust belt, such that the depth increases to ∼9 km to the north, and also increases southward but the latter is less well constrained. This north to south folding of the IBR is a response to the flexural load of the Shillong Massif (Najman et al., 2016; Bürgi et al., 2021). Bürgi et al., 2021 also document the transition of the folding and thrusting kinematics observed in the IBR from initial detachment folding in the blind thrust belt to fault-propagation and fault-bend folding with increasing magnitudes of shortening. In another recent study, Das et al., (2021) present field mapping and structural analysis of ductile shale in the core of the anticlines to propose an alternative interpretation of the IBR. They consider the whole of the IBR as a train of detachment folds developing in poorly consolidated water-saturated sediments of the IBR that behave like a viscous wedge and compare the IBR structures with analog viscous wedge models to support their interpretations. While detachment folding is an important mechanism of fold growth in the IBR (Sikder and Alam, 2003; Das et al., 2021; Bürgi et al., 2021), fault-related folding structures are also imaged in seismic data (Sikder and Alam, 2003; Islam, Habib, et al., 2015; Bürgi et al., 2021) and recognized in field studies of the IBR (Betka et al., 2018; Maurin and Rangin, 2009), indicating that fold growth is accommodated by a combination of fault-related and detachment folding processes. Although a number of studies have investigated the kinematic evolution of the outer and blind belts, considerable debate remains regarding the spatio-temporal development of the thrust systems of the IBR.

In a previous study of the geomorphic expression of active deformation across the IBR, Maneerat and Bürgmann (2022) found evidence of out-of-sequence thrusting in the eastern inner-belt region which is consistent with the findings of Betka et al. (2018), Sincavage et al. (2020), and Chit Thet Mon et al., (2020). In the outer belt, Betka et al. (2018) document a strongly linear increase in the cumulative shortening (i.e. slip on the décollement) toward the east across eight of the outer-belt antiforms, which each have a characteristic shortening of $\sim 4.8 \pm 2.5$ km (mean and standard deviation) and propagated toward the foreland (westward) at a rate of ∼15 km/Myr. This linear trend in cumulative shorting across the outer belt can be achieved by a number of possible sequences of thrust propagation and fold growth. For example, the thrusts could break forward sequentially with each achieving their maximum shortening magnitude before breaking a new structure in the foreland to the west (the sequential propagation scenario in Figure 4.2). Alternatively, the thrusts could propagate forward in-

sequence from east to west with initially lower shortening magnitudes and later be reactivated out-of-sequence until the maximum shortening is achieved for each structure (sequential propagation with partial reactivation scenario in Figure 4.2). Similarly, the thrusts could break forward (westward) in sequence with initially lower shortening magnitudes and grow by continuous out-of-sequence reactivation of all the older structures (sequential propagation with continuous reactivation scenario in Figure 4.2). Finally, the thrusts could all form together and continue to grow synchronously (continuous thrusting scenario in Figure 4.2). Any of these sequences of thrust propagation are permissible based on kinematic constraints because the thrust ramp spacing is greater than the anticline widths, and thus, there are no overprinting relationships between the outer-belt folds (except where the fold tips overlap, Figure 4.1a). In fact, it is also kinematically permissible for the structures to propagate in any sequence (e.g. first A8, then A1, then A3, then A6, then A2... etc. Figure 4.2b), however, we consider this unlikely, because the structural style of the outer and blind belts of the IBR, constrained with subsurface seismic data (Sikder and Alam, 2003; Maurin and Rangin, 2009; Bürgi et al., 2021), indicates a generally westward propagation of the thrust system. The inferred foreland propagation of faults and folds in the IBR is also consistent with the basic paradigm of thrust propagation in foreland regions (i.e. Bally et al., 1966; Boyer and Elliott, 1982; McClay, 1992), although it is widely recognized that out-of-sequence reactivation of old thrusts (or formation of new thrusts) commonly occurs in fold-thrust belts world-wide (Stockmal et al., 2007; J. E. Wu and McClay, 2011) and in the IBR (Betka et al., 2018; Sincavage et al., 2020), as thrust systems adjust to maintain critical taper (Davis et al., 1983). Although there are no absolute kinematic constraints on the sequence of thrust propagation in the IBR, herein we investigate how various sequences of thrust propagation control the geomorphic expression of transverse rivers that cross a fold-thrust belt.

4.4 Methodology

Since the sequence of fold-thrust belt propagation likely controls stream patterns and shapes of their fluvial profiles, we investigate the profiles of four major river tributaries in the outer belt and compare them with our surface dynamics modeling results. The geomorphic study will provide the information of the potential thrust sequence and active tectonics across the region. We also consider numerical models of fold-thrust belt evolution with weak detachment condition.

Geomorphology Investigation

We employed geographical information system software (ArcGIS) and a computational tool (TopoToolbox, Schwanghart and Scherler, 2014) to investigate the antiform characteristics, i.e. crest length to width ratio, stream profiles and knickpoints along 20 tributaries of the four major rivers in the western, outer belt of the IBR, which are Feni, Karnaphuli, Sangu and Matamuhuri Rivers, from the digital elevation model (DEM, Figure 4.1b). We utilized a 30 $\times$

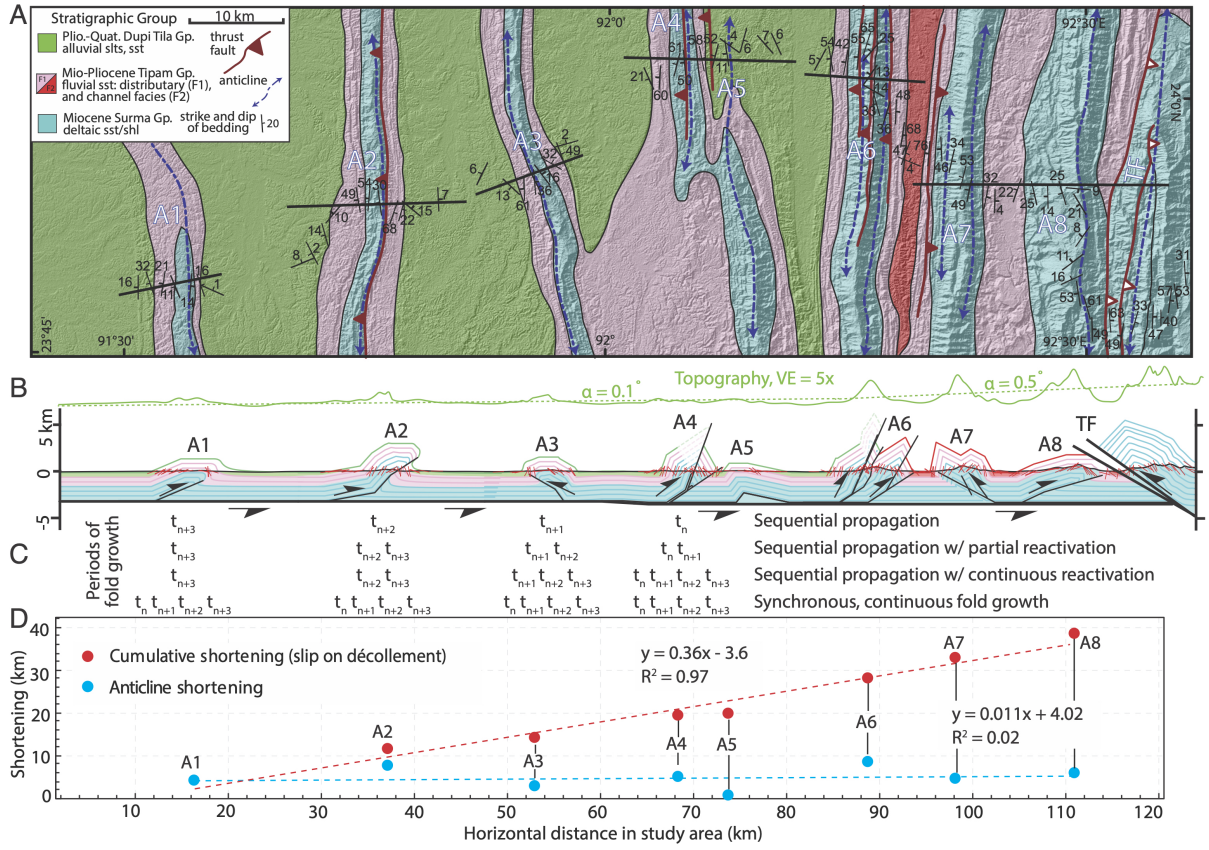

Figure 4.2: Geologic map and four possible kinematic thrust propagation scenarios, modified after Betka et al. (2018). (a) Simplified geologic map. (b) Balanced kinematic model of the outer belt of the IBR at latitude 24N. (c) Table showing four possible kinematic scenarios with periods of forward propagation and fold growth for structures A1 – A4 in the outer belt, starting from time tn and propagating westward. See text for a complete description of each kinematic scenario. For simplicity, propagation sequences are only given for structures A1 – A4, however, the four kinematic scenarios can be readily extrapolated to all of the structures in the outer belt. (d) Plot of individual anticline shortening and cumulative shortening (i.e. slip on décollement) across the outer belt.

30 m pixel size DEM created from radar interferometric data collected by the NASA Shuttle Radar Topography Mission and distributed by the U.S. Geological Survey. We created the stream profiles of 20 selected tributaries and determined the knickpoints along the profiles using the knickpointfinder function from the TopoToolbox (Schwanghart and Scherler, 2014). We applied the constrained regularized smoothing algorithm presented in Schwanghart and Scherler (2017) to select the optimal parameter called *tol*, which stands for tolerance. This parameter is an important variable helping to increase the accuracy of knickpoint detection and mitigating the effects of DEM data artifacts or noise. We further utilized the information of the IBR anticlinal structures and streams to (1) create a simple surface dynamics model to resemble the western outer belt and (2) compare the IBR antecedent fluvial profiles and knickpoint locations to the modeled results.

Surface Dynamics Modeling

In this study, we employed Landlab (Hobley et al., 2017) to create first-order surface dynamics models resembling the possible scenarios of thrust propagation in the western IBR. We explain individual details of the models as follows.

Fold Geometries

Before creating the folds, we examined the fold structures in the western IBR using the DEM. We assumed that the folds in the western IBR were incipient folds and measured their lengths and widths from the DEM, which are in the range of 24 - 75 km and 5 - 9 km, respectively. The average ratio of the fold width to crest length is approximately 1 to 7. In the model, we scale the fold width to 1 km (∼7 km in the DEM) and crest length to 7 km (∼49 km in the DEM, Table 4.1). The modeled folds are symmetric and trend north.

General Model Setup

For all of our models, we assigned a study region geometry of 150 × 150 cells (rows × columns) with a cell size of 200 × 200 m (Table 4.1). We assigned a regional slope gradient up toward the east in order to let the streams flow down to the west as observed in the outer belt (Figures 4.1 and 4.2b). We assumed uniform lithology and precipitation rates across the entire model domain. For this study, we created a simple model of three folds resembling the westernmost region in the IBR where the incipient folds are about to form or have recently formed. The change in elevation over time in the models are due to three major factors, fluvial erosion, linear diffusion applied to hillslopes, and uplift as described in the following equation (Hobley et al., 2017):

$$\frac{\partial z}{\partial t} = -K_{sp} A^m S^n + K_{hs}(\frac{\partial^2 z}{\partial x^2}) + U$$

where the first term on the right-hand side of the equation is the stream power erosion equation or the fluvial erosion term in which K_{sp} is the coefficient of the fluvial erosion, A is

drainage area, S is the local channel slope, and m and n are positive exponents, typically m/n is 0.5 (e.g. K. X. Whipple and Tucker, 1999). The second term is the linear diffusion applied to hillslopes in which K_{hs} is the coefficient of the linear diffusivity, z is the elevation and x is the horizontal distance (Roering, 2008). U is an uplift rate. The parameters of these terms in the previous equation are specified in Table 4.1 and applied identically for all modeling periods and scenarios, which are explained in the next sections.

Parameters	**Values/Explanation**	**Comments**
Number of Cells	150 × 150	Rows × Columns
Cell Size	200 × 200	
Boundary Conditions	Outflow only on the West	The stream directions before the folds are formed are only in the EW directions.
Initial Noise on Elevation Grid	Included	Hobley et al. (2017)
Initial Regional Slope	Included	Linear slope from the west to the east.
Regional Vertical Uplift Rate	1 mm/yr	Imposed uniformly over time. We set this to maintain the background topography.
Flow Accumulator Parameters	$K_{sp} = 1 \times 10^{-5}$ $m/n = 0.5/1$	These values are typically and widely used (Hobley et al., 2017).
Linear Diffusion Coefficient	$K_{hs} = 0.005 m^2/yr$	Hillslope diffusion coefficient in humid/temperate regions – moist winter and dense vegetation (Roering et al., 1999).
Initial Fold Geometry	1-km width and 7-km crest length	The imposed western embryonic fold width – crest length ratio is ∼1:7.
Fold Axis Spacing Distance	3 km	

Table 4.1: Parameters used for the surface dynamics models.

Modeling Periods

There are five different periods used in our models (Table 4.2):
(t_0) the streams start to flow and evolve for 2 Myr,
(t_1) the eastern fold starts to form and stays tectonically active for 300 kyr,
(t_2) the middle fold begins to rise and uplifts for 200 kyr,
(t_3) the western fold initiates and rises for 150 kyr,
(t_4) all three folds stop uplifting and no longer laterally grow for 500 kyr.

We consider four simple model scenarios (Models A - D) as explained below, and generally t_0 and t_4 are the common modeling periods used for all four models. However, t_1, t_2 and t_3 are only applied for Models A - C (Table 4.2).

Modeling Scenarios

We created a total of four models with three anticlines, western, middle, and eastern anticlines, included in each model. Generally, we imposed a lateral propagation of active folds as they are uplifting vertically. Then, we set individual models with different vertical uplift

Modeling Periods (kyr)	Model 1	Model 2	Model 3	Model 4
t_0 - Before anticlinal formation		2000 (10)		
t_1 - During eastern fold growth		300 (1)		$t_1 + t_2 + t_3$
t_2 - During middle fold growth		200 (1)		or
t_3 - During western fold growth		150 (1)		650 (1)
t_4 - After cessation of Fold Growth		500 (1)		

Table 4.2: Study periods and time steps used in the models (in kyr). The numbers in the brackets are the time steps assigned in each study period (t).

and lateral fold growth rates for each of the three individual folds over time (Table 4.3). The following four models represent the possible scenarios of the antiform formation in the outer belt of the IBR.

(1) Model A (Sequential propagation): After the t_0 period, the eastern fold starts to form (t_1). Over time, when the middle fold rises, the eastern fold stops uplifting and growing laterally northward (t_2). Likewise, when the western antiform rises, the middle fold stops uplifting (t_3). Lastly, after the western fold evolves for 150 kyr, it stops rising, and only the uniform regional uplift and erosion process take place (t_4).

(2) Model B (Sequential propagation with partial reactivation): After the t_0 period, the eastern fold starts to rise and evolves for 300 kyr (t_1). Then, as the middle fold begins to rise, the eastern antiform remains active but its vertical and lateral growth rates decrease (t_2). Later on, as the western fold starts to form, the eastern fold stops uplifting and the middle antiform's vertical uplift and lateral growth rates reduce (t_3). Subsequently, the western and middle antiforms are no longer active (t_4).

(3) Model C (Sequential propagation with continuous reactivation): This model is quite similar to the Model B. The difference between the two models is that for the Model C, when the western fold starts to rise, the older antiforms in the east are still active with similar vertical and lateral fold growth rates.

(4) Model D (Synchronous, continuous fold growth): All three folds start rising at the same time. They evolve for 650 kyr, which is the combination of t_1, t_2 and t_3 of Models A - C, before all antiforms stop uplifting (t_4).

These models are designed to capture the first-order fluvial profile patterns and effects of antiform propagation sequence on the landscape evolution of the fold-belt. We do not intend to find the best-fit parameters that accurately represent the IBR outer-belt observation.

Fluvial Profile and Knickpoint Observations

After obtaining the results of the surface dynamics models, we employed the MATLAB-based computational tool (TopoToolbox, Schwanghart and Scherler, 2014) to examine the selected stream profiles. We chose both antecedent and non-antecedent streams in order to compare the differences of fluvial profiles over time. We also used the knickpointfinder

Models	Modeling Periods	Vertical Uplift and Lateral Fold Growth Rates (mm/yr)		
		Western Fold	Middle Fold	Eastern Fold
Model 1 (Sequential Propagation)	t_1	0, 0	0, 0	4, 10
	t_2	0, 0	4, 10	0, 0
	t_3	4, 10	0, 0	0, 0
Model 2 (Sequential Propagation with Partial Reactivation)	t_1	0, 0	0, 0	4, 10
	t_2	0, 0	4, 10	2, 5
	t_3	4, 10	2, 5	0, 0
Model 3 (Sequential Propagation with Continuous Reactivation)	t_1	0, 0	0, 0	4, 10
	t_2	0, 0	4, 10	4, 10
	t_3	4, 10	4, 10	4, 10
Model 4 (Synchronous Thrusting)	$t_1 + t_2 + t_3$		4, 10	

Table 4.3: The vertical uplift and lateral fold growth rates assigned for individual models. The left and right numbers are the vertical uplift and lateral growth rates, respectively. t_0 and t_4 are not included in the table since the vertical uplift and lateral growth rates of the three folds are always zero during these periods. Only the uniform regional uplift rate of 1 mm/yr is applied during t_0 and t_4 periods.

function mentioned previously to find the knickpoints along the studied profiles (Schwanghart and Scherler, 2014).

4.5 Results

Geomorphic Investigation

There are two major types of stream flows in the IBR, transverse and parallel to the fold-and-thrust belt. The transverse channels represent antecedent streams that are able to maintain their course while the folds formed and grew over time. The parallel stream flows are the channels flowing along the synclinal valleys before merging with the transverse streams and flowing to the outlets. Most of the antecedent streams in the western IBR originate from higher relief regions at ∼longitude 92E - 93E. Along the antecedent streams, we find knickpoints, especially where the streams cut across the antiforms (Figures 4.3 and 4.4). In this section, we explore 20 tributaries of the four major rivers in the outer belt of the IBR, which are the Feni, Karnaphuli, Sangu and Matamuhuri Rivers (Figures 4.3 - 4.12).

Feni River

The Feni River is a ∼120-km-long river that originates from a high relief area around longitude 92E and flows westward crossing the incipient folds in the outer belt (Table 4.4). Within the Feni River watershed, we observe a low-elevation, vegetated floodplain between the folds where tributary A2 flows through (Figure 4.3a). We observe portions of five folds in the Feni River watershed. The two western antiforms are about to obliquely link while the

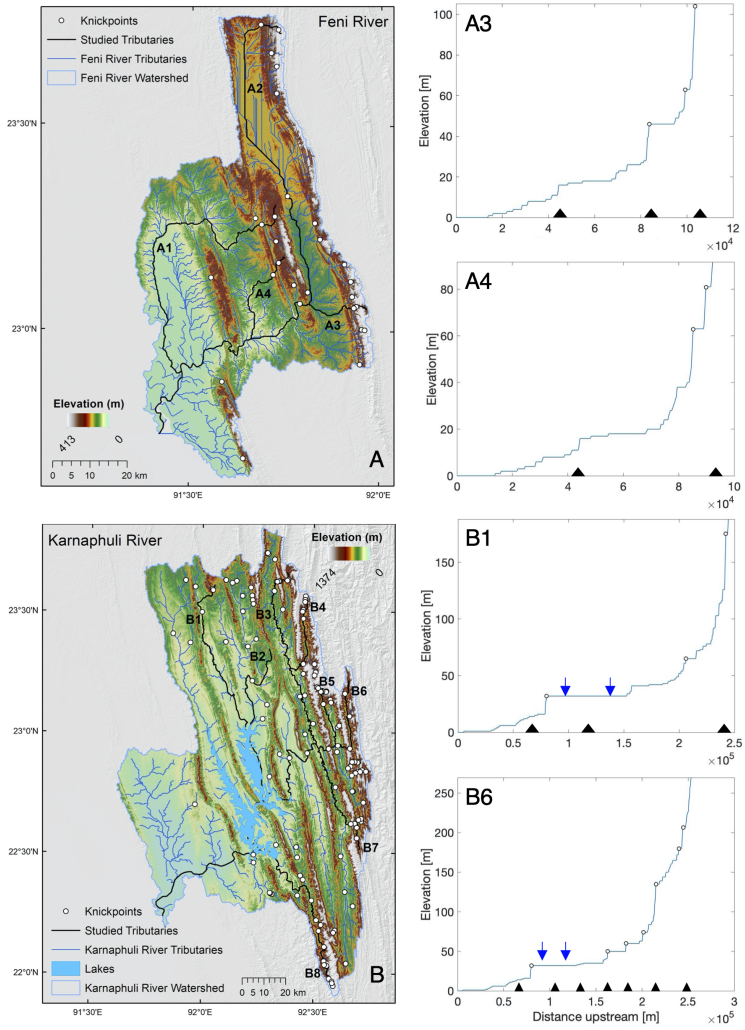

Figure 4.3: Studied rivers and examples of stream profiles. (a, b) Elevation maps of the Feni and Karnaphuli River watersheds, respectively. Color-contoured shaded-relief DEM illuminates N-S-trending fault-cored anticlines. The blue lines represent the river tributaries, and the black lines are the studied tributaries. The white circles with black perimeters represent the knickpoints. The light blue polygon indicates the Kaptai Lake, and the lake boundary data is obtained from DIVA-GIS (2019). (Profiles A3, A4) The fluvial profiles of the tributaries A3 and A4 of the Feni River whose locations are labeled in (a). (Profiles B1, B6) the fluvial profiles of the tributaries B1 and B6 of the Karnaphuli River whose locations are denoted in (b). The white circles with black perimeter and the black triangles on all four example profiles indicate knickpoints and antiform locations, respectively. The blue arrows on (Profiles B1, B6) indicate the extent of the lake.

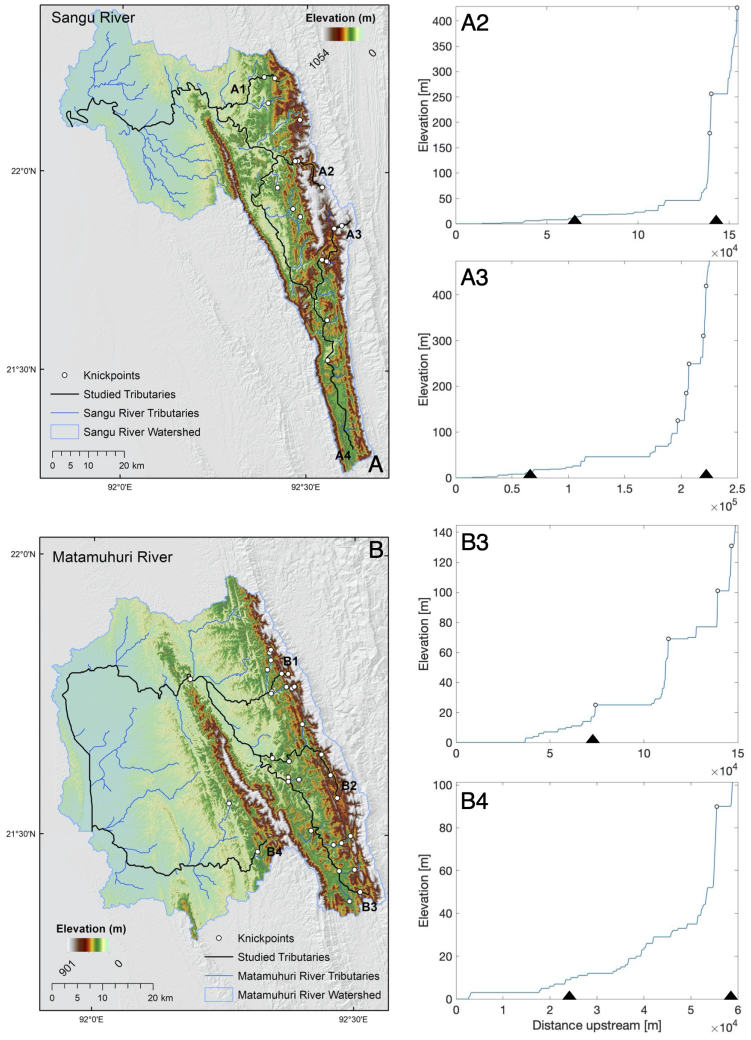

Figure 4.4: Studied rivers and examples of stream profiles. (a, b) the elevation maps within the Sangu and Matamuhuri River watersheds, respectively. The blue lines represent the river tributaries, and the black lines are the studied tributaries. (Profiles A2, A3) the fluvial profiles of the tributaries A2 and A3 of the Sangu River in which their locations are labeled in (a). (Profiles B3, B4) the fluvial profiles of the tributaries B3 and B4 of the Matamuhuri River in which their locations are denoted in (b). The white circles with black perimeter and the black triangles on all four example profiles indicate knickpoints and antiform locations, respectively.

two eastern folds seem to be already connected. Since the western folds are not completely linked, the Feni River can cut across this area through the gap (tributary A2 - 4 in Figure 4.3a). Some tributaries (e.g., tributary A1 in Figure 4.3a) initiate around the oblique fold linkage zone in the east and navigate through the northern end of the western fold.

We selected four tributaries to investigate their stream profiles and determined knickpoint locations along them. The studied profiles show slope-break locations mostly at the upper course of the channels indicating knickpoints in the eastern antiform region. The Feni River (i.e. tributaries A2 and A3 in Figure 4.3a) cuts through the southern ends of the western and eastern folds, but the fluvial profile only indicates a knickpoint where the river crosses the eastern antiform. This is because the western antiform is situated near the outlet or in the lower course of the river where the river has higher volume.

Karnaphuli River

The Karnaphuli River is a ∼270-km-long river and cuts across multiple antiforms. This river forms from a higher relief region at longitude 92.8E (Figures 4.1 and 4.3b; Table 4.4). Within the Karnaphuli River watershed, segments of several elongate antiforms appear to have overlapped and connected over time. Between these folds lies Kaptai Lake, a large reservoir built for hydropower generation (Hoque et al., 2021). This lake has two major water bodies connected by the Karnaphuli River. Overall, elevation in the lake region is lower than the surrounding areas within the watershed. Therefore, there is an accumulation of a large amount of water.

We selected eight tributaries to study their fluvial profiles. Along the profiles, there are flat segments along the extent of Kaptai Lake (light blue polygon in Figure 4.3b and blue arrows on Profiles B1,6). We find that most of the identified knickpoints are situated near the antiforms, especially in the east where the elevations are higher and the spacing between the folds is narrower than in the west (Figure 4.3b - Profiles B1,6). In addition, the slope breaks (knickpoints) along the profiles are steep even in the areas where the streams cross the higher relief eastern folds (Figure 4.3b - Profile B6). Some stream profiles also suggest a cluster of knickpoints, or a knickzone in their upper course region (e.g., tributary B8 in Figure 4.3b). These areas have higher elevation and narrower fold spacing than the surroundings.

Sangu River

The Sangu River is a ∼270-km-long river that flows around the overlapping anticlines in the southwestern IBR (Figure 4.1b and 4.4a). The Sangu River watershed encompasses portions of two antiformal structures (Table 4.4). The eastern structure seems to be defined by multiple fold linkages leading to markedly higher elevations than the other areas within the drainage basin. The spacing between the eastern and western antiforms decreases toward south from ∼25 to ∼5 km while the elevation of this area increases.

We studied the fluvial profiles of four tributaries. The tributaries A2 and A3 in Figure 4.4a originate from a high relief area around longitude 92.7E and flow through the region of

fold overlap. The profiles of these channels indicate knickpoint locations at the antiform sites (Figure 4.4 - Profiles A2, A3). The tributaries A1 and A4 do not entirely cross an antiform, but we still observe knickpoints along these channels (Figure 4.4a). For A1, the identified knickpoints are observed at locations where the stream reaches the eastern antiform. On the other hand, the knickpoints along A4 are situated between the folds where the elevation is higher and fold spacing is narrower than in the north. Overall, the knickpoints along all four stream profiles are located in uplifted and higher-relief areas of the watershed (Figure 4.4a).

	Feni River	**Karnaphuli River**	**Sangu River**	**Matamuhuri River**
Length (km)	120	270	270	290
Topography within the watersheds	Portions of five antiforms, vegetated floodplains in the northeast	Several elongate antiforms that overlapped and connected over time, Kaptai Lake between the middle folds	Portions of two antiforms	Portions of three antiforms
Number of studied tributaries	4 (A1-4 in Figure 4.3a)	8 (B1-8 in Figure 4.3b)	4 (A1-4 in Figure 4.4a)	4 (B1-4 in Figure 4.4b)
Overall fluvial profile shapes	Concave with some convex or vertical-step segments, a flat segment on A2 profile indicating vegetated area	Concave with some convex segments, a flat segment on the profiles of streams crossing the Kaptai Lake	Concave with some convex or vertical-step segments	Concave with some convex or vertical-step segments
Locations of knickpoints	Upper course of the studied channels (eastern antiform region)	Mostly in the upper course of the studied streams (eastern antiforms), some sites where the streams cross antiforms, a few near the Kaptai Lake	Upper course of the studied channel (eastern antiform area)	Upper course of the studied streams (eastern antiform area) and the site where the streams cut across the middle antiform

Table 4.4: Summary of the geomorphic investigation results of the studied rivers.

Matamuhuri River

The Matamuhuri River is a ∼290-km-long river situated to the south of the Sangu River. Its watershed includes portions of three folds (Figure 4.4b; Table 4.4). The Matamuhuri River originates from a high relief region, around longitude 92.6E where the eastern fold is located, and flows westward through the middle antiform. The spacing between the middle and eastern antiforms slightly decreases from ∼25 to 15 km southward while the elevation increases.

We analyzed the profiles of four tributaries to determine knickpoint locations. The tributaries B1-3 in Figure 4.4b initiate in the area uplifted by the eastern antiform. They merge and cut across the middle fold while the channel B4 flows through the northern end of the western fold. The B1-3 fluvial profiles suggest a knickpoint at the middle antiform site (Figure

4.4b - Profile B3). In contrast, the tributary B4 profile does not indicate a knickpoint at the antiform-crossing location, possibly due to lower elevation and greater erosion in the lower course region of the channel. However, this profile suggests a knickpoint in the upstream area where the channel reaches the middle fold. The profile shape of the B4 downstream segment is approximately concave suggesting equilibrium state (i.e., Wobus et al., 2006; Figure 4.4 - Profile B4). Overall, the observed knickpoints are located in the higher-elevation areas between the middle and eastern antiforms.

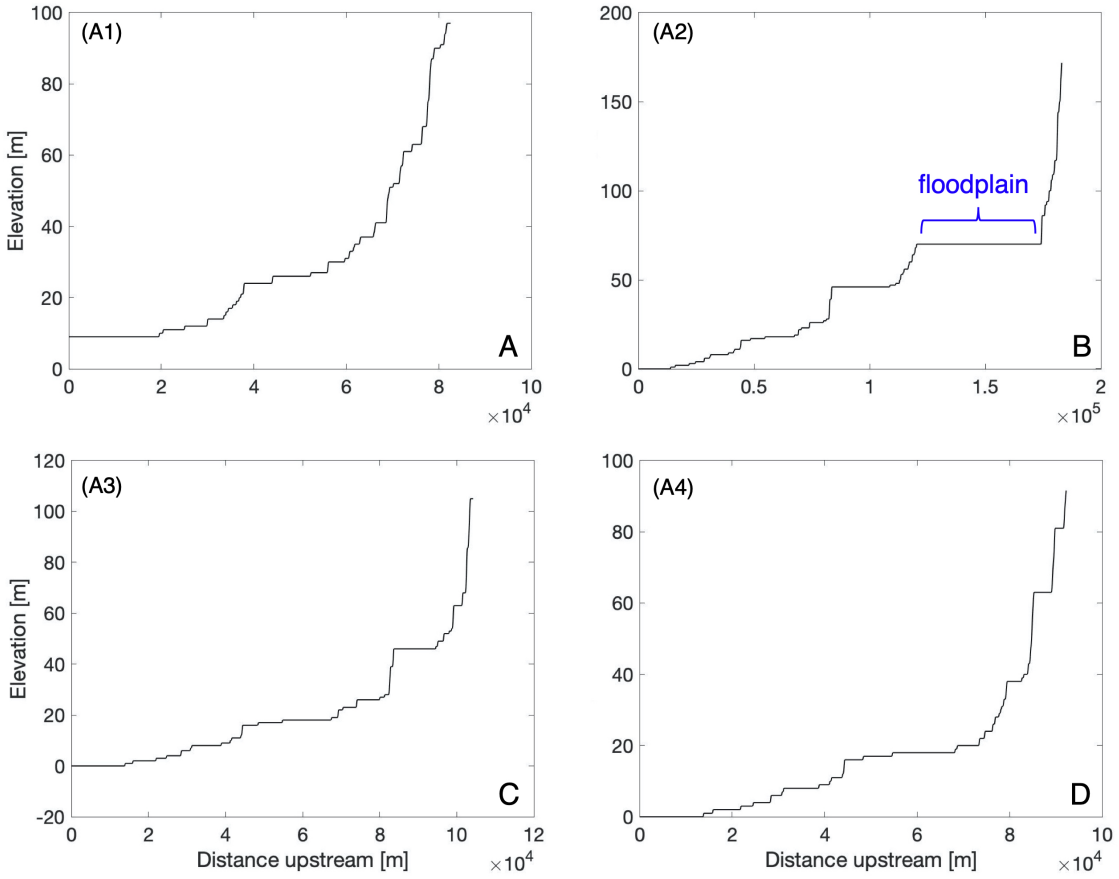

Figure 4.5: Fluvial profiles of Feni River tributaries. (a, b, c, d) the profiles of tributaries A1, A2, A3 and A4 specified on Figure 4.3a, respectively.

Surface Dynamics Models

As an antiform starts rising, we find that knickpoints are first generated at that antiform location and migrate upstream over time. The migration of the knickpoints leads to changes

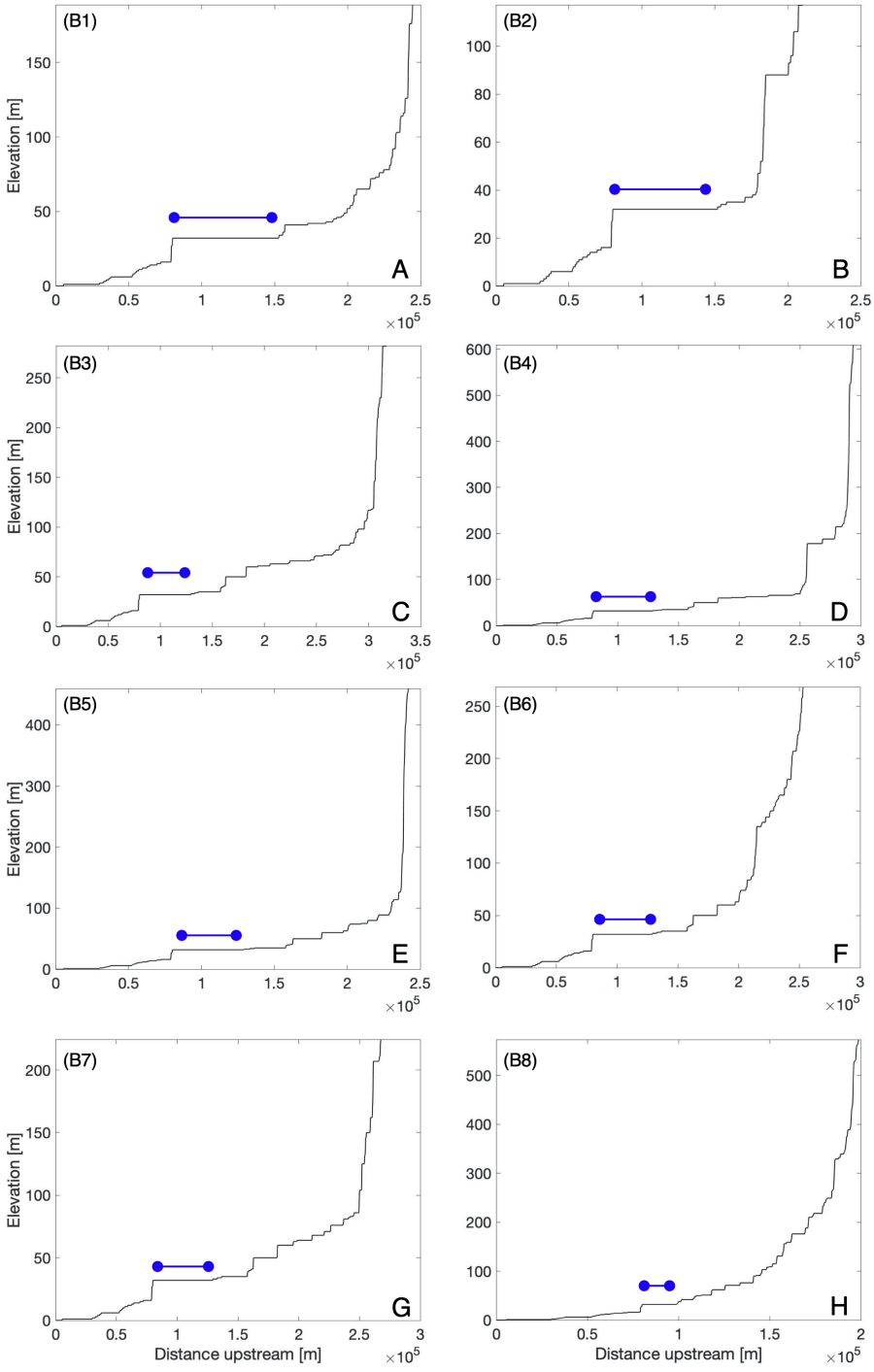

Figure 4.6: Fluvial profiles of Karnaphuli River tributaries. (a, b, c, d, e, f, g, h) The profiles of tributaries B1-8 specified on Figure 4.3b, respectively. The blue horizontal bar represents the Kaptai lake location.

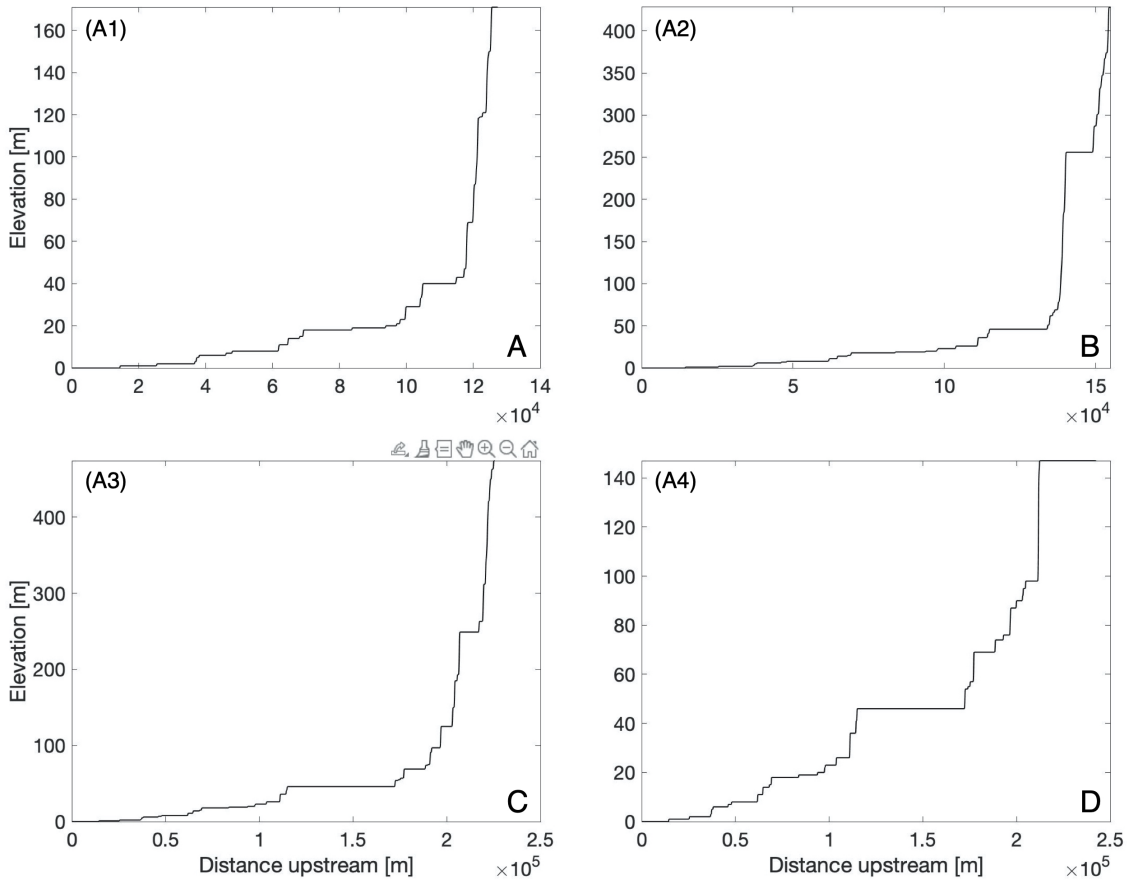

Figure 4.7: Fluvial profiles of Sangu River tributaries. (a, b, c, d) The profiles of tributaries A1, A2, A3 and A4 specified on Figure 4.4a, respectively.

in elevation of the antecedent rivers. When a fold stops uplifting, no knickpoints form at the antiform site. However, sometimes we still observe knickpoints near the inactive fold since the knickpoints generated in the downstream area propagate upstream. On the fluvial profiles of Models A - D, the recently-created knickpoints are steeper than the migrated ones. This can be used to differentiate whether the knickpoints in the modeling results indicate actively uplifting antiforms or are currently migrating upstream. In the Discussion, we further discuss the model outputs and make first-order comparisons with the observed stream profiles in the IBR.

The three Models A - C are set up identically during modeling period t_1. During t_1, the eastern antiform starts to form and evolves for 300 kyr. As the fold starts to rise, knickpoints form in the antecedent stream profiles at the antiform location (Figure 4.13a-b, e-f). These slope-break segments (knickpoint locations) become smoother and develop a convex shape over time. Knickpoint migrations expand the convex segments on the profiles, extending

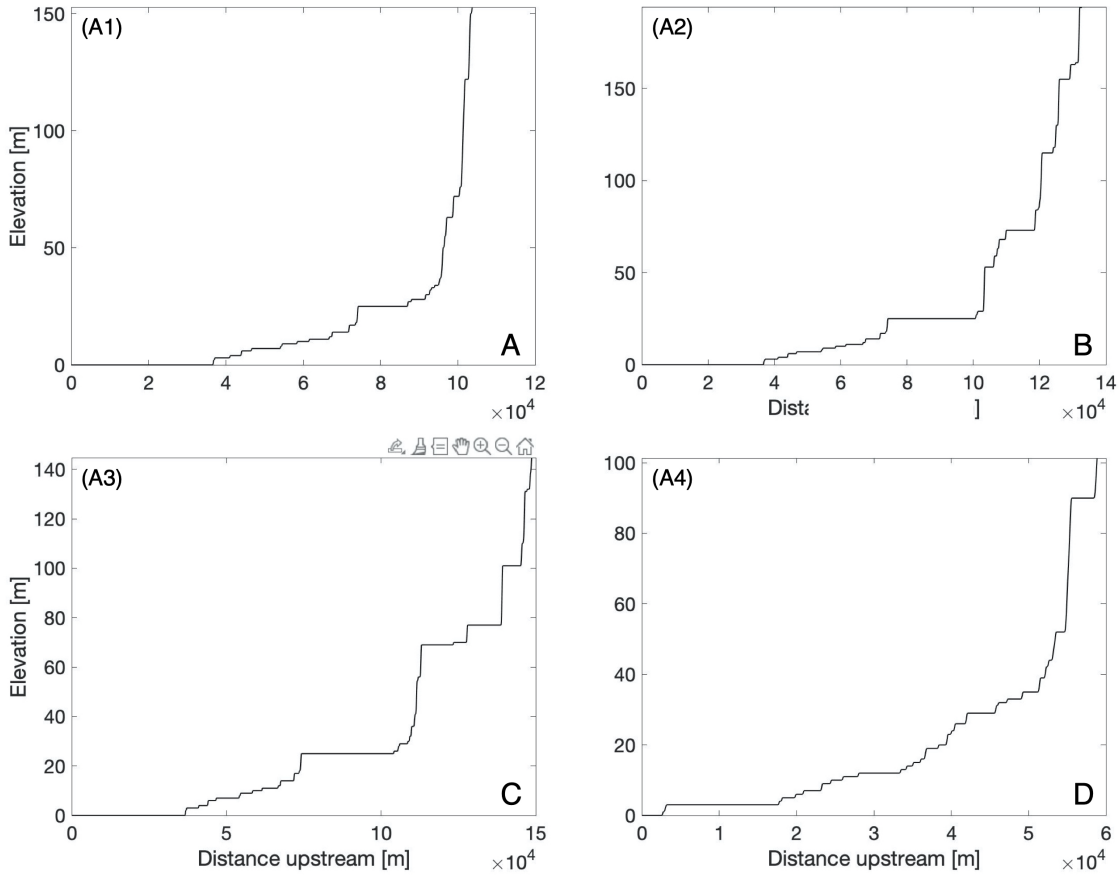

Figure 4.8: Fluvial profiles of Matamuhuri River tributaries. (a, b, c, d) The profiles of tributaries B1, B2, B3 and B4 specified on Figure 4.4b, respectively.

from the eastern fold location to the upstream region (Figure 4.13g-h). The shape of the antecedent stream profiles becomes approximately concave near the upstream end of the channel sections. However, the convex segments in the models beyond 200 kyr seem to get larger (Figure 4.13c-d, g-h). For the subsequent modeling periods (t_2, t_3 and t_4), individual models provide different results and are explained in more detail in the following sections.

Model A (sequential propagation)

In this section, we describe the results during three modeling periods (t_2, t_3, t_4) of Model A. During t_2, as the middle antiform starts rising, the older eastern fold stops uplifting. In the early period, i.e. 25 kyr, after the middle antiform starts to form, we observe the knickpoints on the antecedent stream profiles at the middle fold location (Figure 4.14a, e). Over time, these knickpoints become smoother similar to the evolution of the streams observed during t_1

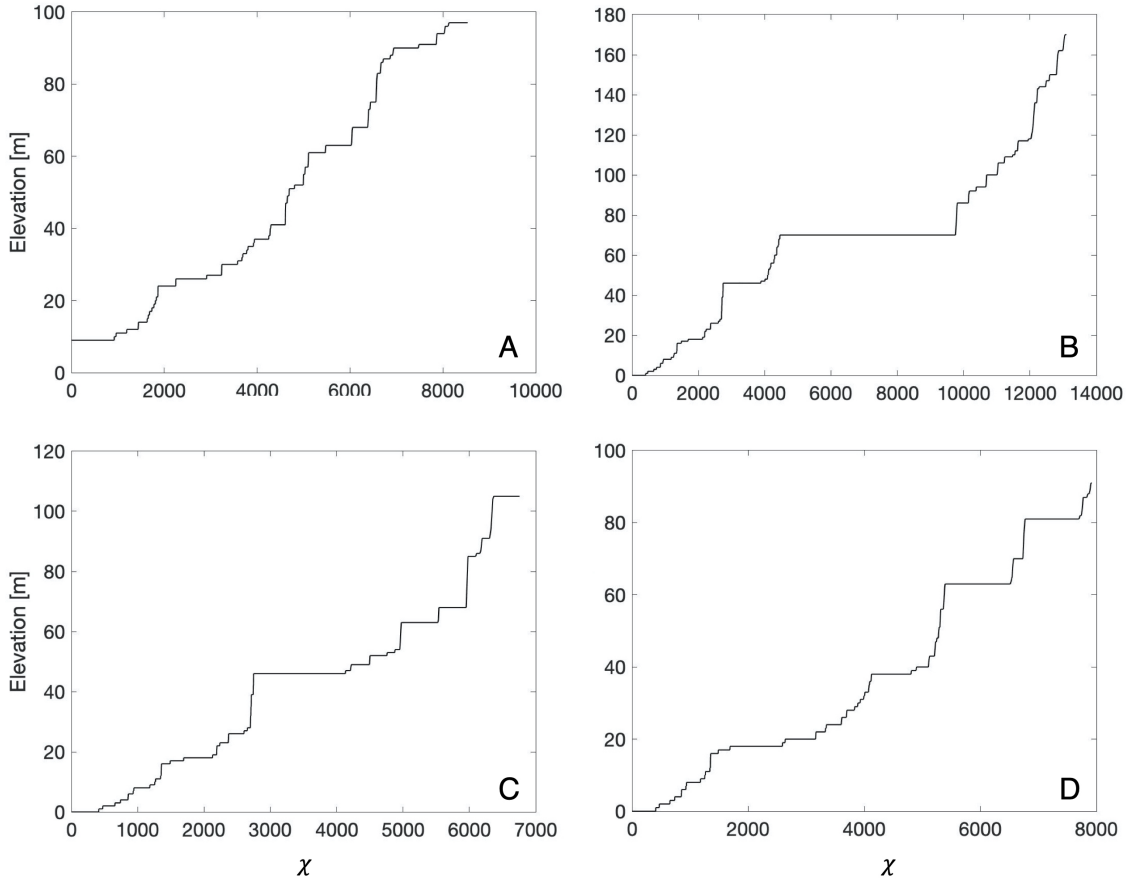

Figure 4.9: Elevation-χ plots of Feni River tributaries. (a, b, c, d) The Elevation-χ plots of tributaries A1, A2, A3 and A4 specified on Figure 4.3a, respectively.

(Figure 4.13). There are also knickpoints upstream, which are the ones that originate at the eastern fold location and have migrated upward. Similar to t_1, over 100 kyr, the knickpoint migration causes the expansion of the convex segments upstream, generating two major convex portions on the antecedent stream profiles (Figure 4.14b, f). Overall, the knickpoints at the active middle fold location are steepest compared to the other segments along the fluvial profiles. During t_3, the results are similar to those of t_2, but on the antecedent stream profiles, we observe the knickpoints closer to the outlet, where the youngest western fold starts to rise (Figure 4.14c-d, g-h). Similar to t_2, there are two major convex segments. Since only the western antiform uplifts during t_3, the antecedent stream profiles at this location show steeper knickpoints than the other sections. Lastly, during t_4, all knickpoints migrate upstream, and the profiles become more even over time (Figure 4.15). At 500 kyr after the western antiform stops rising, the stream profiles return to the concave shape indicating equilibrium state (Figure 4.15h).

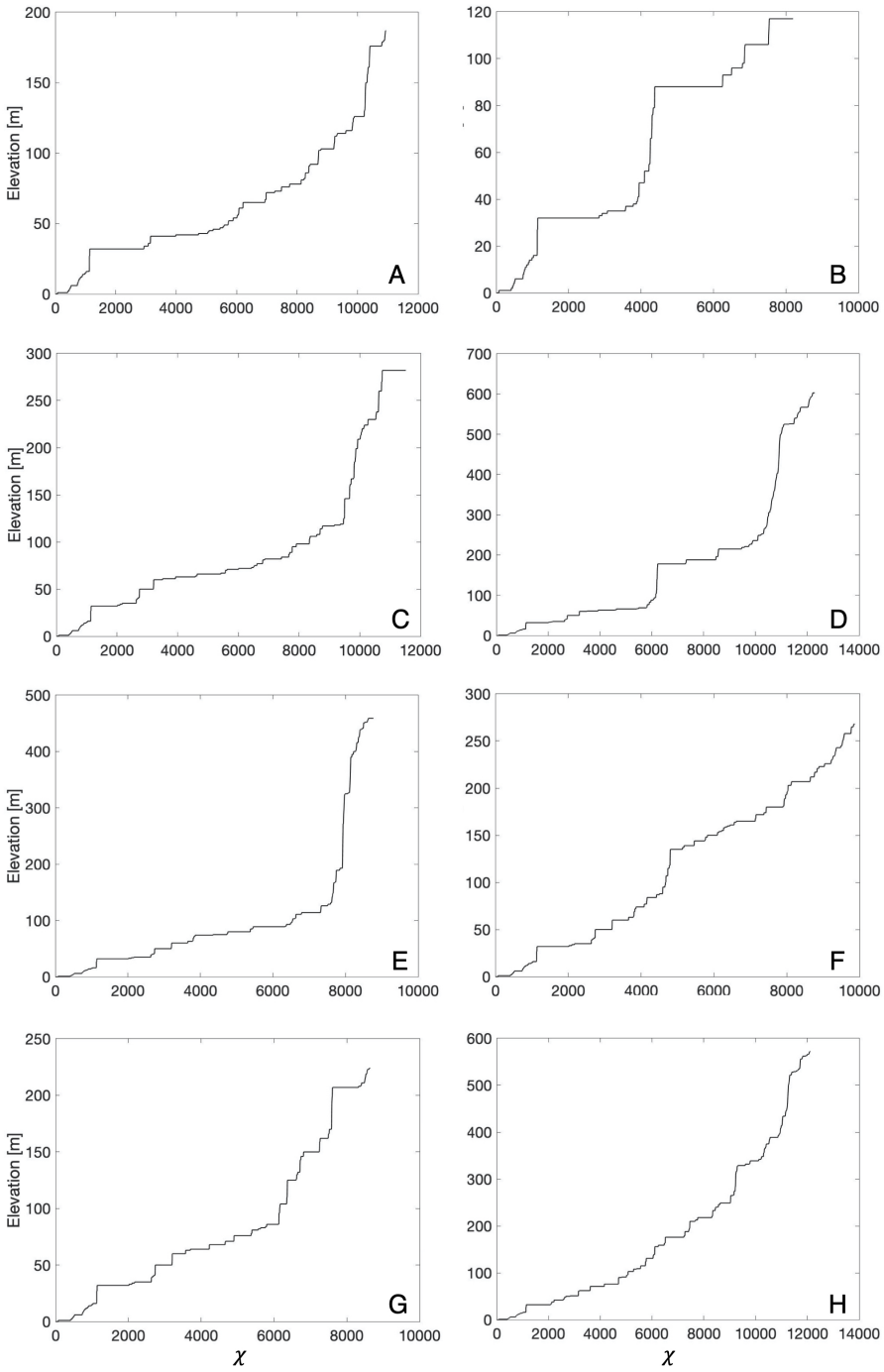

Figure 4.10: Elevation-χ plots of Karnaphuli River tributaries. (a, b, c, d, e, f, g, h) The Elevation-χ plots of tributaries B1-8 specified on Figure 4.3b, respectively.

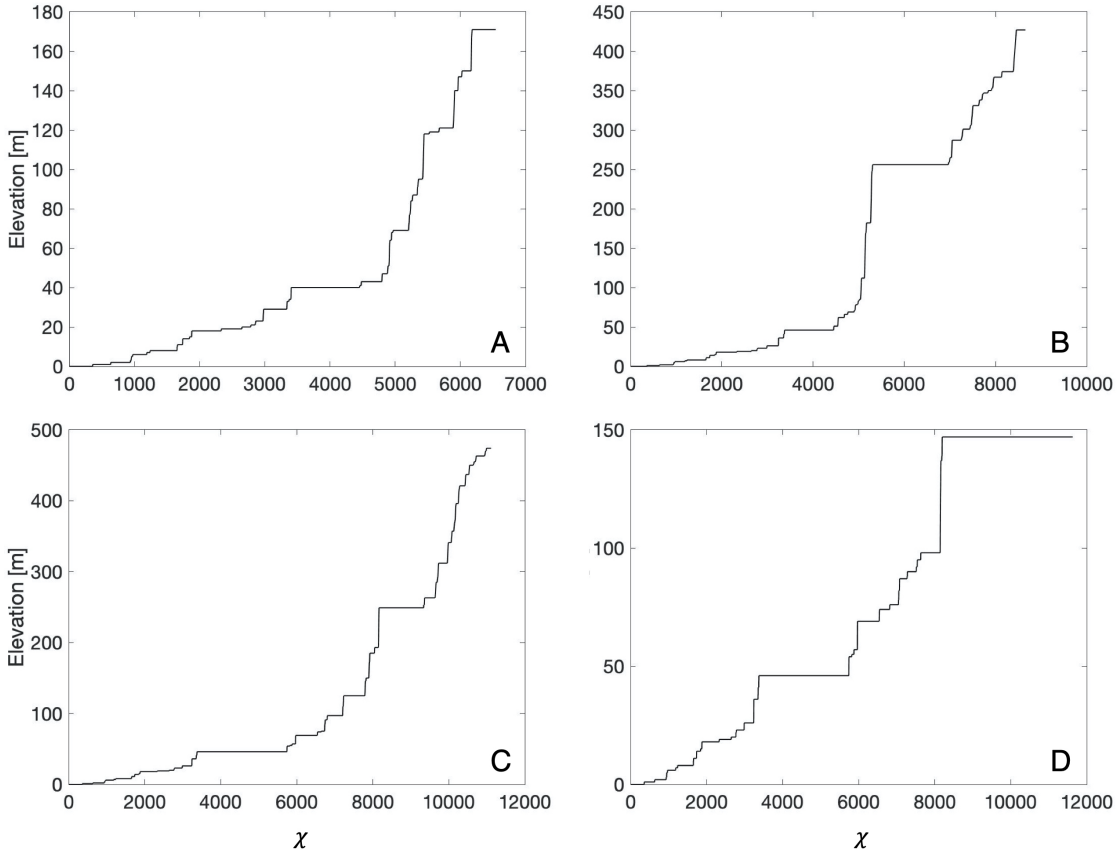

Figure 4.11: Elevation-χ plots of Sangu River tributaries. (a, b, c, d) The Elevation-χ plots of tributaries A1, A2, A3 and A4 specified on Figure 4.4a, respectively.

Model B (sequential propagation with partial reactivation)

We illustrate the output of Model B during three modeling periods (t_2, t_3, t_4). In the course of t_2, the stream profiles of the antecedent rivers grow smoother over time. However, there are still knickpoints at the locations of the middle and eastern antiforms (Figure 4.16a, b). The upstream segments of the antecedent channels are less concave and have higher elevation than those of the non-antecedent streams. Subsequently, during t_3, the migration of the knickpoints starts to take place. At around 100 kyr after the eastern fold stops uplifting, there is no knickpoint observed at the locations where the streams cross the eastern antiform (Figure 4.16c, g). However, at 150 kyr, the knickpoints in the downstream area migrate upstream to the location of the eastern fold (Figure 4.16d, h). The slope-break sections (knickpoint locations) along the profiles at the eastern antiform are not as steep as those located at the middle and western folds. Lastly, during t_4, the changes in the antecedent stream profiles and knickpoint migration over time in Model B are similar to the results of

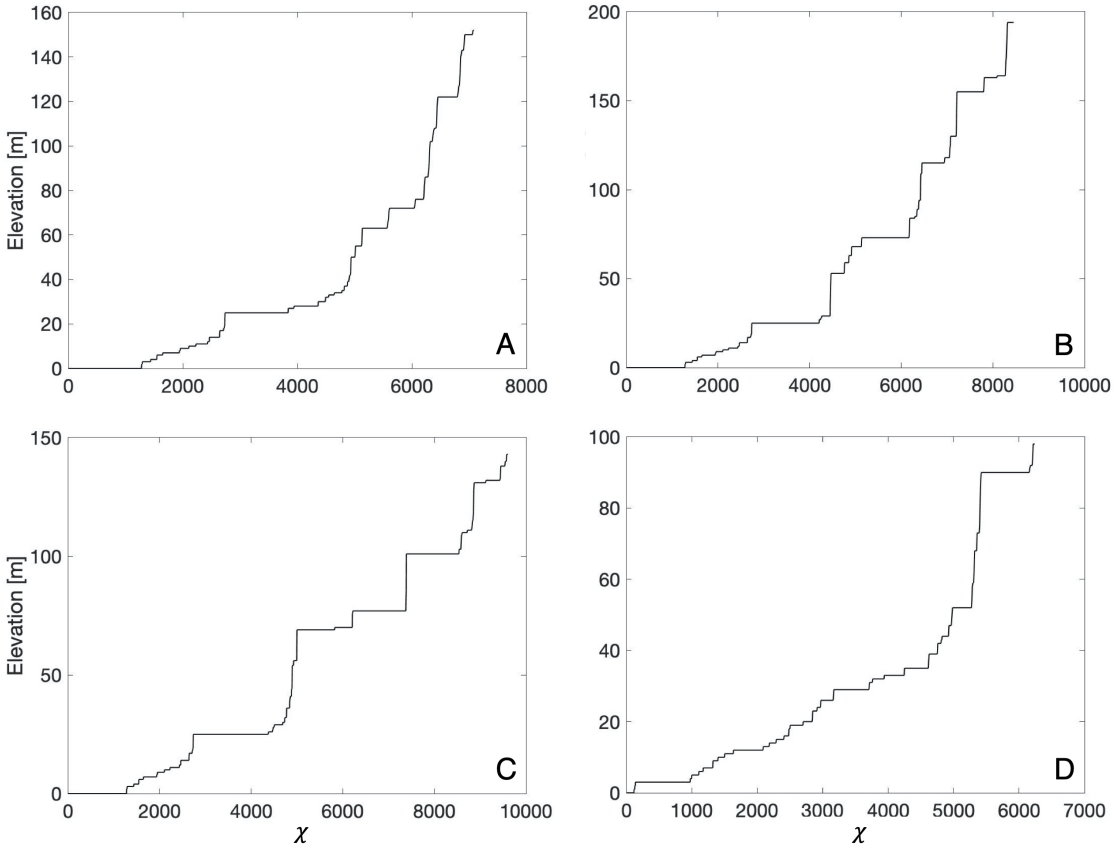

Figure 4.12: Elevation-χ plots of Matamuhuri River tributaries. (a, b, c, d) The Elevation-χ plots of tributaries B1, B2, B3 and B4 specified on Figure 4.4b, respectively.

Model A (Figure 4.17).

Model C (sequential propagation with continuous reactivation)

Figure 4.18 shows the results of three modeling periods (t_2, t_3, t_4) of Model C. During t_2, the results are similar to those of Model B. However, the elevations in the upstream segments of the antecedent channels are higher than the Model B results (Figure 4.18a-b, e-f). During t_3, we observe three knickpoints on each antecedent stream profile (Figure 4.18c-d, g-h). Each of these knickpoints is located at the active antiform locations. Moreover, the overall elevation of the antecedent streams crossing the anticline are greater than (1) the Model C streams that do not cross the antiforms and (2) the antecedent streams of Models A and B. Subsequently, during t_4, the results are similar to the previous models (Models A and B, Figure 4.19), the stream profiles become more even and concave while the knickpoints migrate upstream over time.

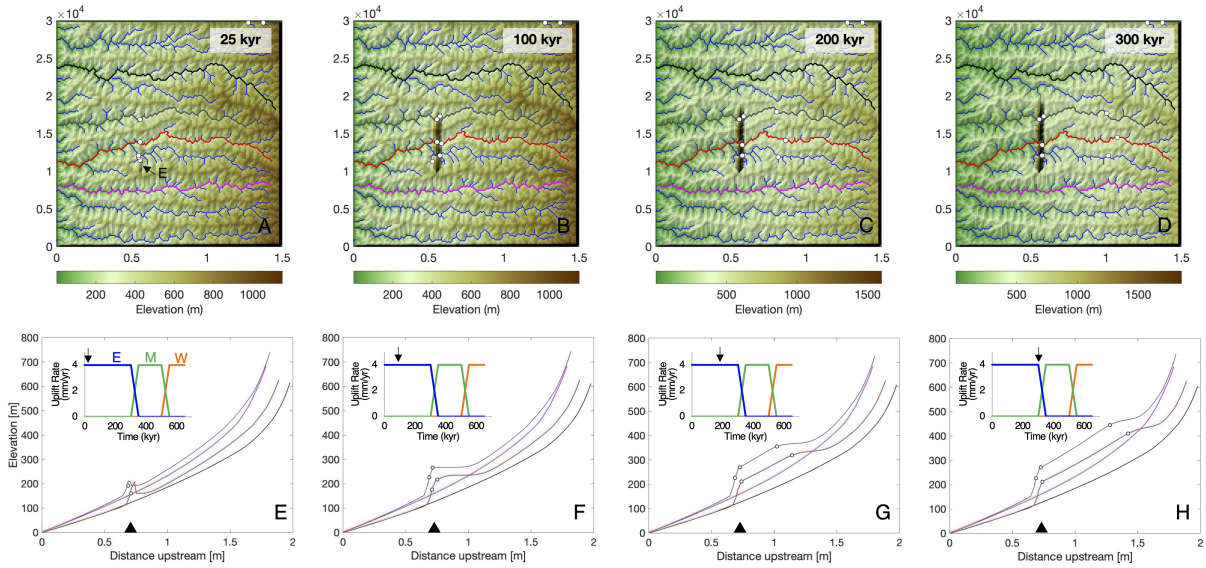

Figure 4.13: Surface dynamics modeling results during t_1 of Models A – C (see Tables 4.2 4.3). (a, b, c, d) The elevation maps show the eastern antiform evolves for 25, 100, 200 and 300 kyr, respectively, since it starts rising. (e, f, g, h) The fluvial profiles of sampled streams at 25, 100, 200 and 300 kyr, respectively, since the eastern antiform initiates. The blue lines are streams that are not selected for fluvial profile analysis. The red and gray lines are the antecedent rivers that cross the antiform, while the pink and black lines are streams that do not cross the antiform. The white circles with black perimeter on all maps and fluvial profiles represent knickpoints. The black triangles on the profiles represent the antiform locations. The inset plots in (e, f, g, h) show the vertical uplift rates over time of three folds (western fold [W] = orange, middle fold [M] = green, and eastern fold [E] = blue). The black arrows in the inset plots indicate the modeling periods. Note that all subsequent models will be annotated with the same symbology.

Model D (synchronous thrusting)

In Figure 4.20, we show the modeling results with all three antiforms concurrently growing for 650 kyr (t_1 + t_2 +t_3). In this case, the results are fairly similar to those of Model C. However, over time, around the east of the eastern antiform (upstream region), the antecedent stream profiles have greater elevations, and their shape becomes straight rather than concave, i.e. 650 kyr (Figure 4.20). During t_4, the solutions are similar to the other three models (Figure 4.21).

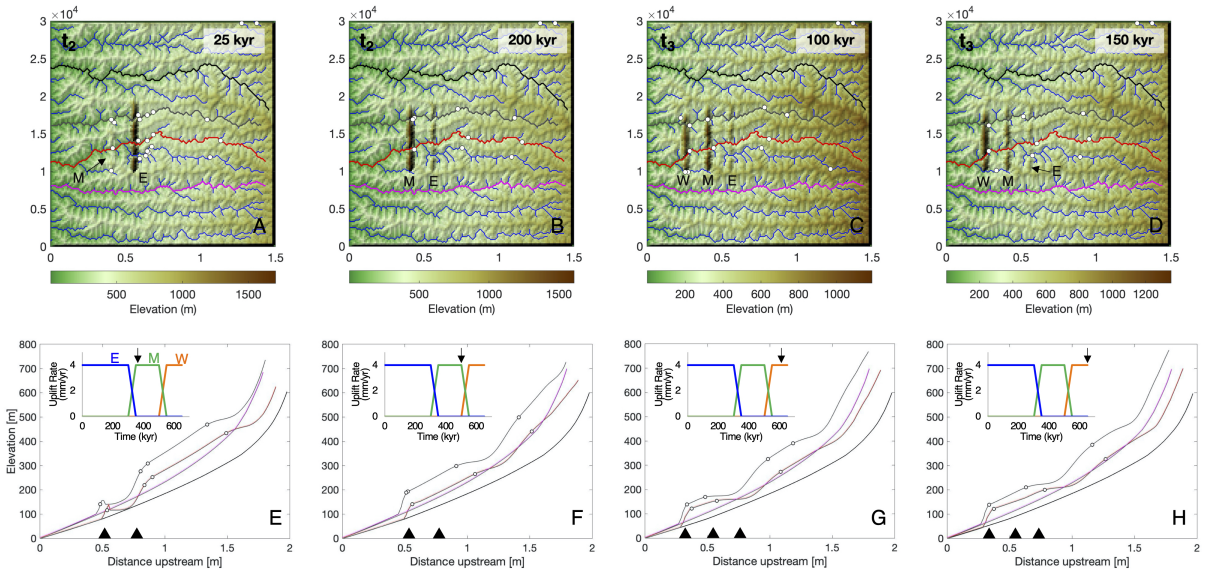

Figure 4.14: Surface dynamics modeling results during t_2 and t_3 of Model A. (a, b) The elevation maps show the evolving landscape as the middle antiform rises for 25 and 200 kyr, respectively (t_2). (c, d) The elevation maps show the western antiform evolves for 100 and 150 kyr, respectively (t_3). (e, f) The fluvial profiles of sampled streams at 25 and 200 kyr, respectively, since the middle antiform initiates (t_2). (g, h) The fluvial profiles of sampled streams at 100 and 150 kyr, respectively, since the western antiform starts uplifting (t_3). Model annotations as in Figure 4.13.

4.6 Discussion

We first summarize our observations and interpretation of active tectonics in the western IBR, then discuss the differences between the model results, and compare the modeled results to the observed stream profiles of the four outer-belt IBR rivers. We then compare our geomorphological results with kinematic and numerical models of the outer belt structures to explore possible physical explanations for the observed stream profiles and discuss the significance of our findings in the context of the active tectonics of the IBR. Lastly, we comment on the limitations of our simple surface dynamics models.

Fluvial profiles, knickpoints and tectonics across the western IBR

We selected 20 tributaries of four rivers to analyze their fluvial profiles and determine knickpoint location. All selected stream profiles include slope-break knickpoints and a few vertical-step knickpoints. These results are obtained by examining the fluvial profiles and elevation-χ plots, which is another method to examine the slope-area relationship within a

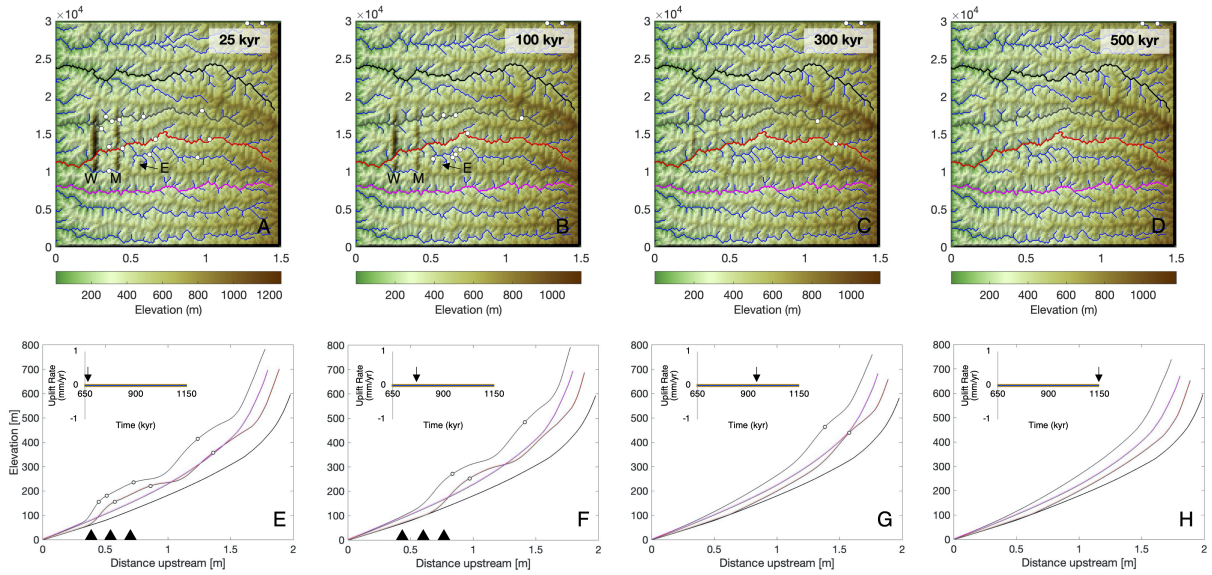

Figure 4.15: Surface dynamics modeling results during t_4 of Model A. (a, b, c, d) The elevation maps show the landscape evolving for 25, 100, 300 and 500 kyr, respectively, since the western antiform becomes tectonically inactive. (e, f, g, h) The fluvial profiles of sampled streams at 25, 100, 300 and 500 kyr, respectively, since the western antiform stops uplifting. Model annotations as in Figure 4.13.

river network and to determine types and locations of knickpoints (Gailleton et al., 2019; Whipple et al., 2017, 2013; Figures 4.5 - 4.12). The slope-break knickpoints indicate sudden changes in slope along the river caused by an increase in tectonic uplift rates. This type of knickpoint denotes differences in steepness index values of the segments above and below the knickpoint. On the other hand, so-called vertical-step knickpoints represent a relatively abrupt change in elevation (Gailleton et al., 2019; Neely et al., 2017; Whipple et al., 2013; Haviv et al., 2010). The steepness index values of the segments above and below a vertical-step knickpoint are similar, but the index is higher at the knickpoint location (a local increase in the steepness index, i.e., Whipple et al., 2013). In our studied watersheds, the vertical-step knickpoints are located downstream from the Kaptai Lake and floodplain locations (Figures 4.3, 4.5 and 4.6). On the other hand, the slope-break types are mostly located at the antiform-crossing sites and in higher-elevation regions (Figures 4.3 and 4.4). This suggests that the antiforms in our study region are actively uplifting. In addition, between individual knickpoints on the profiles, the shape of the profiles is approximately concave (Figures 4.3 - 4.8), whereas the flat segments on the profiles reflect the dammed Kaptai lake and floodplains (Figures 4.3, 4.5 and 4.6). Accordingly, the analysis of the fluvial profiles and identification of knickpoint locations suggest that the eastern antiforms in the western IBR actively uplift even while there are younger folds forming in the west. It is likely that there is an out-of-sequence reactivation of

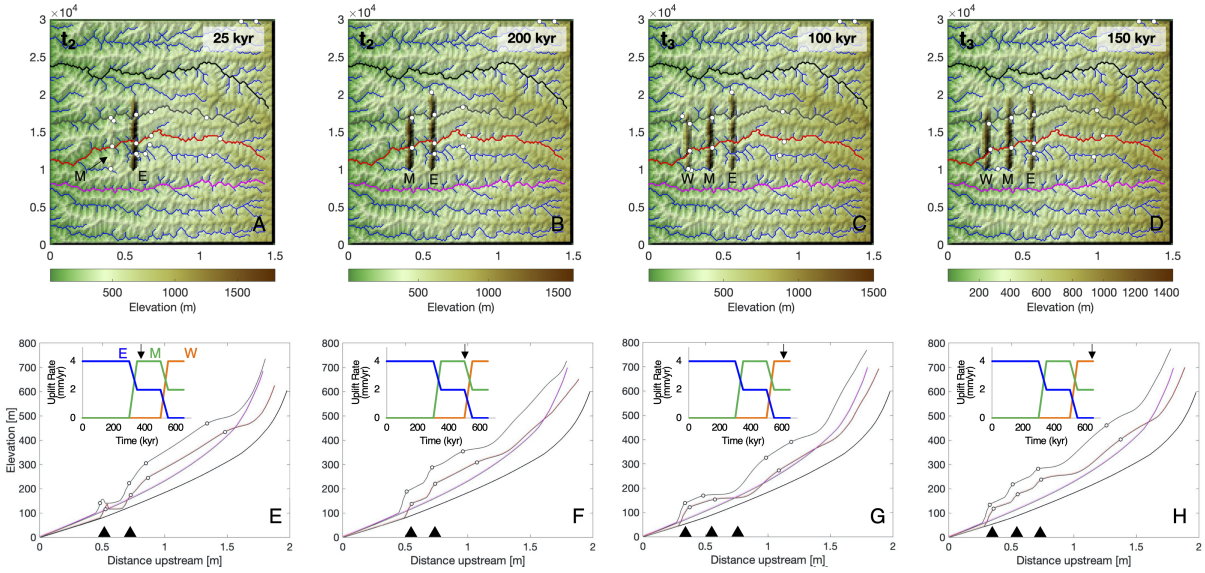

Figure 4.16: Surface dynamics modeling results during t_2 and t_3 of Model B. (a, b) The elevation maps show the middle antiform rises for 25 and 200 kyr, respectively, since it starts rising (t_2). (c, d) The elevation maps show the western antiform evolves for 100 and 150 kyr, respectively, since it starts uplifting (t_3). (e, f) The fluvial profiles of sampled streams at 25 and 200 kyr, respectively, since the middle antiform initiates (t_2). (g, h) The fluvial profiles of sampled streams at 100 and 150 kyr, respectively, since the western antiform starts uplifting (t_3). Model annotations as in Figure 4.13.

older eastern antiforms in the outer belt of the IBR.

Comparison between the results of the models

Here, we mainly focus on the t_2 and t_3 periods since the results of the other modeling periods (t_0, t_1, t_4) are similar. Also, for t_2, we compare Models A - C, because the Model D scenario is set up differently from the other three models. However, for t_3, we discuss and compare the results of all models.

During t_2, after the middle fold starts to rise and evolves for 200 kyr, there is one major slope-break knickpoint observed on each antecedent stream profile of Model A (sequential propagation). This is different from the results of Models B (sequential propagation with partial reactivation) and C (sequential propagation with continuous reactivation) since in these models, there are two major slope-break knickpoints (Figures 4.14f, 4.16f, 4.18f). This is because in Model A, the middle fold actively uplifts while the eastern antiform stops rising. This scenario is distinct from the other two models in which both the eastern and middle folds are actively uplifting during t_2. In addition, the results of Models B and C are quite

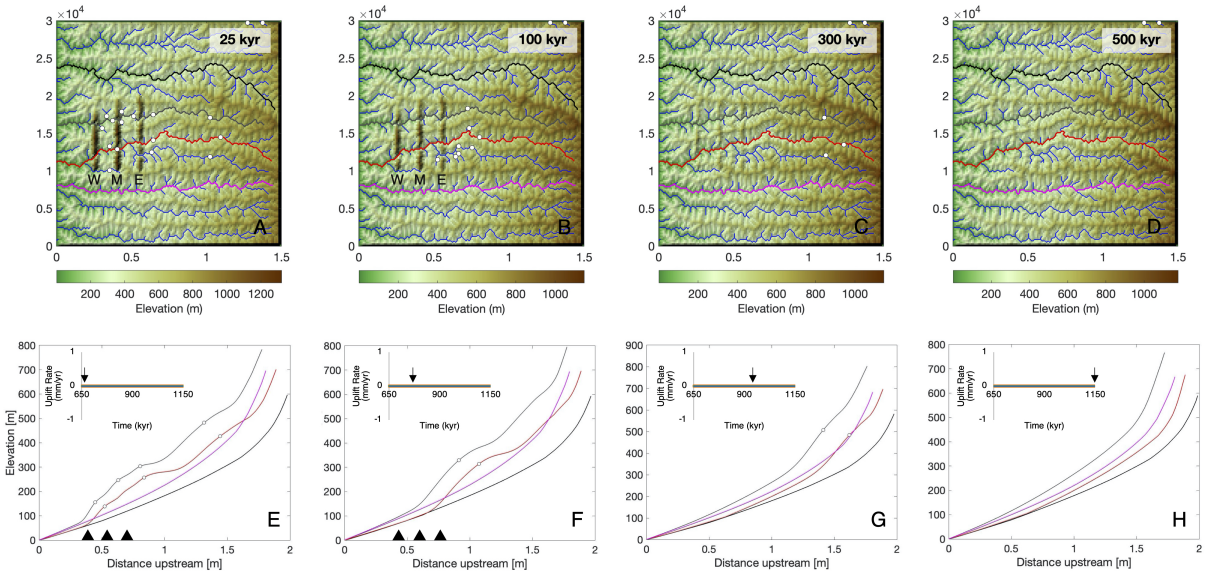

Figure 4.17: Surface dynamics modeling results during t_4 (after fold growth stops) of Model B (sequential propagation with partial reactivation). (a, b, c, d) The elevation maps show the landscape evolves for 25, 100, 300 and 500 kyr, respectively, since the western antiform stops uplifting. (e, f, g, h) The fluvial profiles of sampled streams during 25, 100, 300 and 500 kyr, respectively, since the western antiform stops uplifting. Model annotations as in Figure 4.13.

similar, but the elevation of the Model C antecedent stream segments at the antiform-crossing locations is higher than those of Model B. The knickpoints observed on the Model C profiles are also steeper than the ones of Models A and B. This is likely because the western and middle folds in Model C have greater vertical uplift rates than in the other two models. Additionally, to the east of the eastern antiform, the antecedent stream profiles of Models A - C have similar, slightly concave shapes.

During t_3, at 150 kyr since the western fold started to form (Models A - C) and 650 kyr since all three folds concurrently initiated (Model D), we find that for Models B – D, there are three major slope-break knickpoints along the antecedent stream profiles. These knickpoints indicate the locations where the channels cross the actively uplifting folds (Figures 4.16h, 4.18h, 4.20h). On the stream profiles of Model B, the knickpoints located at the eastern antiform are less steep than those from Models C and D. This is because for Model B, the eastern fold stops uplifting during this study period. Additionally, to the east of the eastern antiform, the stream profiles of Models A - C have a fairly similar shape (Figures 4.16h, 4.18h, 4.20h). Their shapes are slightly convex, which is possibly due to the knickpoint migration upstream from the fold, and then become concave upward. However, by only considering the convex segments, the degree of convexity of the stream portions seems to decrease when there are more actively uplifting folds in the model. The convexity of the Model A stream profiles

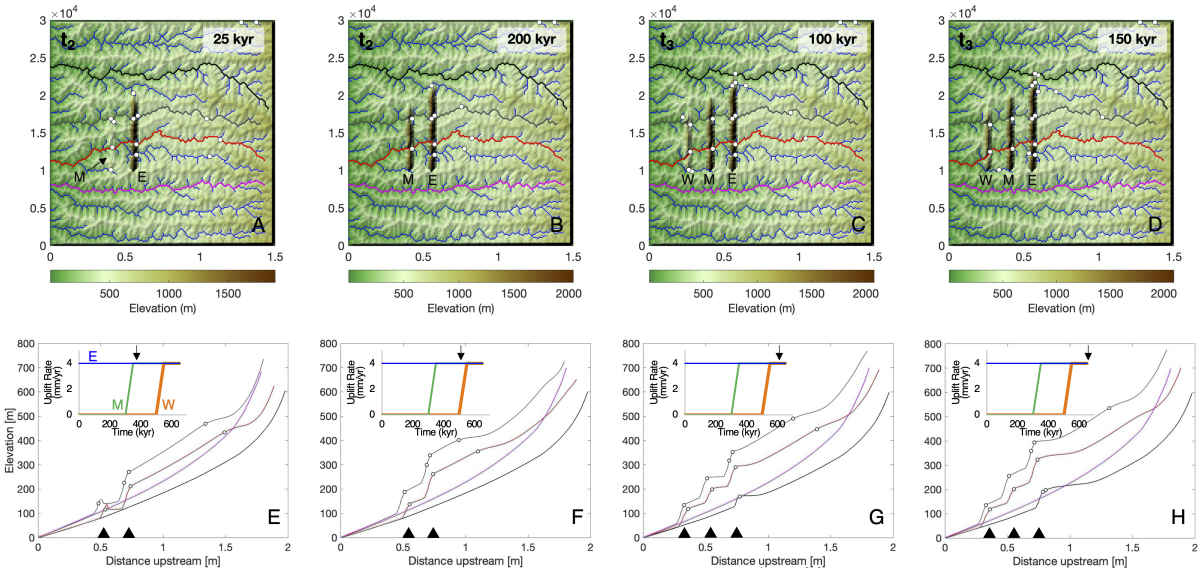

Figure 4.18: Surface dynamics modeling results during t_2 and t_3 of Model C. (a, b) The elevation maps show the middle antiform evolves for 25 and 200 kyr, respectively, since it starts rising (t_2). (c, d) The elevation maps show the western antiform evolves for 100 and 150 kyr, respectively, since it starts uplifting (t_3). (e, f) The fluvial profiles of sampled streams at 25 and 200 kyr, respectively, since the middle antiform initiates (t_2). (g, h) The fluvial profiles of sampled streams at 100 and 150 kyr, respectively, since the western antiform starts uplifting (t_3). Model annotations as in Figure 4.13.

is the greatest while it is the lowest in Model C (Figures 4.14g, h and 4.18g, h). It is possible that when there are more actively uplifting folds near the outlets, the river incision in the upstream of the antiforms near the outlet is affected. This also leads to greater surface uplift in the upper course regions of the Model C antecedent streams than those of Models A and B. Moreover, the upstream segments on the profiles of Model C (to the east of the eastern antiform) are different from those of Model D (synchronous thrusting), in that the Model D upstream profiles are straight with a steady slope. It is possible that when three folds start to form and evolve at the same time, the tectonic rock uplift greatly interrupts the erosion process in the downstream area. Since the erosion cannot keep up with the tectonic uplift, the upstream profiles are straight rather than concave in shape, unlike those of Model C.

Accordingly, the results from all models suggest that when there is an actively uplifting antiform in a region, a knickpoint is first created at that fold location and then propagates upstream over time. Also, as more slope-break knickpoints are produced in the downstream sections of the streams due to the rise of multiple antiforms, the formation of convex segments in the upstream areas becomes less likely.

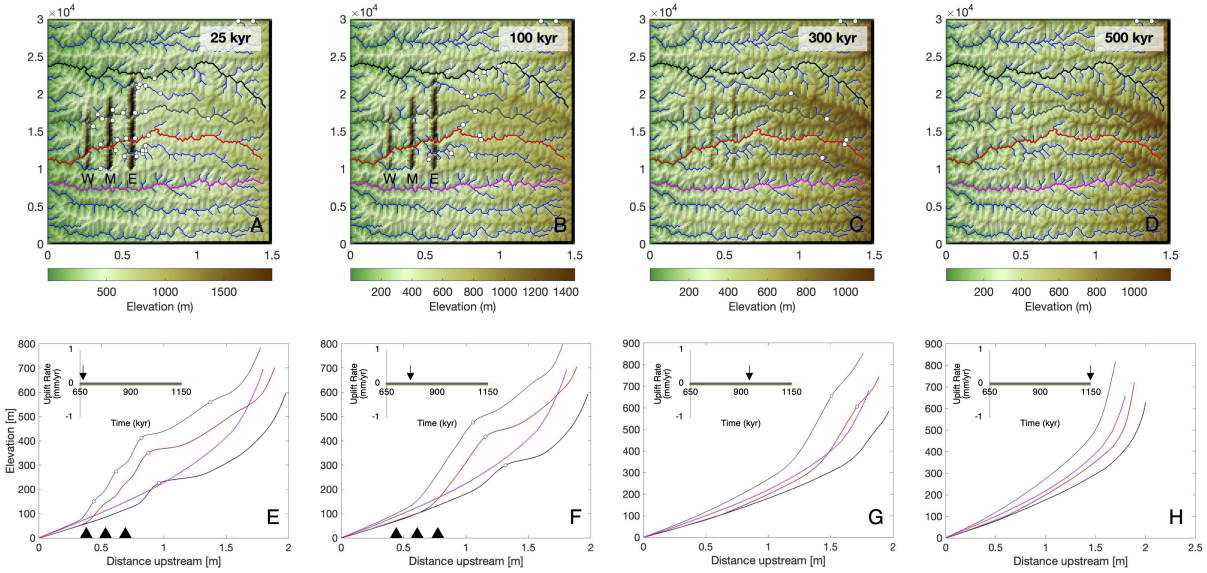

Figure 4.19: Surface dynamics modeling results during t_4 of Model C (sequential propagation with continuous reactivation). (a, b, c, d) The elevation maps showing the landscape evolves for 25, 100, 300 and 500 kyr, respectively, since the westernmost antiform becomes tectonically inactive. (e, f, g, h) The fluvial profiles of sampled streams during 25, 100, 300 and 500 kyr, respectively, since the westernmost antiform stops uplifting. Model annotations as in Figure 4.13.

Comparison between the modeled stream profiles and the western tributaries in the IBR

We note that the observed stream profiles in the IBR likely include some artifacts, in part due to the resolution limitations of the DEM. However, despite the lower resolution, the derived stream morphology indices of the 30 × 30m SRTM DEM and higher-resolution, 12 × 12m TanDEM-X data are quite similar to each other (Maneerat and Bürgmann, 2022). Some knickpoint locations on the modeled fluvial profiles are also expressed as bumps (i.e. Figures 4.14e and 4.-16e), and this is due to a grid sampling issue, similar to the DEM artifact problem. Overall, the shapes of the profiles extracted from the SRTM DEM and the locations of knickpoints allow for first-order comparisons with our modeling results.

By comparing the IBR observation with the Model A (sequential propagation) results, the fluvial profiles of the streams in the IBR are not similar to this model solution. We notice that the Model A profiles are convex to the east of the eastern antiform and become concave upstream (Figures 4.14). This characteristic is not observed on the profiles of the studied IBR channels. Moreover, we find multiple steep slope-break knickpoints on the IBR profiles but not on those of Model A (Figures 4.3, 4.4 and 4.14). There is one major slope-break

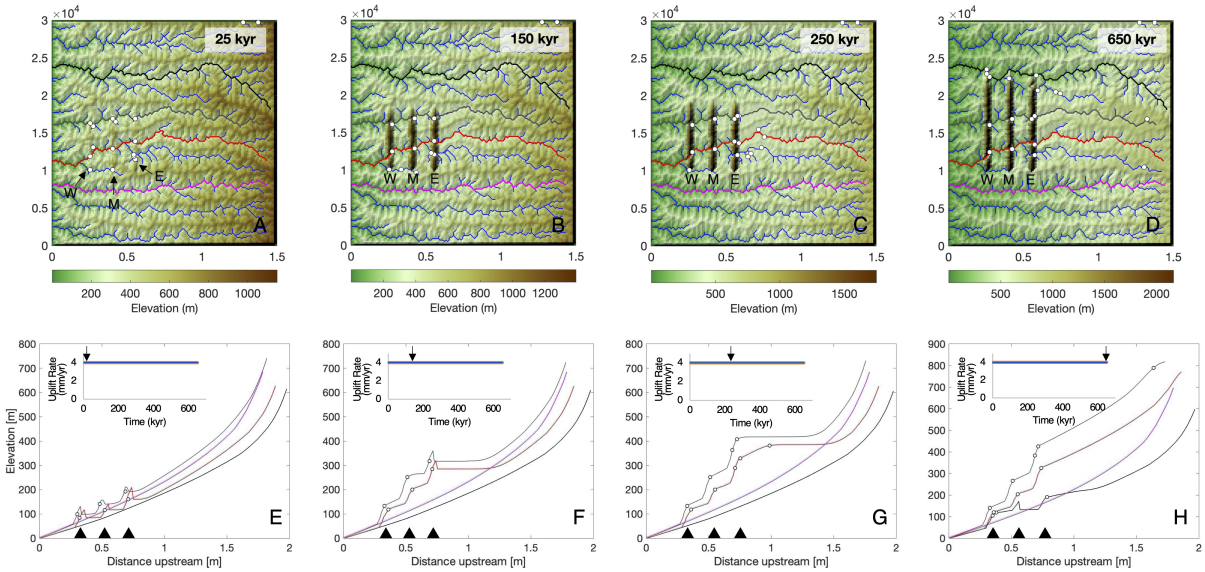

Figure 4.20: Surface dynamics modeling results during $t_1 + t_2 + t_3$ of Model D. (a, b, c, d) The elevation maps show all three antiforms evolve for 25, 150, 250 and 650 kyr, respectively, since they start rising. (e, f, g, h) The fluvial profiles of sampled streams at 25, 150, 250, and 650 kyr, respectively, since all three antiforms initiate. Model annotations as in Figure 4.13.

knickpoint on each Model A profile since we imposed one actively uplifting antiform at a time. This suggests that in the western IBR, even though the western fold starts to form, the older eastern antiform is still active.

The pattern and shape of the Model B (sequential propagation with partial reactivation) antecedent stream profiles are more similar to the observations in the IBR than those of Model A (Figure 4.16). However, the observed knickpoints are steeper than the Model B results. Similar to the Model A solution, the Model B fluvial profiles include convex segments to the east of the eastern antiform (upstream area) which are not observed in the IBR profiles. Overall, Model B still does not provide comparable results to the IBR observation.

The Model C (sequential propagation with continuous reactivation) results are fairly similar to the observed stream profiles in the IBR (Figure 4.18). The knickpoints are steeper than the ones of Models A and B and more comparable to the observed knickpoints. The observed slope-break knickpoints on the IBR profiles are located where the streams cross several antiforms (Figures 4.3 and 4.4) which is also seen in Model C. Additionally, the segments between the folds and the sections to the east of the eastern antiform in the model are concave in shape, similar to what is observed along several tributaries in the IBR (i.e. Figures 4.3, 4.4 and 4.22). This supports the scenario that as a western fold starts rising, the older eastern antiforms in the IBR also continue uplifting. Although thrust propagation in the outer belt of the IBR occurs sequentially, there is likely the out-of-sequence reactivation of

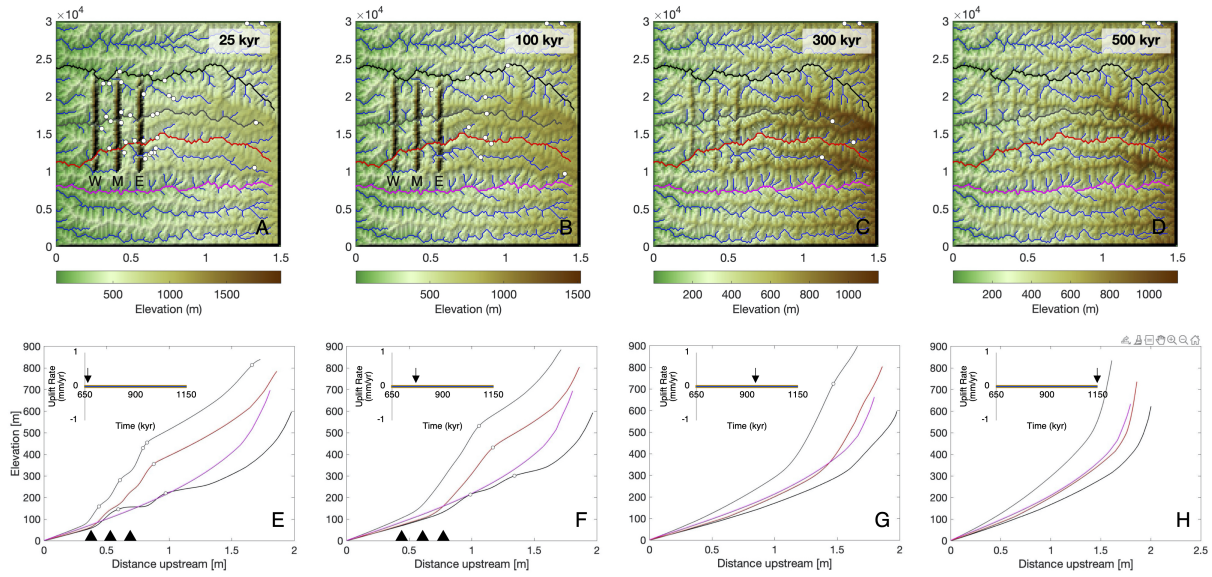

Figure 4.21: Surface dynamics modeling results during t_4 of Model D (synchronous thrusting). (a, b, c, d) The elevation maps showing the landscape evolves for 25, 100, 300 and 500 kyr, respectively, since the three antiforms become tectonically inactive. (e, f, g, h) The fluvial profiles of sampled streams during 25, 100, 300 and 500 kyr, respectively, since all three antiforms stop uplifting. Model annotations as in Figure 4.13.

older eastern antiforms. The result is also consistent with the pattern of cumulative shortening presented by Betka et al. (2018), which increases toward the east, suggesting continued activity of the eastern folds even as the deformation front has migrated westward.

When comparing the IBR observations and the Model D (synchronous thrusting) results, we find that the model solutions are also similar to some of the observed stream profiles. At 250 kyr after the three antiforms start to rise, the modeled profiles are similar to the tributaries that cross the westernmost antiforms (Figures 4.3, 4.4, 4.20g and 4.23). However, when we consider the modeling period later than 250 kyr, the shape of the modeled stream profiles diverges from the observed ones. For example, at 650 kyr, the upstream segments to the east of the eastern fold become straight with approximately steady gradients (Figure 4.20h). We do not observe such straight segments along the IBR stream profiles. Accordingly, it is likely that when several antiforms start rising concurrently, it hinders the downstream incision process leading to increases in the elevations of upstream areas. Since the erosion cannot keep pace with the tectonic rock uplift, the antecedent stream profiles are not concave in shape. Overall, we cannot rule out the fact that some of the westernmost, young folds in the IBR might have formed synchronously since at 250 kyr of Model D, the modeled antecedent stream profiles look similar to the observed ones.

During t_4, we find that all four model results do not resemble the observations in the

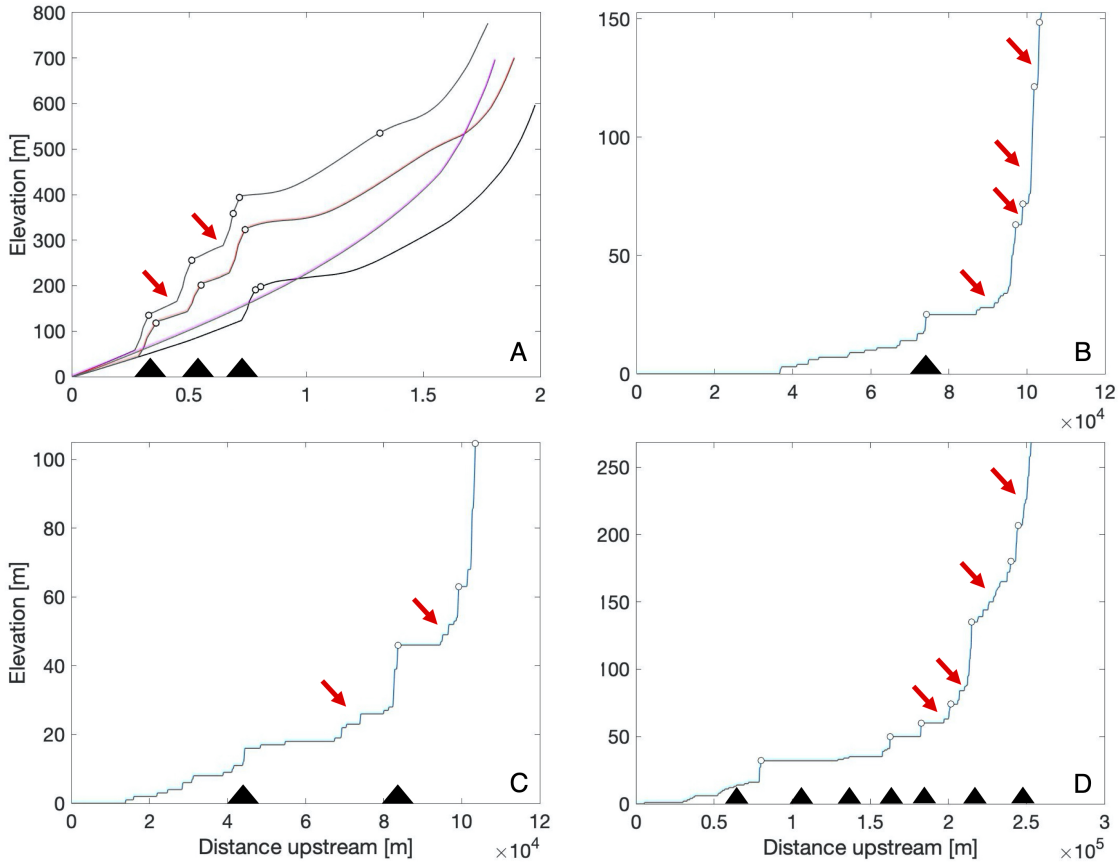

Figure 4.22: Comparison examples of actual IBR and the Model C stream profiles. (a) The stream profiles of Model C at 150 kyr since the westermost antiform starts rising. Three of the lines represent antecedent fluvial profiles while the pink one is a non-antecedent profile. (b) The Matamuhuri River tributary B1 profile specified on Figure 4.4a. (c) The Feni River tributary A3 defined on Figure 4.3a. (d) The Karnaphuli River tributary B6 specified on Figure 4.3b. The white circles with black perimeter represent knickpoints. The red arrows indicate concave segments between the knickpoints along the actual IBR stream profiles, as also observed in the modeled profiles (a). The black triangles represent antiform locations.

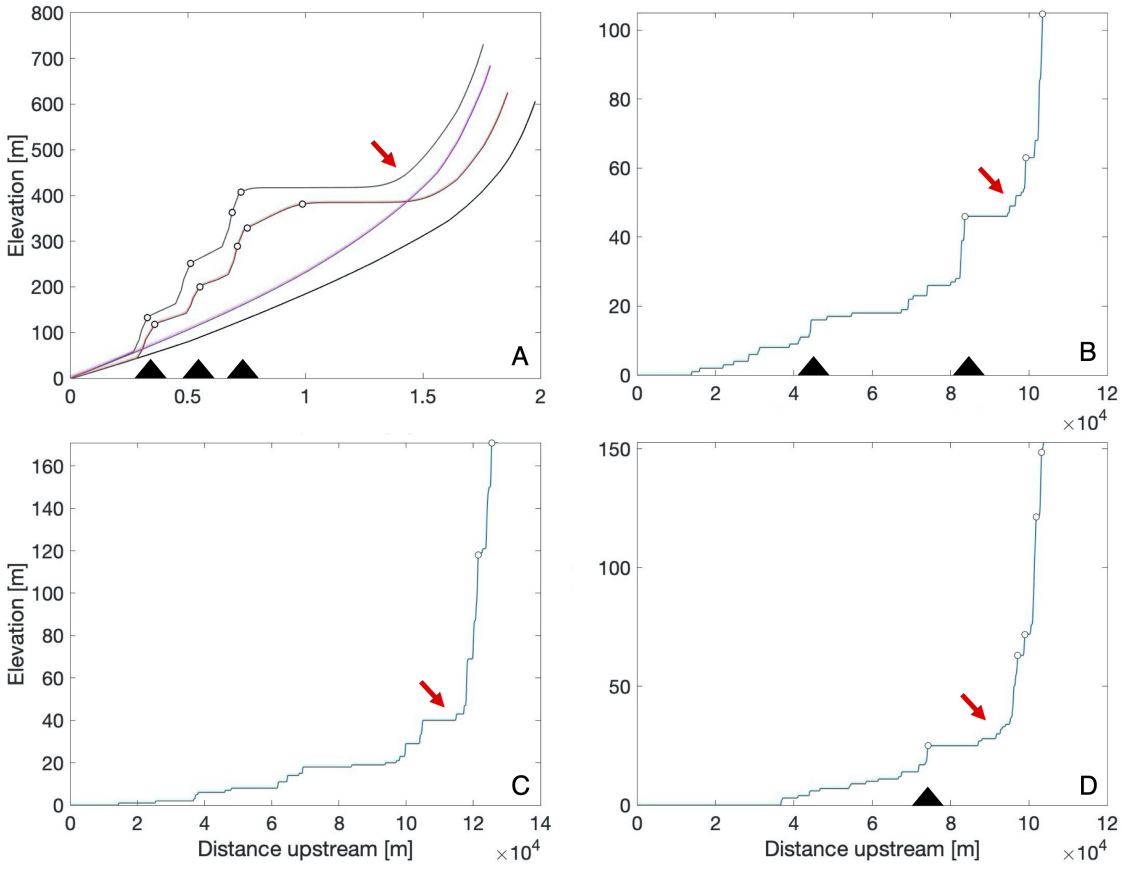

Figure 4.23: Comparison examples of actual IBR and the Model D stream profiles. (a) The stream profiles of Model D at 250 kyr since all three antiforms start rising. The gray and red lines represent antecedent fluvial profiles while the pink and black ones are non-antecedent profiles. (b) The Feni River tributary A3 profile specified on Figure 4.3a. (c) The Sangu River tributary A1 defined on Figure 4.4a. (d) The Matamuhuri River tributary B1 specified on Figure 4.4b. The white circles with black perimeter represent knickpoints. The profiles (b, c, d) contain steep slope breaks and then become concave upstream (indicated by red arrows) similar to the antecedent stream profiles of the modeled ones (a). The black triangles represent antiform locations.

IBR. As all the folds stop uplifting, we find that on the stream profiles of Models A - D, the knickpoints rapidly grow smoother within only ∼25 kyr, (i.e. Figures 4.15 and 4.17). We do not observe smooth knickpoints and multiple convex segments on the observed stream profiles in the IBR (i.e., Figure 4.3 and 4.4). This indicates that all the antiforms in the western IBR that the studied streams traverse actively uplift.

Accordingly, the Model C results during t_2 and t_3 periods are most comparable to the observed stream profiles and knickpoint locations in the western IBR while the Model D solution at 250 kyr is similar to some IBR streams crossing the westernmost antiforms (Figures 4.22 and 4.23). It is likely that while the western antiforms start rising, the old eastern folds are still tectonically active in the outer belt. Moreover, it is possible that some of the westernmost folds start to form concurrently. Overall, the antiforms within our study region in the IBR seem to continue rising.

Although stream convexities, as predicted by the fluvial profiles of Models A - C, are not observed in the upstream portions of the IBR profiles, they have been observed along fluvial profiles of other regions. Some profiles of streams draining the Argentera Massif in Stura Valley in northwestern Italy have convex segments, which have been attributed to several factors, including active faults and glacial erosion (Marrucci et al., 2018). Similarly, in the central High Atlas, some channels crossing the southern Atlas Fault, an active reverse fault, have convex segments on their profiles upstream of the fault (Boulton et al., 2014). Likewise, some major Himalayan rivers draining the Tibetan Plateau, such as the Sutlej, Bheri, Karnali, and Arun Rivers, also have convex segments on their fluvial profiles upstream of the main central thrust (Seeber and Gornitz, 1983). Accordingly, the occurrence of profile convexities in upstream region of streams is not an uncommon feature and indicates knickpoint migration suggesting active tectonics rock uplift of these regions. Although the antiforms in the outer belt of the IBR are likely active, we do not observe the convex segments on the IBR profiles. This is possibly because there are more rapid and large-scale uplifts in the example regions than the one in the IBR.

However, the modeled convex segment lengths of Models A - C in some modeling periods, i.e. at 300 kyr of t_1 and at 25 kyr of t_2, seem to be almost half of the entire stream lengths, and the profiles of segments between active antiform and upstream knickpoints are straight (Figures 4.14, 4.16 and 4.18). This is not observed in any of the previously mentioned examples. This feature is likely because of the high regional uplift rate imposed in the model (1 mm/yr). To further investigate this, we perform surface modeling of Model A at 300 kyr by varying the regional uplift rate to 0.5 and 0.1 mm/yr. The resultant profiles of the segments to the east of the active eastern antiform (between the eastern antiform and upstream knickpoint) become more concave than those of the 1-mm/yr model (Figure 4.24). By setting the regional uplift rate to relatively low values, e.g., 0.5 and 0.1 mm/yr, the results seem to be more comparable to other actively deforming regions mentioned previously. However, over several modeling periods the surrounding topographic elevations become much lower ($>$ 1000 m) than the active antiforms (Figure 4.24b, c). This rapid subsidence of the background topography occurs as the regional uplift rate is reduced. Because of this, in this study (Models A - D) we set the regional uplift rate to be relatively high in order to maintain background topography

over multiple modeling periods (preventing rapid erosion of background topography over time). The ad hoc choice of a regional uplift rate of 1 mm/yr is not uncommon for Landlab modeling, and other publications also used a similar range of rates (e.g., Reitman et al., 2019; Lyons et al., 2020). In addition, the antiform vertical uplift rate is also related to the regional uplift rate. By altering the regional uplift rate to 0.5 and 0.1 mm/yr and keeping the antiform uplift rate as 4 mm/yr, the modeled antecedent stream profiles change, thus becoming more concave in shape at the original locations of convex or straight segments (Figure 4.24). However, when we reduce both the regional and antiform vertical uplift rate to half of the original rates, the results are fairly similar to our original models (Figure 4.25).

Although we observe notable changes of fluvial profiles of the Model A - D results, we do not observe complete stream diversion around the rising antiform (Figures 4.13 - 4.20). Changes in stream flow directions can happen depending on the assigned rates of regional and antiform uplift. For example, as the regional uplift rate is reduced to 0.1 mm/yr and the antiform uplift rate remains the same (4 mm/yr), at 200 kyr of Model A t_2, the stream is deflected and flows around the middle antiform (Figure 4.26). These regional and antiform uplift parameters seem to be related and likely affect the modeling results. Accordingly, if we run the simulations with different regional and antiform uplift rates over various timescales, we obtain similar fluvial profile shapes. Given the lack of quantitative vertical uplift and erosion rate data, this study only provides qualitative results and explores the general relationship between these rates and topography evolution.

Mechanism for forward propagation and fault reactivation

Considering the surface and deeper structures of the outer belt, the very low wedge taper angle and bivergent antiforms (Betka et al., 2018) can facilitate out-of-sequence thrusting to occur in the western IBR. These observations of low surface slope and variation in thrust vergence also support a weak décollement in this region. Recently, Das et al. (2021) proposed that the viscous outer wedge allows for solely ductile deformation in the IBR outer fold and thrust belt. According to analog models (i.e. Costa and Vendeville, 2002), out-of-sequence and/or synchronous bivergent thrusting styles are favored to occur with a viscous detachment. Bivergent thrust propagation is also observed in the Niger Delta fold and thrust belt above a subhorizontal, overpressure shale décollement (Bilotti and Shaw, 2005). Corredor et al. (2005) document regions of the Niger Delta fold-thrust belt with both sequential propagation and out-of-sequence or synchronous thrusting which may be analogous to our observations in the outer belt of the IBR.

To evaluate mechanisms of out-of-sequence thrusting in the outer belt, we present a representative numerical model of fold-thrust belt evolution with a weak décollement using FLAC (Fast Lagrangian Analysis of Continua, Itasca, 2000; Cundall and Board, 1988), a finite difference numerical code. The model includes layers of relatively strong sedimentary rocks overlying a weak décollement horizon with a strong backstop. All of the model layers are prescribed a visco-elasto-plastic rheology (non-Newtonian, Mohr-Coulomb, Maxwell). The model incorporates syntectonic erosion and sedimentation. Figure 4.27 gives the general

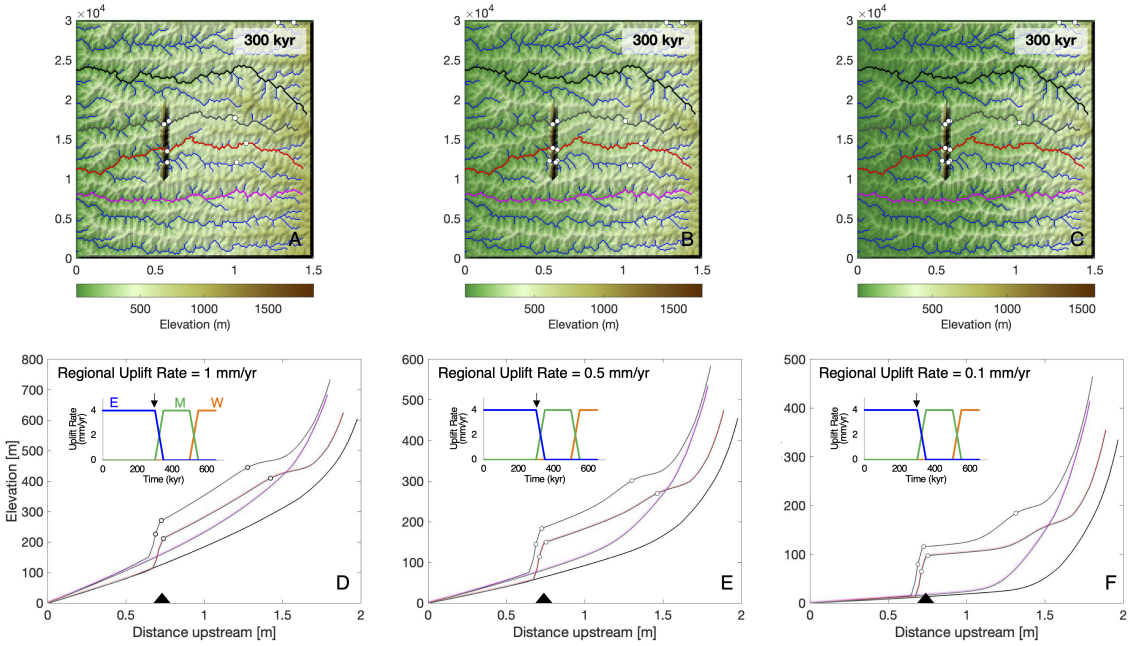

Figure 4.24: Surface dynamics modeling results during t_1 of Model A varying regional uplift rates from 1 mm/yr to 0.5 and 0.1 mm/yr. (a, b, c) The elevation maps showing the landscape evolves for 300 kyr since the eastern antiform starts rising, and the regional uplift rate is assigned to 1, 0.5 and 0.1 mm/yr, respectively. (d, e, f) The fluvial profiles of sampled streams during 300 kyr since the eastern antiform starts uplifting, and the regional uplift rate is assigned to 1, 0.5 and 0.1 mm/yr, respectively. Model annotations as in Figure 4.13.

configuration and boundary conditions of the model. Wedge top sediments have rheology parameters identical to layer 1. The numerical modeling results are shown in Figure 4.28. The strain rate map in Figure 4.28a shows that nearly all of the slip is localized along the frontal ramp during time step 111 after 2.775 Myr of convergence, after a new ramp has propagated to the foreland. The deviatoric-stress map shows stress localization where the ramp steps up from the décollement (Figure 4.28a). After an additional 225 kyr of convergence (Figure 4.28b), the ramp that initiated in Figure 4.28a has achieved its maximum slip and become inactive. During this time step (Figure 4.28b), the strain rate map shows reactivation of four older ramps and the stress map shows a delocalization of stress at the frontal ramp with more stress localization where the internal ramps step up from the décollement and are reactivated (Figure 4.28b). After an additional 8 model timesteps (200 kyr), the out-of-sequence thrusting stops, and a new ramp propagates in the foreland (Figure 4.28c). The model suggests periodic pulses of frontal ramp propagation (Figure 4.28a) followed by reactivation of internal thrusts. Fault of reactivation occurs when slip on the frontal ramp is arrested as the hanging wall builds topography, loading the frontal thrust (Figure 4.28b) and transmitting stress to the

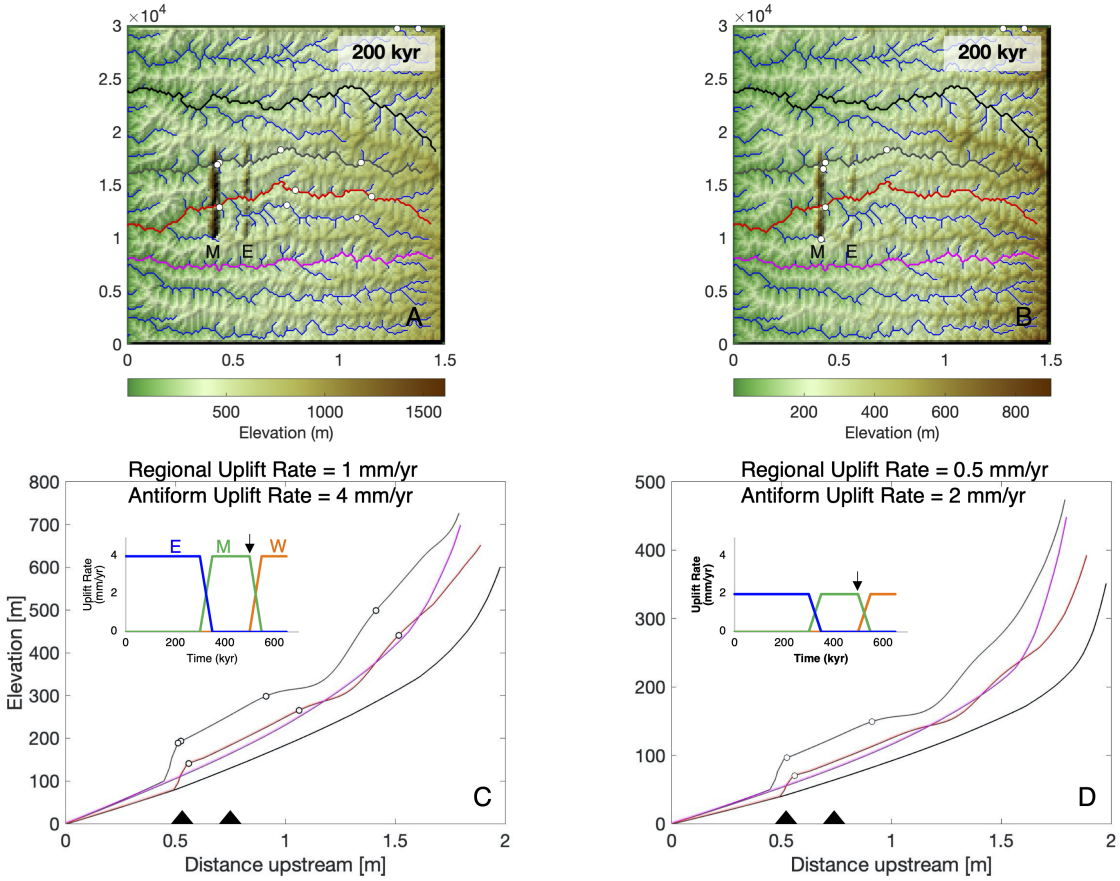

Figure 4.25: Surface dynamics modeling results during t_2 of Model A reducing the regional and antiform uplift rates by half of the original values. (a, b) The elevation maps showing the landscape evolves for 200 years after the middle antiform starts rising, and the regional uplift rate is assigned to 1 and 0.5 mm/yr, respectively, while the antiform uplift rate is set to 4 and 2 mm/yr, respectively. (c, d) The fluvial profiles of sampled streams during 200 kyr since the middle antiform starts uplifting, and the regional uplift rate is assigned to 1 and 0.5 mm/yr, respectively, while the antiform uplift rate is set to 4 and 2 mm/yr, respectively. Model annotations as in Figure 4.13

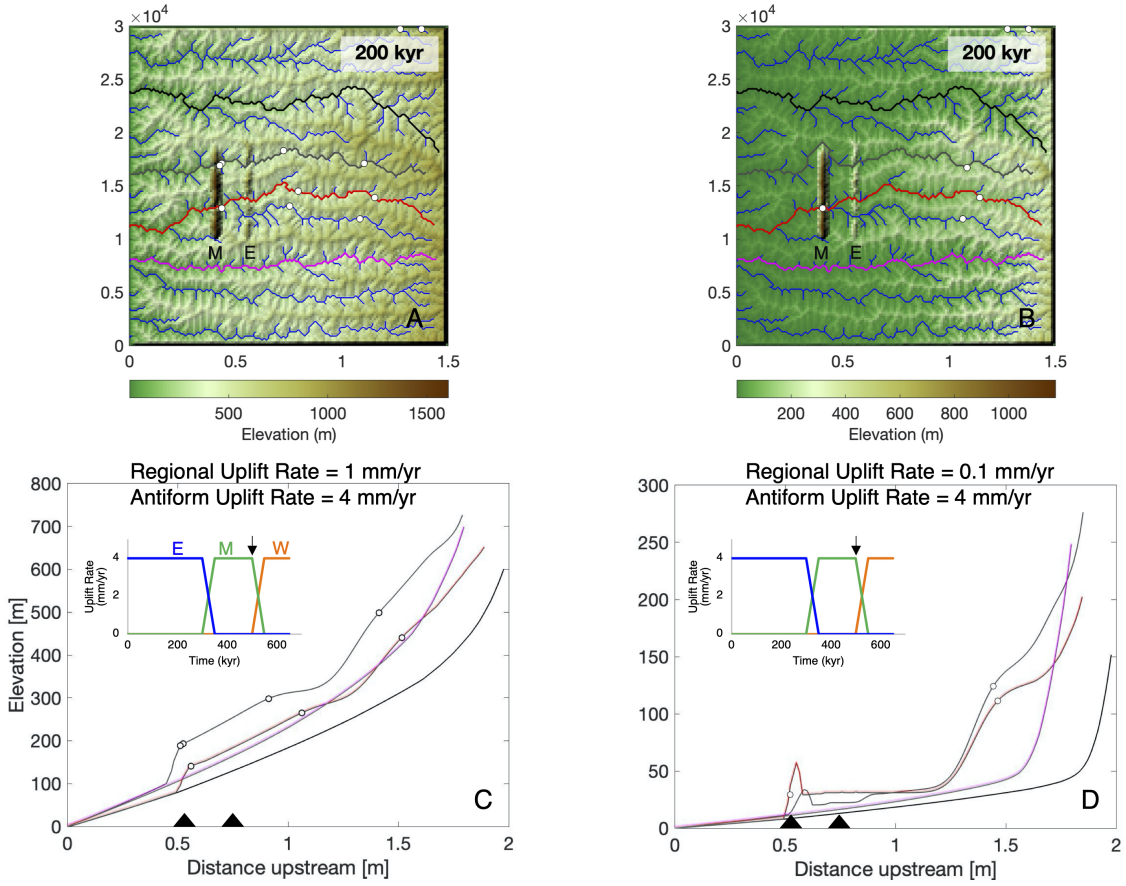

Figure 4.26: Surface dynamics modeling results during t_2 of Model A varying regional uplift rate from 1 to 0.1 mm/yr. (a, b) The elevation maps showing the landscape evolves for 200 years after the middle antiform starts rising, and the regional uplift rate is assigned to 1 and 0.1 mm/yr, respectively. (c, d) The fluvial profiles of sampled streams during 200 kyr since the middle antiform starts uplifting, and the regional uplift rate is assigned to 1 and 0.1 mm/yr, respectively. Model annotations as in Figure 4.13.

older structures. These results are consistent with our landscape dynamic models that indicate reactivation of eastern antiforms for the outer belt of the IBR. The models also suggest that earthquakes may alternately rupture to the frontal thrust or partially rupture one or more existing structures in the fold-thrust belt. In the numerical experiments, strain localization along the décollement horizon and fault reactivation requires a weak basal décollement layer, consistent with the predictions of critical taper theory and observations of elevated pore-fluid pressures in décollement horizons globally, including the IBR (Davis et al., 1983; Bilotti and Shaw, 2005; Zahid and Uddin, 2003).

Our results indicate active growth of the outer belt structures in the IBR, suggesting that the megathrust is active (Figure 4.29). However, it remains inconclusive whether the megathrust is likely to rupture all the way to the deformation front, and if subsidiary faults primarily fail with the entire megathrust or in independent events (Wang et al., 2014). Wang et al. (2014) consider that historical events, such as the 1964 Alaskan (i.e., Plafker, 1965) and 1762 Arakan earthquakes (i.e., Halsted, 1841; Wang et al., 2013), involved failures of the splay faults occurring together with the megathrust rupture. We suggest that it is likely that the out-of-sequence splay faults may cause more frequent, moderate earthquakes due to independent failures of the faults in the outer belt. Overall, the observed structures and evidence for a weak décollement support the scenarios of sequential propagation with continuous reactivation and/or synchronous thrust propagation in the outer belt of the IBR.

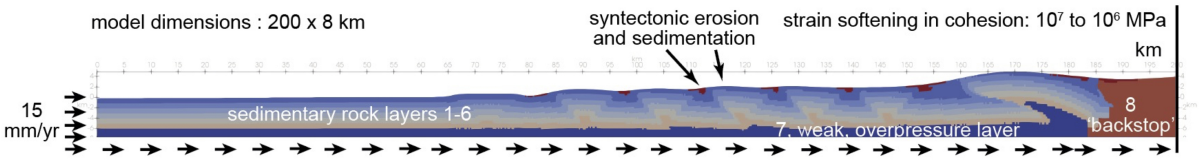

Figure 4.27: Model design for pilot study numerical experiments. The model grid spacing is 250 m, allowing four elements per kilometer. The left and lower boundary conditions are defined by a horizontal velocity of 15 mm/yr to the right, the right boundary is fixed horizontally, and the lower boundary is fixed vertically.

Model Limitation

Since our models only include three folds and represent very simple scenarios of the fold growth and evolution with time, they are not meant to provide results that perfectly match the observations in the IBR. Instead, we focus on first-order aspects of the evolution of antecedent stream profiles that we consider to be diagnostic of the synchronous growth of the anticlines. There are additional factors or parameters that we can include in future models, such as increasing the number of antiforms, building fold linkage scenarios, allowing for asymmetric fold morpology, imposing widening antiformal growth over time, assigning

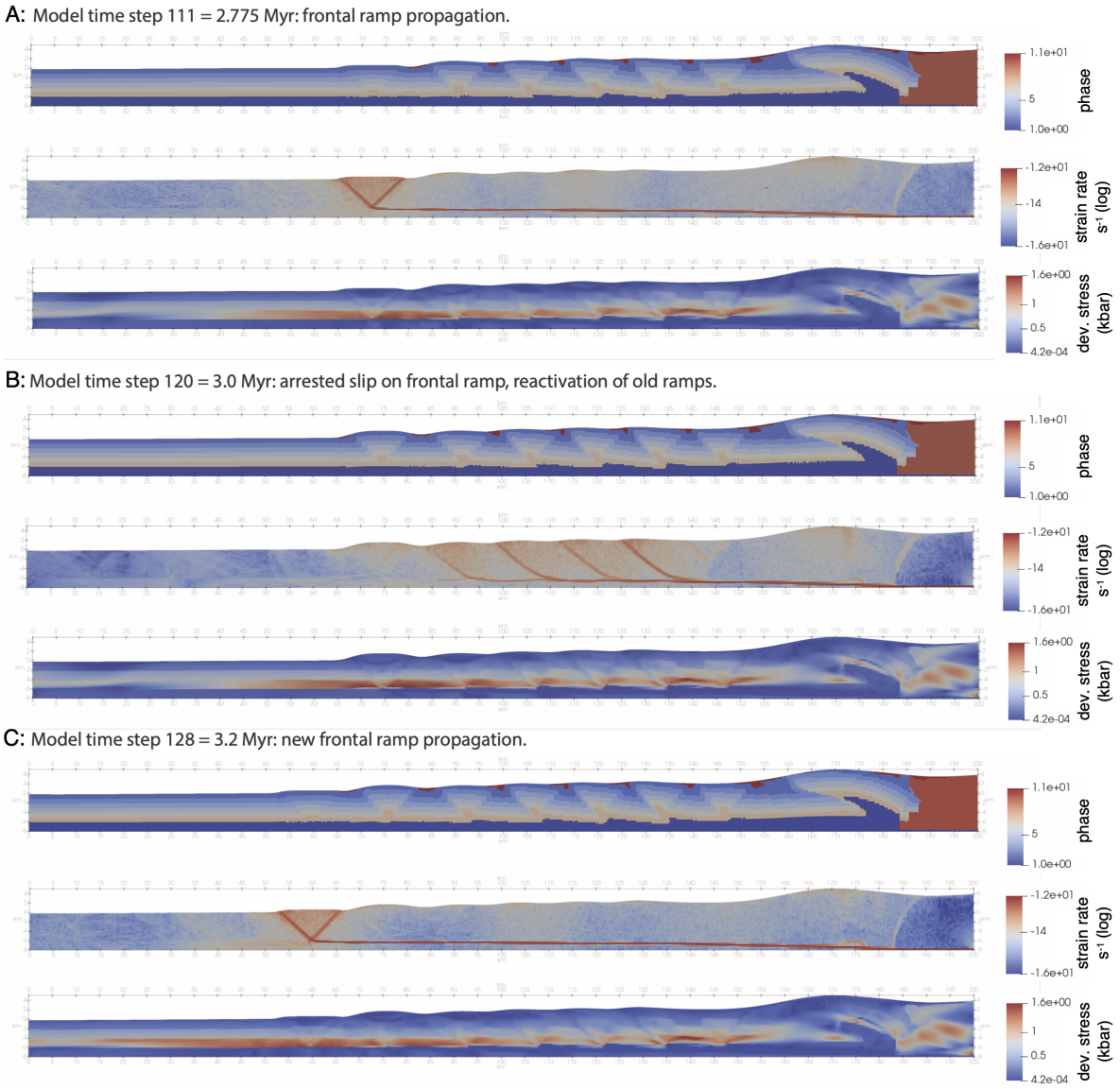

Figure 4.28: Snapshot views of finite difference numerical model to evaluate the mechanical conditions of ramp propagation and reactivation. (a) Time step 111 after 2.775 Myr of convergence, an incipient ramp has propagated to the foreland. (b) Time step 120 after an additional 225 kyr of model time. (c) Time step 128 after an additional 200 kyr of model time.

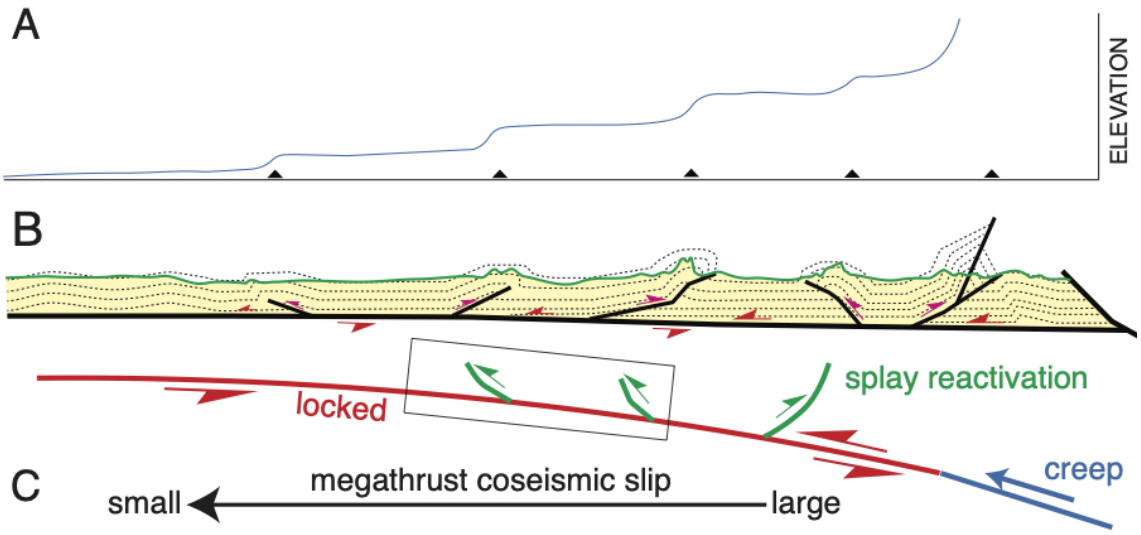

Figure 4.29: Schematic diagram showing potential thrust propagation and its geomorphic expresssion in the IBR outer belt. (a) Fluvial profile of an antecedent stream that cut across the antiforms (black triangles) in a sequential fold-thrust belt with continuous activation of older ramps. (b) Schematic cross section of the outer belt of the IBR modified after Betka et al. (2018). The green line on top of the cross section indicates the topographic profile with a 10x vertical exaggeration. (c) A possible scenario of megathrust and splay fault ruptures after Wang et al. (2014). The rectangle represents the region shown in (a) and (b).

variable lithology and erodibility, varying precipitation rates, and imposing different fold spacing distances. Since currently we do not have sufficient data constraining erosion and vertical uplift rates in the western IBR, we present only qualitative results. In the future, we hope to have other datasets, e.g., quantitative estimates of rock uplift and erosion rates, that would allow us to better constrain the long-term timescales and process parameters involved in the growth and erosion of the anticlinal structures, hoping to find quantitative relationships between the tectonic deformation, surface process rates and drainage evolution through time.

4.7 Conclusion

By investigating the stream profiles and knickpoint locations along the studied tributaries in the outer belt of the IBR and developing first order surface dynamics models, we find that the sequence of anticline propagation controls the first-order shapes of antecedent fluvial profiles. For sequential ramp propagation where model fold growth is limited to the frontal structure, there are knickpoints upstream near the outlet on fluvial profiles where the incipient fold is located. There might also be smooth, convex segments upstream due to knickpoint

migration. On the other hand, for sequential propagation with reactivation of older ramps, there are knickpoints observed on fluvial profiles in many locations, particularly at active antiform sites. As the streams cross several active antiforms, the convex segments of their fluvial profiles are unlikely to be observed. Our models show that fluvial profiles can be used to infer kinematic evolution of fold-thrust belts and help to inform their seismic potential.

By comparing our modeling results to the outer-belt observations, all the antiforms in our study region are likely to have continued to rise to the present day. The eastern folds are reactivated even as the thrust front propagates westward. It is also possible that some of the antiforms initiated concurrently. Accordingly, continuous reactivation of older ramps likely contributes to the structural growth of the IBR. Therefore, independent failures of reactivated out-of-sequence splay faults may occur more frequently than megathrust ruptures, causing intermediate-magnitude shallow earthquakes.

Chapter 5

Conclusions

In the studies presented here, I investigated both short- and long-term tectonics across the Indo Burma range (IBR). There continues to be some controversy about whether the subduction is ongoing and capable of producing > M8 earthquakes in the future. Although the short- and long-term study results address very different observations, the integrated information obtained from the investigations helps improve our understanding of the tectonics across the IBR.

For the study of principal stress orientations based on focal mechanisms across the IBR (Chapter 2), I found a nearly constant NS σ_1 direction in all domains, while the σ_3 below the upper plate (> 30-km depth) always orientates ∼EW. This is not expected since several published geodetic studies (i.e., Socquet et al., 2006; Steckler et al., 2016; and Mallick et al., 2019), and IBR surface structures (NS-oriented antiforms) suggest EW compression across this boundary. Moreover, there are six earthquakes with shallow east-dipping nodal planes that potentially occur on the megathrust. However, this seismicity observation alone cannot confirm ongoing subduction thrust activity. In addition, the orientation of the σ_1 axis, sub-parallel to the slab strike, is consistent with the obliquely convergent plate motion. The consistency of the NS-oriented σ_1 at all depth ranges suggests compression due to the northward-moving slab pushing through the mantle. On the other hand, the EW-oriented σ_3 in which its plunge is consistent with the slab dip suggests downdip tension, and thus the driving force governing it is likely a net slab pull. Accordingly, it is possible that the slab pulling force contributes to the formation of the IBR surface structures. It is still inconclusive whether the megathrust is locked and able to produce major earthquakes in the future, even though a great 1762 earthquake has been attributed to the subduction thrust. In spite of that, the findings in this chapter suggest that we cannot rule out that the convergent boundary has high possibility to generate the megathrust events.

According to the long-term tectonics study examining the stream- and basin-scale morphometric indices (Chapter 3), the relative uplift rates, suggested by the k_{sn}, are greater in the eastern IBR inner belt than the west. This finding is consistent with the observation of out-of-sequence thrusts in the upper plate region between the Churachandpur Mao Fault and Kabaw Fault. In addition, the transition from high to low k_{sn} values is observed around

the Tut Fault, an active reverse fault deeply rooted from the megathrust in the eastern IBR. These active splay faults suggested by Betka et al. (2018) and Chit Thet Mon et al. (2020) are consistent to our geomorphic observation indicating active tectonic uplift even in the inner belt.

Since there is evidence of out-of-sequence thrusts in the eastern IBR, it is possible that there also might be out-of-sequence reactivation of older ramps in the western outer belt. In Chapter 4, I propose that the fluvial profiles of streams crossing the active fold-thrust belt are able to record information about the sequence of thrust propagation, suggesting the kinematic evolution of the belt. My findings suggest that the shapes of stream profiles in surface dynamics models involving sequential thrust propagation with continuous reactivation of older structures are the most comparable to the IBR outer-belt profiles. The synchronous thrusting model also provides similar results to the westernmost IBR investigation. This indicates that even though the deformation front has migrated westward, the older, eastern antiforms in the outer belt are still active. Moreover, the bivergent antiform structures and numerical fold-thrust belt models invoking a weak décollement provide additional support for reactivated out-of-sequence thrusts in the outer belt. This suggests that the megathrust is tectonically active in this region. Although it is not certain if the megathrust can fully rupture causing major earthquakes, it is likely that independent failures of the reactivated splay faults can cause frequent, moderate events in the future.

Overall, my studies suggest active tectonics and seismic activity across the IBR, even though both short- and long-term investigations do not allow us to conclude if the megathrust is fully locked and able to generate $>$ M8 earthquakes. The findings and observations in Chapter 2 - 4 indicate that the IBR is tectonically active, and the intermediate-magnitude earthquakes can frequently occur due to independent failures of the active splay faults across the region. These events may cause significant damage across the IBR, particularly in sediment-filled valleys which are the densely populated areas. Accordingly, I hope my studies will raise an awareness of local governments in the area so, that they can educate people and prepare for future earthquakes and associated hazards, such as landslides.

Bibliography

Alam, M., Alam, M. M., Curray, J. R., Chowdhury, M. L. R., & Gani, M. R. (2003). An overview of the sedimentary geology of the bengal basin in relation to the regional tectonic framework and basin-fill history. *Sedimentary geology*, *155*(3-4), 179–208.

Aung, L. T., Oo, K. Z., Win, K. M., Moore, G. F., Tun, S. T., & Naing, W. (2020). Active deformation of the central myanmar forearc basin: Insight from post-pleistocene inversion of the pyay fault. *Journal of Asian Earth Sciences: X*, *4*, 100037.

Aung, T. T., Satake, K., Okamura, Y., Shishikura, M., Swe, W., Saw, H., Swe, T. L., Tun, S. T., & Aung, T. (2008). Geologic evidence for three great earthquakes in the past 3400 years off myanmar. *Journal of Earthquake and Tsunami*, *2*(04), 259–265.

Azañón, J., Pérez-Peña, J., Giaconia, F., Booth-Rea, G., Martınez-Martınez, J., & Rodrıguez-Peces, M. (2012). Active tectonics in the central and eastern betic cordillera through morphotectonic analysis: The case of sierra nevada and sierra alhamilla. *Journal of Iberian Geology*, *38*(1), 225–238.

Bally, A. W., Gordy, P., & Stewart, G. A. (1966). Structure, seismic data, and orogenic evolution of southern canadian rocky mountains. *Bulletin of Canadian Petroleum Geology*, *14*(3), 337–381.

Banerjee, P., Bürgmann, R., Nagarajan, B., & Apel, E. (2008). Intraplate deformation of the indian subcontinent. *Geophysical Research Letters*, *35*(18).

Bellin, N., Vanacker, V., & Kubik, P. (2014). Denudation rates and tectonic geomorphology of the spanish betic cordillera. *Earth and Planetary Science Letters*, *390*, 19–30.

Betka, P. M., Seeber, L., Thomson, S. N., Steckler, M. S., Sincavage, R., & Zoramthara, C. (2018). Slip-partitioning above a shallow, weak décollement beneath the indo-burman accretionary prism. *Earth and Planetary Science Letters*, *503*, 17–28.

Betka, P. M., Thomson, S. N., Sincavage, R., Zoramthara, C., Lalremruatfela, C., Lang, K. A., Steckler, M. S., Bezbaruah, D., Borgohain, P., & Seeber, L. (2021). Provenance shifts during neogene brahmaputra delta progradation tied to coupled climate and tectonic change in the eastern himalaya. *Geochemistry, Geophysics, Geosystems*, *22*(12), e2021GC010026.

Bhattarai, I., Gani, N. D., & Xue, L. (2021). Geomorphological responses of rivers to active tectonics along the siwalik hills, midwestern nepalese himalaya. *Journal of Mountain Science*, *18*(5), 1268–1294.

Bilotti, F., & Shaw, J. H. (2005). Deep-water niger delta fold and thrust belt modeled as a critical-taper wedge: The influence of elevated basal fluid pressure on structural styles. *AAPG bulletin*, *89*(11), 1475–1491.

Bookhagen, B., & Strecker, M. R. (2008). Orographic barriers, high-resolution trmm rainfall, and relief variations along the eastern andes. *Geophysical Research Letters*, *35*(6).

Boulton, S., Stokes, M., & Mather, A. (2014). Transient fluvial incision as an indicator of active faulting and plio-quaternary uplift of the moroccan high atlas. *Tectonophysics*, *633*, 16–33.

Boyer, S. E., & Elliott, D. (1982). Thrust systems. *Aapg Bulletin*, *66*(9), 1196–1230.

Brocklehurst, S. H., & Whipple, K. X. (2002). Glacial erosion and relief production in the eastern sierra nevada, california. *Geomorphology*, *42*(1-2), 1–24.

Burbank, D., Meigs, A., & Brozović, N. (1996). Interactions of growing folds and coeval depositional systems. *Basin Research*, *8*(3), 199–223.

Burbank, D., Blythe, A., Putkonen, J., Pratt-Sitaula, B., Gabet, E., Oskin, M., Barros, A., & Ojha, T. (2003). Decoupling of erosion and precipitation in the himalayas. *Nature*, *426*(6967), 652–655.

Bürgi, P., Hubbard, J., Akhter, S. H., & Peterson, D. E. (2021). Geometry of the décollement below eastern bangladesh and implications for seismic hazard. *Journal of Geophysical Research: Solid Earth*, *126*(8), e2020JB021519.

Copley, A., & McKenzie, D. (2007). Models of crustal flow in the india-asia collision zone. *Geophysical Journal International*, *169*(2), 683–698.

Corredor, F., Shaw, J. H., & Bilotti, F. (2005). Structural styles in the deep-water fold and thrust belts of the niger delta. *AAPG bulletin*, *89*(6), 753–780.

Cundall, P., & Board, M. (1988). A microcomputer program for modelling large-strain plasticity problems. proceedings of the sixth international conference on numerical methods in geomechanics, 11-15 april 1988, innsbruck, austria. volumes 1-3. *Publication of: Balkema (AA).*

Curray, J., Moore, D., Lawver, L., Emmel, F., Raitt, R., Henry, M., & Kieckhefer, R. (1979). Tectonics of the andaman sea and burma: Convergent margins.

Cyr, A. J., Granger, D. E., Olivetti, V., & Molin, P. (2010). Quantifying rock uplift rates using channel steepness and cosmogenic nuclide–determined erosion rates: Examples from northern and southern italy. *Lithosphere*, *2*(3), 188–198.

Duvall, A., Kirby, E., & Burbank, D. (2004). Tectonic and lithologic controls on bedrock channel profiles and processes in coastal california. *Journal of Geophysical Research: Earth Surface*, *109*(F3).

Earnest, A., Sunilkumar, T., & Silpa, K. (2021). Sinking slab stress and seismo-tectonics of the indo-burmese arc: A reappraisal. *Tectonics*, *40*(8), e2021TC006827.

Flint, J.-J. (1974). Stream gradient as a function of order, magnitude, and discharge. *Water Resources Research*, *10*(5), 969–973.

Forte, A. M., & Whipple, K. X. (2018). Criteria and tools for determining drainage divide stability. *Earth and Planetary Science Letters*, *493*, 102–117.

Gahalaut, V. K., Kundu, B., Laishram, S. S., Catherine, J., Kumar, A., Singh, M. D., Tiwari, R., Chadha, R., Samanta, S., Ambikapathy, A., et al. (2013). Aseismic plate boundary in the indo-burmese wedge, northwest sunda arc. *Geology*, *41*(2), 235–238.

Gaidzik, K., & Ramırez-Herrera, M. T. (2017). Geomorphic indices and relative tectonic uplift in the guerrero sector of the mexican forearc. *Geoscience Frontiers*, *8*(4), 885–902.

Gailleton, B., Mudd, S. M., Clubb, F. J., Peifer, D., & Hurst, M. D. (2019). A segmentation approach for the reproducible extraction and quantification of knickpoints from river long profiles. *Earth Surface Dynamics*, *7*(1), 211–230.

Gani, M. R., & Alam, M. M. (1999). Trench-slope controlled deep-sea clastics in the exposed lower surma group in the southeastern fold belt of the bengal basin, bangladesh. *Sedimentary Geology*, *127*(3-4), 221–236.

Govin, G., Najman, Y., Copley, A., Millar, I., Van der Beek, P., Huyghe, P., Grujic, D., & Davenport, J. (2018). Timing and mechanism of the rise of the shillong plateau in the himalayan foreland. *Geology*, *46*(3), 279–282.

Guzmán-Speziale, M., & Ni, J. F. (2000). Comment on "subduction in the indo-burma region: Is it still active?" by sp satyabala. *Geophysical Research Letters*, *27*(7), 1065–1066.

Hack, J. T. (1957). *Studies of longitudinal stream profiles in virginia and maryland* (Vol. 294). US Government Printing Office.

Halsted, E. P. (1841). Report on the island of chedooba.

Hardebeck, J. L. (2015). Stress orientations in subduction zones and the strength of subduction megathrust faults. *Science*, *349*(6253), 1213–1216.

Harkins, N., Kirby, E., Heimsath, A., Robinson, R., & Reiser, U. (2007). Transient fluvial incision in the headwaters of the yellow river, northeastern tibet, china. *Journal of Geophysical Research: Earth Surface*, *112*(F3).

Haviv, I., Enzel, Y., Whipple, K., Zilberman, E., Matmon, A., Stone, J., & Fifield, K. (2010). Evolution of vertical knickpoints (waterfalls) with resistant caprock: Insights from numerical modeling. *Journal of Geophysical Research: Earth Surface*, *115*(F3).

Hayes, G. P., Moore, G. L., Portner, D. E., Hearne, M., Flamme, H., Furtney, M., & Smoczyk, G. M. (2018). Slab2, a comprehensive subduction zone geometry model. *Science*, *362*(6410), 58–61.

Hobley, D. E., Adams, J. M., Nudurupati, S. S., Hutton, E. W., Gasparini, N. M., Istanbulluoglu, E., & Tucker, G. E. (2017). Creative computing with landlab: An open-source toolkit for building, coupling, and exploring two-dimensional numerical models of earth-surface dynamics. *Earth Surface Dynamics*, *5*(1), 21–46.

Hoque, M. E., Islam, M., Karmakar, S., Rahman, M. A., & Bhuyan, M. S. (2021). Sediment organic matter and physicochemical properties of a multipurpose artificial lake to assess catchment land use: A case study of kaptai lake, bangladesh. *Environmental Challenges*, *3*, 100070.

Howard, A. D., & Kerby, G. (1983). Channel changes in badlands. *Geological Society of America Bulletin*, *94*(6), 739–752.

Hurukawa, N., Tun, P. P., & Shibazaki, B. (2012). Detailed geometry of the subducting indian plate beneath the burma plate and subcrustal seismicity in the burma plate derived from joint hypocenter relocation. *Earth, planets and space*, *64*(4), 333–343.

Islam, A. R. M., Habib, M. et al. (2015). Identification of gas sand horizons of the rashidpur structure, surma basin, bangladesh, using 2d seismic interpretation. *International Journal of Geophysics*, *2015*.

Itasca, F. (2000). Fast lagrangian analysis of continua. *Itasca Consulting Group Inc., Minneapolis, Minn*.

Johnson, S. Y., & NUR ALAM, A. M. (1991). Sedimentation and tectonics of the sylhet trough, bangladesh. *Geological Society of America Bulletin*, *103*(11), 1513–1527.

Kagan, Y. Y. (2007). Simplified algorithms for calculating double-couple rotation. *Geophysical Journal International*, *171*(1), 411–418.

Kagan, Y. (1991). 3-d rotation of double-couple earthquake sources. *Geophysical Journal International*, *106*(3), 709–716.

Keller, E. A., & Pinter, N. (1996). *Active tectonics* (Vol. 338). Prentice Hall Upper Saddle River, NJ.

Kirby, E., & Whipple, K. (2001). Quantifying differential rock-uplift rates via stream profile analysis. *Geology*, *29*(5), 415–418.

Kirby, E., & Whipple, K. X. (2012). Expression of active tectonics in erosional landscapes. *Journal of Structural Geology*, *44*, 54–75.

Kreemer, C., Blewitt, G., & Klein, E. C. (2014). A geodetic plate motion and global strain rate model. *Geochemistry, Geophysics, Geosystems*, *15*(10), 3849–3889.

Krien, Y., Karpytchev, M., Ballu, V., Becker, M., Grall, C., Goodbred, S., Calmant, S., Shum, C., & Khan, Z. (2019). Present-day subsidence in the ganges-brahmaputra-meghna delta: Eastern amplification of the holocene sediment loading contribution. *Geophysical Research Letters*, *46*(19), 10764–10772.

Kundu, B., & Gahalaut, V. (2012). Earthquake occurrence processes in the indo-burmese wedge and sagaing fault region. *Tectonophysics*, *524*, 135–146.

Kundu, B., & Gahalaut, V. (2013). Tectonic geodesy revealing geodynamic complexity of the indo-burmese arc region, north east india. *Current Science*, 920–933.

Lyons, N. J., Val, P., Albert, J. S., Willenbring, J. K., & Gasparini, N. M. (2020). Topographic controls on divide migration, stream capture, and diversification in riverine life. *Earth Surface Dynamics*, *8*(4), 893–912.

Mallick, R., Lindsey, E. O., Feng, L., Hubbard, J., Banerjee, P., & Hill, E. M. (2019). Active convergence of the india-burma-sunda plates revealed by a new continuous gps network. *Journal of Geophysical Research: Solid Earth*, *124*(3), 3155–3171.

Maneerat, P., & Bürgmann, R. (2022). Geomorphic expressions of active tectonics across the indo-burma range. *Journal of Asian Earth Sciences*, *223*, 105008.

Marrucci, M., Zeilinger, G., Ribolini, A., & Schwanghart, W. (2018). Origin of knickpoints in an alpine context subject to different perturbing factors, stura valley, maritime alps (north-western italy). *Geosciences*, *8*(12), 443.

Maurin, T., & Rangin, C. (2009). Impact of the 90 e ridge at the indo-burmese subduction zone imaged from deep seismic reflection data. *Marine Geology*, *266*(1-4), 143–155.

McClay, K. (1992). Glossary of thrust tectonics terms. *Thrust tectonics*, 419–433.

Mitchell, A. (1993). Cretaceous–cenozoic tectonic events in the western myanmar (burma)–assam region. *Journal of the Geological Society*, *150*(6), 1089–1102.

Mon, C. T., Gong, X., Wen, Y., Jiang, M., Chen, Q.-F., Zhang, M., Hou, G., Thant, M., Sein, K., & He, Y. (2020). Insight into major active faults in central myanmar and the related geodynamic sources. *Geophysical Research Letters*, *47*(8), e2019GL086236.

Mondal, D. R., McHugh, C. M., Mortlock, R. A., Steckler, M. S., Mustaque, S., & Akhter, S. H. (2018). Microatolls document the 1762 and prior earthquakes along the southeast coast of bangladesh. *Tectonophysics*, *745*, 196–213.

Mudd, S. M., Attal, M., Milodowski, D. T., Grieve, S. W., & Valters, D. A. (2014). A statistical framework to quantify spatial variation in channel gradients using the integral method of channel profile analysis. *Journal of Geophysical Research: Earth Surface*, *119*(2), 138–152.

Najman, Y., Bickle, M., BouDagher-Fadel, M., Carter, A., Garzanti, E., Paul, M., Wijbrans, J., Willett, E., Oliver, G., Parrish, R., et al. (2008). The paleogene record of himalayan erosion: Bengal basin, bangladesh. *Earth and Planetary Science Letters*, *273*(1-2), 1–14.

Najman, Y., Bracciali, L., Parrish, R. R., Chisty, E., & Copley, A. (2016). Evolving strain partitioning in the eastern himalaya: The growth of the shillong plateau. *Earth and Planetary Science Letters*, *433*, 1–9.

Neely, A., Bookhagen, B., & Burbank, D. (2017). An automated knickzone selection algorithm (kz-picker) to analyze transient landscapes: Calibration and validation. *Journal of Geophysical Research: Earth Surface*, *122*(6), 1236–1261.

Oleskevich, D., Hyndman, R., & Wang, K. (1999). The updip and downdip limits to great subduction earthquakes: Thermal and structural models of cascadia, south alaska, sw japan, and chile. *Journal of Geophysical Research: Solid Earth*, *104*(B7), 14965–14991.

Panda, D., Kundu, B., Gahalaut, V. K., & Rangin, C. (2020). India-sunda plate motion, crustal deformation, and seismic hazard in the indo-burmese arc. *Tectonics*, *39*(8), e2019TC006034.

Pérez Peña, J. V. (2009). Gis-based tools and methods for landscape analysis and active tectonic evaluation.

Pérez-Peña, J. V., Azor, A., Azañón, J. M., & Keller, E. A. (2010). Active tectonics in the sierra nevada (betic cordillera, se spain): Insights from geomorphic indexes and drainage pattern analysis. *Geomorphology*, *119*(1-2), 74–87.

Perron, J. T., & Royden, L. (2013). An integral approach to bedrock river profile analysis. *Earth Surface Processes and Landforms*, *38*(6), 570–576.

Plafker, G. (1965). Tectonic deformation associated with the 1964 alaska earthquake: The earthquake of 27 march 1964 resulted in observable crustal deformation of unprecedented areal extent. *Science*, *148*(3678), 1675–1687.

Rangin, C. (2016). Rigid and non-rigid micro-plates: Philippines and myanmar-andaman case studies. *Comptes Rendus Geoscience*, *348*(1), 33–41.

Rangin, C. (2017). Active and recent tectonics of the burma platelet in myanmar. *Geological Society, London, Memoirs*, *48*(1), 53–64.

Rangin, C., Maurin, T., & Masson, F. (2013). Combined effects of eurasia/sunda oblique convergence and east-tibetan crustal flow on the active tectonics of burma. *Journal of Asian Earth Sciences*, *76*, 185–194.

Rao, N. P., & Kumar, M. R. (1999). Evidences for cessation of indian plate subduction in the burmese arc region. *Geophysical Research Letters*, *26*(20), 3149–3152.

Reitman, N. G., Mueller, K. J., Tucker, G. E., Gold, R. D., Briggs, R. W., & Barnhart, K. R. (2019). Offset channels may not accurately record strike-slip fault displacement: Evidence from landscape evolution models. *Journal of Geophysical Research: Solid Earth*, *124*(12), 13427–13451.

Roering, J. J. (2008). How well can hillslope evolution models "explain" topography? simulating soil transport and production with high-resolution topographic data. *Geological Society of America Bulletin*, *120*(9-10), 1248–1262.

Roering, J. J., Kirchner, J. W., & Dietrich, W. E. (1999). Evidence for nonlinear, diffusive sediment transport on hillslopes and implications for landscape morphology. *Water Resources Research*, *35*(3), 853–870.

Roering, J. J., Perron, J. T., & Kirchner, J. W. (2007). Functional relationships between denudation and hillslope form and relief. *Earth and Planetary Science Letters*, *264*(1-2), 245–258.

Satyabala, S. (1998). Subduction in the indo-burma region: Is it still active? *Geophysical Research Letters*, *25*(16), 3189–3192.

Schwanghart, W., & Scherler, D. (2014). Topotoolbox 2–matlab-based software for topographic analysis and modeling in earth surface sciences. *Earth Surface Dynamics*, *2*(1), 1–7.

Schwanghart, W., & Scherler, D. (2017). Bumps in river profiles: Uncertainty assessment and smoothing using quantile regression techniques. *Earth Surface Dynamics*, *5*(4), 821–839.

Seeber, L., & Gornitz, V. (1983). River profiles along the himalayan arc as indicators of active tectonics. *Tectonophysics*, *92*(4), 335–367.

Shi, X., Wang, Y., Sieh, K., Weldon, R., Feng, L., Chan, C.-H., & Liu-Zeng, J. (2018). Fault slip and gps velocities across the shan plateau define a curved southwestward crustal motion around the eastern himalayan syntaxis. *Journal of Geophysical Research: Solid Earth*, *123*(3), 2502–2518.

Shyu, J. B. H., Wang, C.-C., Wang, Y., Shen, C.-C., Chiang, H.-W., Liu, S.-C., Min, S., Aung, L. T., Than, O., & Tun, S. T. (2018). Upper-plate splay fault earthquakes along the arakan subduction belt recorded by uplifted coral microatolls on northern ramree island, western myanmar (burma). *Earth and Planetary Science Letters*, *484*, 241–252.

Sikder, A. M., & Alam, M. M. (2003). 2-d modelling of the anticlinal structures and structural development of the eastern fold belt of the bengal basin, bangladesh. *Sedimentary Geology*, *155*(3-4), 209–226.

Sincavage, R., Betka, P. M., Thomson, S. N., Seeber, L., Steckler, M., & Zoramthara, C. (2020). Neogene shallow-marine and fluvial sediment dispersal, burial, and exhumation in the ancestral brahmaputra delta: Indo-burman ranges, india. *Journal of Sedimentary Research*, *90*(9), 1244–1263.

Singh, O., Sarangi, A., & Sharma, M. C. (2008). Hypsometric integral estimation methods and its relevance on erosion status of north-western lesser himalayan watersheds. *Water Resources Management*, *22*(11), 1545–1560.

Snyder, N. P., Whipple, K. X., Tucker, G. E., & Merritts, D. J. (2000). Landscape response to tectonic forcing: Digital elevation model analysis of stream profiles in the mendocino triple junction region, northern california. *Geological Society of America Bulletin*, *112*(8), 1250–1263.

Snyder, N. P., Whipple, K. X., Tucker, G. E., & Merritts, D. J. (2003). Importance of a stochastic distribution of floods and erosion thresholds in the bedrock river incision problem. *Journal of Geophysical Research: Solid Earth*, *108*(B2).

Socquet, A., Vigny, C., Chamot-Rooke, N., Simons, W., Rangin, C., & Ambrosius, B. (2006). India and sunda plates motion and deformation along their boundary in myanmar determined by gps. *Journal of Geophysical Research: Solid Earth*, *111*(B5).

Steckler, M. S., Akhter, S. H., & Seeber, L. (2008). Collision of the ganges–brahmaputra delta with the burma arc: Implications for earthquake hazard. *Earth and Planetary Science Letters*, *273*(3-4), 367–378.

Steckler, M. S., Mondal, D. R., Akhter, S. H., Seeber, L., Feng, L., Gale, J., Hill, E. M., & Howe, M. (2016). Locked and loading megathrust linked to active subduction beneath the indo-burman ranges. *Nature Geoscience*, *9*(8), 615–618.

Stock, G. M., Anderson, R. S., & Finkel, R. C. (2004). Pace of landscape evolution in the sierra nevada, california, revealed by cosmogenic dating of cave sediments. *Geology*, *32*(3), 193–196.

Stockmal, G. S., Beaumont, C., Nguyen, M., & Lee, B. (2007). Mechanics of thin-skinned fold-and-thrust belts: Insights from numerical models.

Strahler, A. N. (1957). Quantitative analysis of watershed geomorphology. *Eos, Transactions American Geophysical Union*, *38*(6), 913–920.

Vavryčuk, V. (2014). Iterative joint inversion for stress and fault orientations from focal mechanisms. *Geophysical Journal International*, *199*(1), 69–77.

Vigny, C., Socquet, A., Rangin, C., Chamot-Rooke, N., Pubellier, M., Bouin, M.-N., Bertrand, G., & Becker, M. (2003). Present-day crustal deformation around sagaing fault, myanmar. *Journal of Geophysical Research: Solid Earth*, *108*(B11).

Vorobieva, I., Gorshkov, A., & Mandal, P. (2021). Modelling the seismic potential of the indo-burman megathrust. *Scientific reports*, *11*(1), 1–13.

Wada, I., Mazzotti, S., & Wang, K. (2010). Intraslab stresses in the cascadia subduction zone from inversion of earthquake focal mechanisms. *Bulletin of the Seismological Society of America*, *100*(5A), 2002–2013.

Wang, K. (2000). Stress–strain 'paradox', plate coupling, and forearc seismicity at the cascadia and nankai subduction zones. *Tectonophysics*, *319*(4), 321–338.

Wang, K., & Tréhu, A. M. (2016). Invited review paper: Some outstanding issues in the study of great megathrust earthquakes—the cascadia example. *Journal of Geodynamics*, *98*, 1–18.

Wang, K., Wada, I., & Ishikawa, Y. (2004). Stresses in the subducting slab beneath southwest japan and relation with plate geometry, tectonic forces, slab dehydration, and damaging earthquakes. *Journal of Geophysical Research: Solid Earth*, *109*(B8).

Wang, X., Wei, S., Wang, Y., Maung Maung, P., Hubbard, J., Banerjee, P., Huang, B.-S., Moe Oo, K., Bodin, T., Foster, A., et al. (2019). A 3-d shear wave velocity model for myanmar region. *Journal of Geophysical Research: Solid Earth*, *124*(1), 504–526.

Wang, Y., Zhang, H., Zheng, D., Yu, J., Pang, J., & Ma, Y. (2017). Coupling slope–area analysis, integral approach and statistic tests to steady-state bedrock river profile analysis. *Earth Surface Dynamics*, *5*(1), 145–160.

Wang, Y., Shyu, J. B. H., Sieh, K., Chiang, H.-W., Wang, C.-C., Aung, T., Lin, Y.-n. N., Shen, C.-C., Min, S., Than, O., et al. (2013). Permanent upper plate deformation in western myanmar during the great 1762 earthquake: Implications for neotectonic behavior of the northern sunda megathrust. *Journal of Geophysical Research: Solid Earth*, *118*(3), 1277–1303.

Wang, Y., Sieh, K., Tun, S. T., Lai, K.-Y., & Myint, T. (2014). Active tectonics and earthquake potential of the myanmar region. *Journal of Geophysical Research: Solid Earth*, *119*(4), 3767–3822.

Whipple, K. X., Dibiase, R. A., & Crosby, B. (2013). Bedrock rivers. *Fluvial geomorphology* (pp. 550–573). Elsevier Inc.

Whipple, K. X., & Tucker, G. E. (1999). Dynamics of the stream-power river incision model: Implications for height limits of mountain ranges, landscape response timescales, and research needs. *Journal of Geophysical Research: Solid Earth*, *104*(B8), 17661–17674.

Whipple, K., Forte, A., DiBiase, R., Gasparini, N., & Ouimet, W. (2017). Timescales of landscape response to divide migration and drainage capture: Implications for the role of divide mobility in landscape evolution. *Journal of Geophysical Research: Earth Surface*, *122*(1), 248–273.

Willett, S. D., McCoy, S. W., Perron, J. T., Goren, L., & Chen, C.-Y. (2014). Dynamic reorganization of river basins. *Science*, *343*(6175).

Wobus, C., Whipple, K. X., Kirby, E., Snyder, N., Johnson, J., Spyropolou, K., Crosby, B., Sheehan, D., & Willett, S. (2006). Tectonics from topography: Procedures, promise, and pitfalls. *Special papers-geological society of america*, *398*, 55.

Wu, J. E., & McClay, K. R. (2011). Two-dimensional analog modeling of fold and thrust belts: Dynamic interactions with syncontractional sedimentation and erosion.

Wu, S., Yao, J., Wei, S., Hubbard, J., Wang, Y., Htwe, Y. M. M., Thant, M., Wang, X., Wang, K., Liu, T., et al. (2021). New insights into the structural heterogeneity and geodynamics of the indo-burma subduction zone from ambient noise tomography. *Earth and Planetary Science Letters*, *562*, 116856.

Yao, J., Liu, S., Wei, S., Hubbard, J., Huang, B.-S., Chen, M., & Tong, P. (2021). Slab models beneath central myanmar revealed by a joint inversion of regional and teleseismic traveltime data. *Journal of Geophysical Research: Solid Earth*, *126*(2), e2020JB020164.

Zahid, K. M., & Uddin, A. (2005). Influence of overpressure on formation velocity evaluation of neogene strata from the eastern bengal basin, bangladesh. *Journal of Asian Earth Sciences*, *25*(3), 419–429.